SYNTHESIS PROCESS USING CHARACTERISTIC MODES FOR MULTIPLE IN SITU ANTENNAS FOR SYSTEM RADIATION REQUIREMENTS

BY

NICOLE L. BOHANNON

DISSERTATION

Submitted in partial fulfillment of the requirements
for the degree of Doctor of Philosophy in Electrical and Computer Engineering
in the Graduate College of the
University of Illinois at Urbana-Champaign, 2016

Urbana, Illinois

Doctoral Committee:

Professor Jennifer T. Bernhard, Chair
Professor Steven J. Franke
Professor Jianming Jin
Dr. Carey Buxton, FBI

ABSTRACT

Current methods for installing multiple antennas on a platform rely on trial and error or are primarily focused on isolation. Antenna designers create elements, place them on the platform, and then evaluate the results. This method is slow and does not utilize the platform geometry to achieve better performance. The goal of this research is to develop a synthesis method to design multiple antennas on a platform with a focus on radiation pattern performance.

Characteristic mode theory is commonly used to determine how structures will radiate. Solving for the modes on a structure gives the antenna designer an idea of which modes are easily excited on a structure. Each mode is associated with a modal far field. Because this research focuses on the impact of platform geometry on radiation pattern, characteristic mode theory is a natural fit.

This dissertation first examines how to excite higher order modes on structures. It compares the surface currents for each mode and determines a feed region. The element is then designed based on the feed location and the required direction of the surface current.

When the desired pattern is not associated with a modal far field, this dissertation develops a novel method for solving for the radiation pattern closest to the goal radiation pattern that is achievable on the structure. The radiation pattern solution corresponds to a specific surface current that must be excited by an element to create the optimized pattern. There are two optimization techniques provided. The first method requires the designer to specify power and polarization for the goal pattern while the second only requires specifying power. These methods are novel as they do not require the modal weighting coefficients to be equiphase.

These methods for determining surface current are combined to make a synthesis method for designing antenna elements at multiple frequencies to

be installed on one platform based on goal radiation patterns. The synthesis method begins with calculating the optimal surface currents for each frequency. Starting at the lowest frequency, antenna elements are designed based on the surface current. To demonstrate the new method, three antennas were designed and installed on a CubeSat chassis for operation at 400 MHz, 435 MHz, and 915 MHz. The platform was then constructed and the antenna performance was compared to the simulated performance.

Last, the modal far fields for the CubeSat were compared when there were slight changes to the simulated platform to account for changes between the simulated and constructed platform. Using a slightly altered platform, the optimized patterns were found for the identical scenario as the previous example. The resulting patterns and surface currents are compared to show the impact of model fidelity on the success of the developed synthesis method.

ACKNOWLEDGMENTS

I have never been particularly good at expressing how grateful I am for the support I have received throughout this process. Working toward my doctorate has been an extremely rewarding experience, but I could not have done it without the help, love, and support from many different people. No amount of words would be enough to properly thank all the people who have helped me along this journey, but I am going to do my best to thank as many as I can.

Rob, you have been there for me throughout this entire process. You stayed up late with me when I was having stressful nights. You cooked and cleaned and put up with all of the stress. You even listened to my long antenna ravings as I tried to figure out the next steps of my research. Thank you for everything you have done to make this possible. We are an incredible team.

Mom and Dad, my accomplishments are your accomplishments. From phone calls in tears to numerous plane tickets, you have always been there to help me any way that I needed. I cannot imagine going through this journey without your help. Tim, thanks for listening on many walks home and being my partner in crime.

To Bruce and Sue, thank you for letting me stay in your home as I went through the various steps of getting my Ph.D. You both made Champaign my home away from home and I truly appreciate that.

To the rest of my family, thank you for understanding my crazy schedule and for your unending love.

Professor Bernhard, I can honestly say I would not be here without you. When I first came to visit day at the University of Illinois, I was not even sure about going to graduate school. From deciding to go to graduate school, to deciding that I would pursue my doctoral degree, you walked me through the entire process. Your mentoring has made this experience extremely rewarding for me. Thank you for all of your advice and support throughout this entire

process.

I also want to thank my committee members Jianming Jin, Steven Franke, and Carey Buxton for your guidance and insight. To Carey and Dave, thank you for letting me spend time at your facility and take some of your time to measure the antennas in your chamber. To everyone with whom I spent time in Professor Bernhard's group, thank you for helping me work through road blocks, listening to practice talks, and convincing me that Illinois might not be so bad after all.

Thank you to the National Defense Science and Engineering Fellowship for funding this research.

Bill, I do not know how to thank you for everything you have done for me. Because of you, I got to go to my first antenna conference. You introduced me to the field of antennas and electromagnetics that has resulted in this dissertation. You made it possible for me to pursue my doctoral degree and achieve my personal goals at the same time.

To Danielle, Tom, Paul, and CAP, thank you for letting me present as well as volunteering to help me make measurements. Jess, I could not have done this without you. You helped me my first day at the University of Illinois and welcomed me into Prof. Bernhard's group. I could not have done this without you. Lady, thank you for all of the excellent hugs and cuddling.

To my friends and inevitably others who I may have missed, thank you for understanding and for always being there when I needed you. This has been an incredible journey and I could not have done it without all of you.

TABLE OF CONTENTS

CHAPTER 1

INTRODUCTION

Traditionally antenna designers are asked to add antennas to an existing structure (e.g., circuitry, cars, ships). The existing structure is typically much larger than the space allotted for the antenna design itself and the antenna designer has little to no control over the materials and shape. Because of the disparity in space allotment, these existing structures often exert considerable control over the pattern, isolation, and bandwidth for the installed antennas. Previous research has shown that for certain types of antennas, the larger structure is the dominant force driving bandwidth and radiation pattern [1, 2]. As technology continues to develop and designers attempt to minimize both the circuitry, existing structure, and antennas, it is important to utilize all available options to achieve the desired performance.

In addition to the issue of the size of the platform, more and more technology includes a variety of antennas in close proximity. Placing antennas close together influences their radiation patterns and the effectiveness of their accompanying wireless communication systems. The interaction of multiple antennas in proximity has led to three main areas of study: co-site interference, mutual coupling, and MIMO antennas. While all three research areas are devoted to understanding interaction between antennas, there is still more work to be done. Co-site interference research is dominated by military applications, focused on how to rectify degraded system performance due to collocated transmitters and receivers on ships and Humvees. Because of the heavy military influence, the solutions mainly swap one antenna element for another instead of designing the right antenna for a particular platform. The research also focused on adding filters or active cancellation because these can be added to a delivered system in lieu of redesigning the antenna or portions of a system. Mutual coupling research is more extensive in topic and application than co-site research but it focuses primarily on single frequency designs, leaving much room for understanding how antennas

interact over a broad range of frequencies. Mutual coupling research provides strategies for limiting mutual coupling but most are implemented once the antenna has been designed and the isolation is not high enough for the particular application. MIMO technology utilizes the mutual coupling research to focus on channel capacity increases. The research relies on the data capacity gains from antenna diversity and does not focus on creating specific desired antenna patterns. MIMO research also focuses on single frequency optimization because most MIMO systems operate over only one band of frequencies. Chapter 2 discusses co-site interference, mutual coupling, and MIMO antenna research in detail in order to explain the current state of the art.

Current research does not address how to design antennas when multiple elements have to be installed on a single platform that is large enough to have a significant impact but small enough that it cannot be considered an infinite ground plane. Additionally, there is little focus on providing desired radiation patterns at each frequency of interest. The goal of this research is to provide a synthesis procedure that focuses on antenna pattern synthesis when multiple antenna elements, across a variety of frequencies, must be placed in proximity on an existing structure. The synthesis procedure allows antenna designers to more efficiently utilize the existing structure to radiate the desired far field. Designers will also be able to efficiently and effectively know whether a desired radiation pattern is achievable on the given structure. If the radiation pattern is not exactly achievable, it will provide the best possible approximation of the desired pattern. Because the synthesis procedure takes the existing structure into account, the resulting far fields have the potential for larger gains in directions of interest as well as larger bandwidths. The procedure also ensures a much more efficient antenna design process for multiple elements on an existing structure.

A synthesis procedure for multiple elements over multiple frequency bands that takes into account radiation pattern requires a variety of research to complete. Chapter 3 describes characteristic mode theory and how it can be used to inform antenna element choice and feed position for modal far fields. Chapter 4 develops antenna radiation pattern synthesis techniques and demonstrates how these can be used to understand achievable patterns based on the existing structure. Chapter 5 connects the work from chapters 3 and 4 into a defined synthesis process. It details the designed synthesis

procedure and gives an example of an antenna system designed using the developed methodology. Chapter 6 investigates the impact on the characteristic modes and the modal far fields when small changes are made to the existing structure. Chapter 7 summarizes the previous chapters and details future work on this topic.

CHAPTER 2

BACKGROUND

As stated in the introduction, there are three main avenues of research that attempt to address how antennas interact when they are in proximity. Co-site interference, mutual coupling, and MIMO research all address multiple antenna interaction from a variety of different viewpoints. Each research area has a different focus and goal when optimizing or determining the impact of different antenna structures.

Co-site interference research focuses primarily on military applications and because of that focus, the solutions available are limited. The designers must use existing, previously developed antennas and all solutions must be able to be mass produced. Mutual coupling research is focused on the antenna's proximity effect on impedance and isolation. Many of the techniques used to increase isolation in mutual coupling research are also evaluated for MIMO antennas. MIMO antenna research aims to improve isolation and reduce correlation between antennas in order to increase channel capacity by providing multiple alternate paths from the transmit antenna to the receiver. The goal of the research is simply to provide two isolated antennas with much less focus on ideal patterns or other desired characteristics. The next three sections go into more detail about the state of the art in each topic and discuss the existing gaps in current research.

2.1 Co-site Interference

Co-site interference research focuses on providing solutions to current problems plaguing currently installed systems. Especially in the earlier co-site interference research, the main focus is to mitigate the effects of transmitters with known signals on nearby victim receivers. One of the papers on co-site interference details an automated process for installing shipboard RF

equipment [3]. The developed procedure first calculates the isolation based on the positioning of the antennas, and then uses that information to provide a statistical analysis on the functioning of the RF systems. It iterates through various positions to find a placement with acceptable RF performance. Within the automated procedure, the only changes that can be made are to move the available antennas around on the existing platform or swap one antenna for another prefabricated one. There is no discussion about how to redesign the antenna for increased performance or isolation. The paper does not address how to choose antennas or placements but simply iterates through them until one either meets system requirements or it is determined that system requirements cannot be met. This process is time consuming and gives little insight into how to design an antenna solution if all available options do not fit the system requirements.

Other papers provide limited options for dealing with interference. The main suggestions focus on filtering out unwanted frequencies or active cancellation of known transmit signals [3, 4, 5, 6]. These cancellation techniques can be complex and difficult to implement, especially when interfering signals can have a variety of frequencies and waveforms. For frequency hopping platforms, these papers suggest hopping filters or narrow-band frequency reconfigurable antennas to minimize interference.

Because active cancellation and filtering can be seen as complex, some research focuses on how to achieve physical isolation on existing platforms [5]. Figure 2.1 shows one of the testing platforms to evaluate multiple antennas and systems used in proximity for a military vehicle. The platform extends beyond the vehicle itself and utilizes identical types of antennas for simplicity. This research concluded that the multiple antennas could not be sufficiently separated on the existing platform–accordingly, an interference cancellation unit was installed to actively cancel interfering signals.

Alemohammad et al. provides a solution for co-site interference by using photonic signal cancellation [7]. This method requires that the signal be transformed from an RF signal to an optical signal in order to use their active cancellation techniques. Many of the active cancellation techniques throughout the co-site interference research rely on access to the transmitter signal to use for the active cancellation and cannot be used without an extremely accurate representation of the interfering signal. While the systems may be in proximity, it may not be desirable or easy to grant the receiver

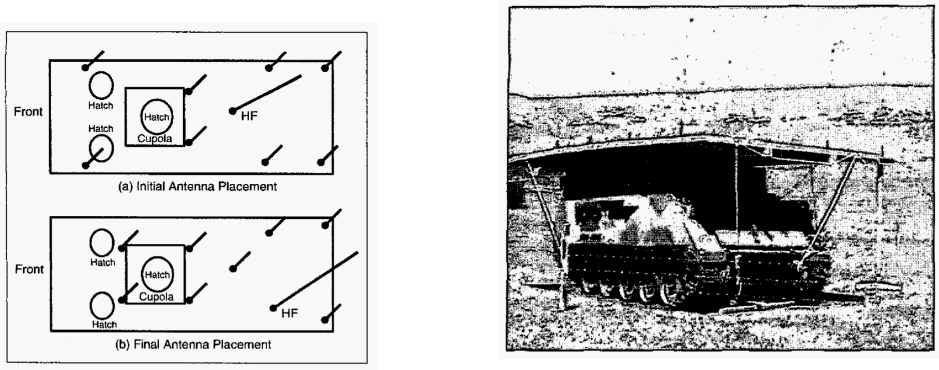

(a) Potential Antenna Placements (b) Antenna Testing Platform

Figure 2.1: Planned antenna positioning and test platform [5]

access to the transmitted interfering signal.

Another large section of co-site interference research focuses on how to simulate co-site interference patterns in order to determine performance of particular systems [8, 9, 10, 11, 12, 13]. This research, while helpful to assess interference before systems are installed, provides limited information about how to better design the systems themselves to minimize the co-site interference. The general assumption is that the antennas are given and cannot be changed. While these procedures provide valuable insight, they do not add any information about better antenna designs. These also typically focus on frequency hopping radios that operate within the same frequency bands and not multiple transmitters and receivers over a variety of frequency bands and modulation schemes, making many of the schemes hard to extend to current technologies like GPS, Wi-Fi, LTE, Bluetooth, etc. One technique was specifically built to address the interference problem between Bluetooth and Wi-Fi because the technologies both utilize the 2.4 GHz ISM band [12]. System analysis can be a useful tool to evaluate given scenarios; however, this analysis provides little insight for how to better design antenna systems for arbitrary platforms.

The current research on co-site interference also addresses the effect of moving platforms on antenna isolation and system performance. One study examined the impact of helicopter rotors on monopole antennas extending from its underside [14]. The paper shows that when the helicopter rotors are close to a half-wavelength near the frequency of interest, they will act as parasitic elements and have some effect on the antenna performance even

though the elements are on the underside of the helicopter and the helicopter is large enough at the frequency of interest for the helicopter to be considered an infinite ground plane. While the discovery of the interference is useful, the paper does not address what to do about minimizing the effect or changing the antenna design if the frequency of interest was near the frequency where the blades were a half-wavelength. Because the authors' frequency of interest did not fall in this limited band, it was not addressed.

One last area of interest within co-site interference research is active nulling. These systems actively search for the source of the interfering signal and work to put a null in that direction. Antennas that perform adaptive nulling are available but must be large in order to be able to put a null in any direction [15, 16, 17]. These systems can be overly complicated and require an active sensing of the environment. Adaptive nulling often requires either additional time or antennas in order to sense the environment and properly locate the angle of arrival of the strongest interfering signal.

While co-site interference research does provide insight into the problem with locating antenna systems in proximity, the solutions are based upon having static antenna designs and iterating through available positions. While a variety of simulation methods have been proposed, these simply evaluate the resulting interference of systems and do not provide additional insight for how to change the antenna designs to better receive all available signals. Co-site interference research focuses heavily on military communications systems. As a result, the research does not adequately address common wireless communication technologies (i.e., Bluetooth, Wi-Fi, GPS, cellular). The use of reconfigurable antennas, large filter banks, and active cancellation can be especially difficult to realize when the existing structures are smaller than current military platforms. While adding filtering and shielding does help mitigate interference significantly, the goal of the present research is to design the antennas with knowledge of the existing structure in order to best address the needs of all the RF systems required without additional filtering or shielding.

2.2 Mutual Coupling

Mutual coupling research studies the effects of having two or more antenna elements in close proximity to one another. There are a variety of different motivations for trying to understand the effects of close proximity. The goal of some of the early work on mutual coupling was to identify mutual coupling between the horn antenna and an antenna under test when trying to perform accurate gain and radiation pattern measurements [18]. Other authors looked to find accurate but efficient ways to calculate mutual coupling between antennas based on far-field patterns and relative positions of antennas [19]. Yaghjian developed a method to calculate mutual coupling by first drawing the smallest sphere that completely enclosed the antenna and then using the far-field only from solid angle of the far-fields that mutually subtended both spheres. This significantly limits the relevant portions of the far-field, especially as the distance between the two antennas increases. The only limitation is that the antennas must be in the far-field of one another for the technique to work successfully.

Mutual coupling came to the forefront especially as antenna designers began to use circuit board processes to build planar antennas like rectangular patch antennas. Designers became concerned with the amount of coupling between patch antennas over the same ground plane. Surface waves would travel along the dielectric and significantly alter the constructed antenna performance compared to the simulated performance. At first the focus was on how to model the effects of mutual coupling on the input impedance and coupling coefficients (e.g., [20]). The research provided is heavily focused on planar structures with rectangular ground planes and is not easily extendable to arbitrary structures.

To attempt to mitigate the effect of surface waves, especially on substrates with high dielectric constants, several mutual coupling mitigation techniques have been researched throughout the years. The goal is to increase the isolation between different antenna structures in order to lessen the overall impact of the substrate on antenna performance. Instead of focusing on the original design of the antennas themselves, the research alters preexisting traditional antenna designs after they have been installed and performance has been shown to be insufficient. For many antenna designs, electromagnetic bandgap (EBG) structures have been developed to reduce the surface waves and

thus the mutual coupling [21]. Another solution was to connect antenna designs at low voltage and field points in order to maximize isolation and reduce crosstalk between planar inverted-f antennas mounted to the same chassis [22]. Other studies use slots or other obstacles in the ground plane to keep the ground plane from increasing the crosstalk between multiple antennas [23]. While these techniques do increase isolation and mitigate crosstalk, they require additional work above and beyond the initial design of the elements. Some of the methods also keep the elements from exciting the ground plane as a means to reducing crosstalk [23, 24, 25, 26, 27]. Because the ground plane is no longer being excited, it does not allow for the increased gain and bandwidth that often come from utilizing all existing metallic structures to radiate.

2.3 MIMO

Recently mutual coupling research has focused on understanding mutual coupling in order to better design antennas for MIMO applications. Because MIMO antennas can be closely spaced and need high levels of isolation, increased isolation between antennas in order to increase channel capacity becomes a priority. MIMO antennas perform best when the correlation between the signals on separate antennas is low. Antenna properties like pattern, polarization, array configuration, and mutual coupling can greatly impact the correlation between the signals on different antennas [28]. Because the main goal for MIMO antennas is increased channel capacity, some authors focused on reporting the effects of mutual coupling on capacity and verifying the detriments of mutual coupling to MIMO antenna performance [29]. Based on other relevant research about isolation, researchers compiled a list of design rules that are relevant to MIMO antenna systems [30]. Because the design rules were developed by running several studies and focusing on increased isolation, the rules only apply in situations where isolation between antenna ports at a single frequency is the main concern.

One of the most common methods for achieving capacity improvement is by adding multiple antennas that are spatially isolated or have different polarizations. However, spatial isolation is not always an option for attempting to create isolation. Also, because mutual coupling occurs through surface

waves, radiation, and a variety of other factors, simple spatial separation does not fully describe the best positions for minimizing mutual coupling between MIMO antennas. Much like co-site interference, in addition to spatial separation, decoupling networks are also employed. These networks are narrowband in nature and can exhibit large losses that can be extremely detrimental to mobile systems [31].

Much of the research with MIMO has to do with minimizing mutual coupling. There are a variety of methods antenna designers have used to minimize and mitigate the effects of mutual coupling. Many of the designers use parasitic and coupling elements [32]. Designers can also create parasitic or coupling elements by altering the ground plane. Zhang et al. add a thin resonant slot between two planar inverted-F antennas in an array to significantly reduce the mutual coupling between the elements of the array [33]. The resonant slot in the ground plane keeps the elements from using the entirety of the ground plane to radiate, trading off some reduced gain and bandwidth for increased isolation between the two PIFAs. The change in the ground plane is also addressed in the study of defected ground plane structures [23, 24, 25, 26, 27].

Some groups look to create multiple antennas that are completely decoupled because they serve different frequency bands with steep roll-off to ensure the antenna does not perform well out of its intended frequency band [31]. Separating the elements in the band does reduce the mutual coupling but there is not always enough space for the approach suggested.

Other designers use reconfigurable antennas to try and increase the capacity and diversity by changing the antenna pattern based on the channel statistics [34, 35]. The ability to dynamically alter the antenna patterns can change system performance greatly without having to install more antennas. While reconfigurable antennas cause added complexity, they also allow the designer to alter the functionality/performance in situ. The ability to reconfigure antenna patterns also typically comes with larger loss which would be unacceptable in mobile systems where power consumption is important.

Recently with the resurgence of research in characteristic mode theory, which will be explained in more depth later, antennas are designed that couple into orthogonal modes in order to create higher isolation in small spaces [36, 37]. Because the antennas use orthogonal operating modes, it becomes possible to achieve high isolation with little physical separation.

It is only possible to use characteristic modes for this MIMO optimization when there are two or more modes that radiate well at a single frequency on a specific platform.

Overall many different antennas for a variety of platforms have been created for MIMO applications [38, 39]. These antennas seek to use the available effective area in order to greatly increase the capacity of a system. The increased capacity is only achieved when several antennas that are tuned to the same frequency are able to operate with high isolation and low mutual coupling. Much of the research into MIMO antennas attempts to reduce mutual coupling but does not fully address the problem of designing antennas based on knowledge of the platform and the desired radiation pattern. Especially for the design methodologies for MIMO that use characteristic mode theory, the orthogonal modes effectively ensure that the different antennas radiate differently in any particular direction. While this is desirable to increase gains due to diversity, it may not be ideal for all antennas being attached to a platform.

Co-site interference, mutual coupling, and MIMO research all are relevant to developing a synthesis procedure for antennas on a platform based on radiation pattern; however, the research does not adequately address all of the concerns with the design of multiple antennas. While some studies are being done to compare the spatial efficiency required of multiple antennas, there is little research into how to design based on radiation pattern and a particular platform [40]. Also many of the techniques used to achieve isolation ensure that the ground plane does not radiate, limiting the efficiency, gain, and bandwidth of the installed antennas. Co-site interference, mutual coupling, and MIMO antenna research provides an excellent starting point for developing a synthesis procedure based on antenna pattern performance of multiple antenna elements on an existing platform. To begin to develop the synthesis procedure, this research will first focus on how to feed and excite a certain pattern on a preexisting structure. The next chapter discusses characteristic mode theory and how that can be applied to existing structure geometry to inform the choice of feed position and antenna element.

CHAPTER 3

IDENTIFYING FEED POINT AND EXCITATION ON AN EXISTING PLATFORM

The feed point and antenna element can greatly impact the radiation pattern and other properties of the radiating system based on how they excite the existing structure. Some previous research has focused on how to find an appropriate feed point on an existing structure. In 1979, one of the earliest papers showed that, by using the theory of characteristic modes, the efficiency of small antennas could be increased by placing it properly on the existing structure [41]. Newman models an airplane as a wire cross and uses characteristic modes to find the placement that optimizes the radiation resistance of a small loop. The paper relies on the structure having a few modes close to resonance near the frequency of interest [41].

In 1992, Murray and Austin also used the theory of characteristic modes to place an HF antenna on a Humvee for use with NVIS communication systems [42]. Traditionally installed mobile HF antennas were monopoles attached to the vehicle that had nulls facing the sky that were not sufficient for skywave communication. Murray and Austin used characteristic modes to better understand where to attach and how to design an antenna that would radiate skyward. Later, further papers were written that explained how they were able to model the vehicle on a wire grid and compute the characteristic modes using the method of moments [43, 44]. The wire grid and resulting antenna can be seen in Figure 3.1.

Characteristic mode theory was not the only theory used to evaluate possible positioning of antennas on platforms. Huff et al. performed an electromagnetic visibility study (EVS) on a laptop to evaluate candidate positions [45]. The structure under test is excited by plane waves from all possible incoming wave directions and polarizations and then the magnitude of the steady state induction current is calculated. By using averaging, it is possible to find zones with higher and lower current. The sections with higher on average conduction current indicate the structure is more likely to assist

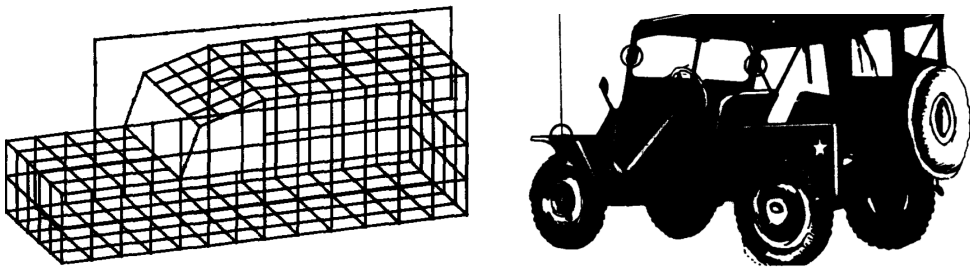

(a) Wire Grid Model (b) Resulting Antenna on Vehicle

Figure 3.1: Designed HF antenna based on wire grid model and characteristic mode analysis [42, 43]

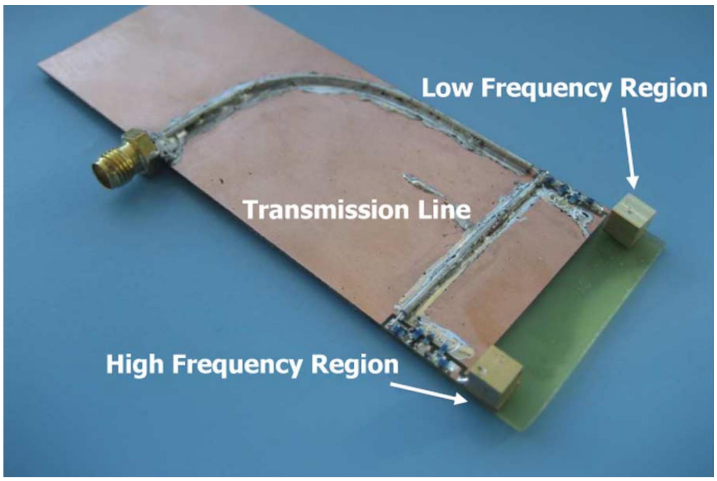

Figure 3.2: Example of ground plane booster technology [2]

with radiation if the antenna is placed in proximity to that location.

Other antenna designs simply use matching networks with a small coupling element to excite the existing structure [2]. While the matching networks are compact compared to similar antennas for the same frequency, the matching network suffers from loss in the circuit elements. The radiation pattern of the antenna does not differ significantly from the radiation pattern associated with the ground plane. Figure 3.2 shows how small ports can be added as matching networks to a ground plane-like structure in order to force radiation in particular frequency bands.

Recently authors are still using the theory of characteristic modes to better

understand proper antenna placement as well as possible radiation patterns for a structure. Even today antennas are being designed to have pattern diversity or superior performance when placed on a UAV [46, 47].

Many of the articles on antenna placement utilize the theory of characteristic modes. In addition to being utilized by antenna placement research, characteristic mode theory is also used to improve isolation for MIMO antennas. Because of the prevalence of the theory in both antenna placement and MIMO performance optimization, it is a natural foundation for an antenna synthesis procedure that designs antennas to install on an existing platform. The theory uses the geometry of the existing structure to better understand how the object will radiate. Because of its application to placement, the theory of characteristic modes will be discussed more in depth in the next section.

3.1 Theory of Characteristic Modes

Characteristic mode theory was introduced in 1971 by Garbacz and Turpin explaining how a structure supported nonphysical modes, independent of the excitation, that could be used to estimate antenna performance [48]. Harrington and Mautz expanded on the theory of characteristic modes by demonstrating that the solution for the modes could be found using an eigenvalue problem and could be solved using the method of moments [49]. The theory uses the method of moments impedance matrix, Z, which can be decomposed into its real and imaginary parts:

$$[Z] = [R] + j[X]. \tag{3.1}$$

Harrington and Mautz derived equations relating R, X, eigenvalues (λ_n), and modal currents (J_n) that can be summarized as

$$X\left(J_n\right) = \lambda_n R\left(J_n\right). \tag{3.2}$$

Using Equation 3.2 and the impedance of the antenna, it is possible to find the modal currents and eigenvalues. The modal currents and the eigenvalues relate to the total current on the structure using Equation 3.3, where V_n^i are the modal excitation coefficients and can be found using Equation 3.4, where

J^i and M^i are the magnetic and electric currents that generate the incident electric and magnetic fields, respectively, and E_n and H_n are the electric and magnetic fields, respectively, resulting from modal current J_n:

$$J = \sum_n \frac{V_n^i J_n}{1 + j\lambda_n} \tag{3.3}$$

$$V_n^i = \iiint_V E_n \dot{J}^i - H_n \dot{M}^i. \tag{3.4}$$

Recently, the theory of characteristic modes was revisited and applied directly to plates and antennas in a comprehensive review [50]. The value of λ_n indicates how well the mode radiates. The larger the magnitude of λ_n, the more energy stored in the mode. The sign of λ_n indicates the type of energy storage associated with the mode. When λ_n is positive, the energy storage mode is inductive and when λ_n is negative, the mode is capacitive. When λ_n equals 0 the mode is resonant on the structure at that frequency. To better visualize λ_n, modal significance is defined by

$$MS = \left| \frac{1}{1 + j\lambda_n} \right|. \tag{3.5}$$

MS also reflects how well the mode radiates. As MS approaches 1, the mode radiates more energy and as MS approaches 0, the mode is storing more energy instead of radiating. Another important quantity for visualizing the modal structure is the characteristic angle, θ_n, which is defined as

$$\theta_n = 180^\circ - \arctan(\lambda_n). \tag{3.6}$$

The characteristic angle is 180° when the mode is resonant, so that when a mode is radiating θ_n is close to 180°. Characteristic mode theory allows modes to be found on the structure independent of the excitation. Because it is independent of the excitation, the theory allows the ground plane modes to be evaluated separately from the modes on the antenna element and the modes of the entire antenna structure.

The fields are linearly related to the currents and can also be expressed in modal form as

$$E = \sum_n \frac{V_n^i E_n}{1 + j\lambda_n} \tag{3.7}$$

$$H = \sum_n \frac{V_n^i H_n}{1 + j\lambda_n} \tag{3.8}$$

where E and H are the fields from J and E_n and H_n are the modal fields corresponding to J_n. The coefficients for the linear superposition can be determined once an excitation is decided. Therefore the total current and field quantities can be written as

$$J = \sum_n \alpha_n J_n \tag{3.9}$$

$$E = \sum_n \alpha_n E_n \tag{3.10}$$

by defining α_n as

$$\alpha_n = \frac{V_n^i}{1 + j\lambda_n} \tag{3.11}$$

where α_n are the modal weighting coefficients corresponding to each mode. The eigencurrents are of indeterminate amplitude so then it is important to normalize the current such that

$$< J_n^*, RJ_n >= 1. \tag{3.12}$$

With this normalization, the orthogonality relationships for the eigencurrents become

$$< J_m, RJ_n >=< J_m^*, RJ_n >= \delta_{mn} \tag{3.13}$$

$$< J_m, XJ_n >=< J_m^*, XJ_n >= \lambda_n \delta_{mn} \tag{3.14}$$

$$< J_m, ZJ_n >=< J_m^*, ZJ_n >= (1 + j\lambda_n)\delta_{mn}. \tag{3.15}$$

When the characteristic fields are determined based on the modal currents, the set of all E_n form a Hilbert space of all fields. We can then evaluate the fields on the sphere at infinity, S_∞. Because of the orthonormality of the modal currents, the characteristic far fields can also be determined to be orthonormal. Because of the relationship between modal current and characteristic far-fields,

$$\frac{1}{\eta} \oiint_{S_\infty} E_m \cdot E_n^* ds = \delta_{mn} \tag{3.16}$$

creating an orthonormal set. The properties of the modal currents and cor-

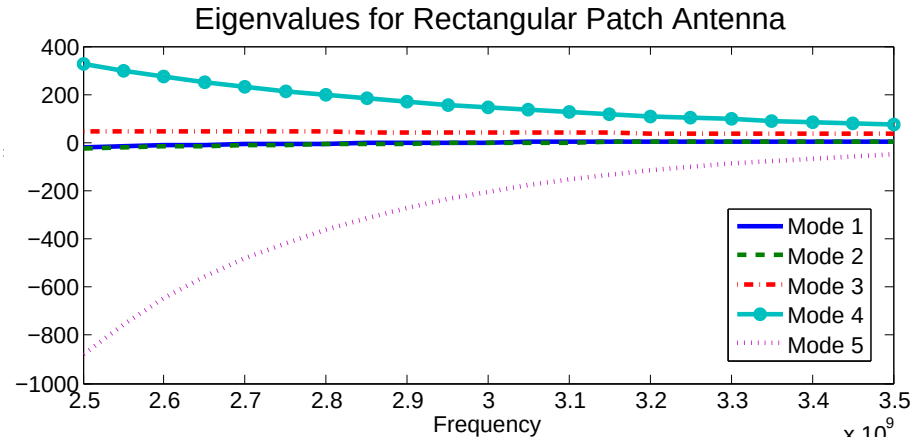

Figure 3.3: Eigenvalues of the first 5 modes for the rectangular patch antenna

responding characteristic far-fields enable the theory of characteristic modes to provide insight on possible radiation patterns based on the geometry of the structure.

3.1.1 Rectangular Patch Antenna

As a simple example, the characteristic modes on a rectangular patch antenna over an infinite ground plane are evaluated. The patch is 0.465λ in length with a center frequency of 3 GHz. Figure 3.3 shows the eigenvalues of the patch antenna over frequency and Figure 3.4 shows the corresponding modal significance. Figure 3.5 shows the surface current corresponding to the first five modes as well as the total current on the patch once it is fed. The first mode has current that runs primarily along the x-axis while the second mode runs primarily along the y-axis. The third mode has current that runs radially outward from the feed point while the fourth mode is circulating about the center of the patch.

Each modal current corresponds to a characteristic far-field. Figure 3.6 shows corresponding far-fields to the surface currents shown in Figure 3.5. Figure 3.6(f) shows the far-field corresponding to the rectangular patch antenna once a feed is added.

From characteristic mode theory, the structure along with the feed can be used to calculate the modal weights and modal excitation coefficients. Figure 3.7 shows the magnitude of the modal weighting coefficients for the

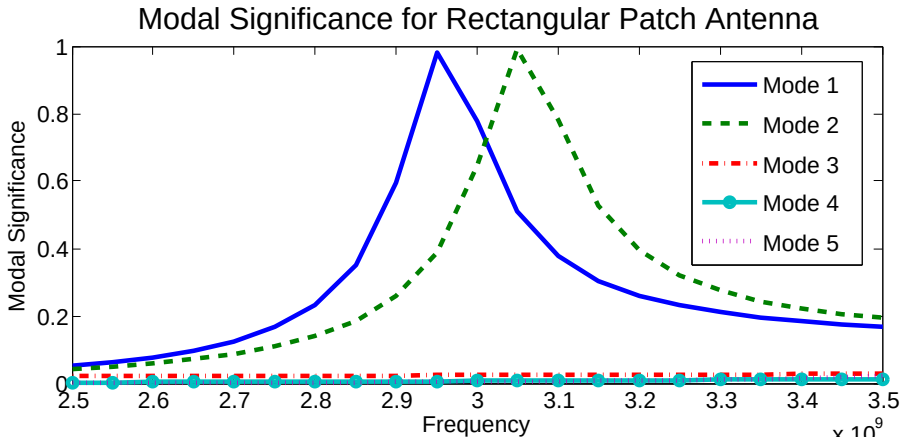

Figure 3.4: The modal significance of the first 5 modes for the rectangular patch antenna

patch antenna. Examining Figure 3.7, modes 2 and 3 are the only modes with non-zero weighting coefficients and the total current and far-field are mainly comprised of input from mode 2 and a much smaller contribution from mode 3. These figures show the relationship between the modal characteristics and the total current and far-field.

3.2 Sample Geometries

When there is an existing structure, typical research focuses on feeding resonant modes or making modes resonant so that they can be utilized as efficient radiating modes. Unfortunately, it is not always possible to alter an existing structure to change the frequency where the mode resonates. It is also possible that the radiation pattern corresponding to a non-resonant mode is the pattern best suited for the application. It then becomes important to understand how to best feed the structure and design an element that will excite the desired mode on the existing structure.

A three-sided box with dimensions 0.5λ x 0.25λ x 0.2λ was modeled in FEKO® and characteristic modes evaluated. Figure 3.8 shows the modeled box when the center frequency is 600 MHz.

Figure 3.9 shows the plot of the eigenvalues corresponding to the first nine modes on the structure. To better visualize how well each mode is radiating, Figure 3.10 plots the modal significance corresponding to the first nine modes on the structure. At 600 MHz, six modes have a modal significance around

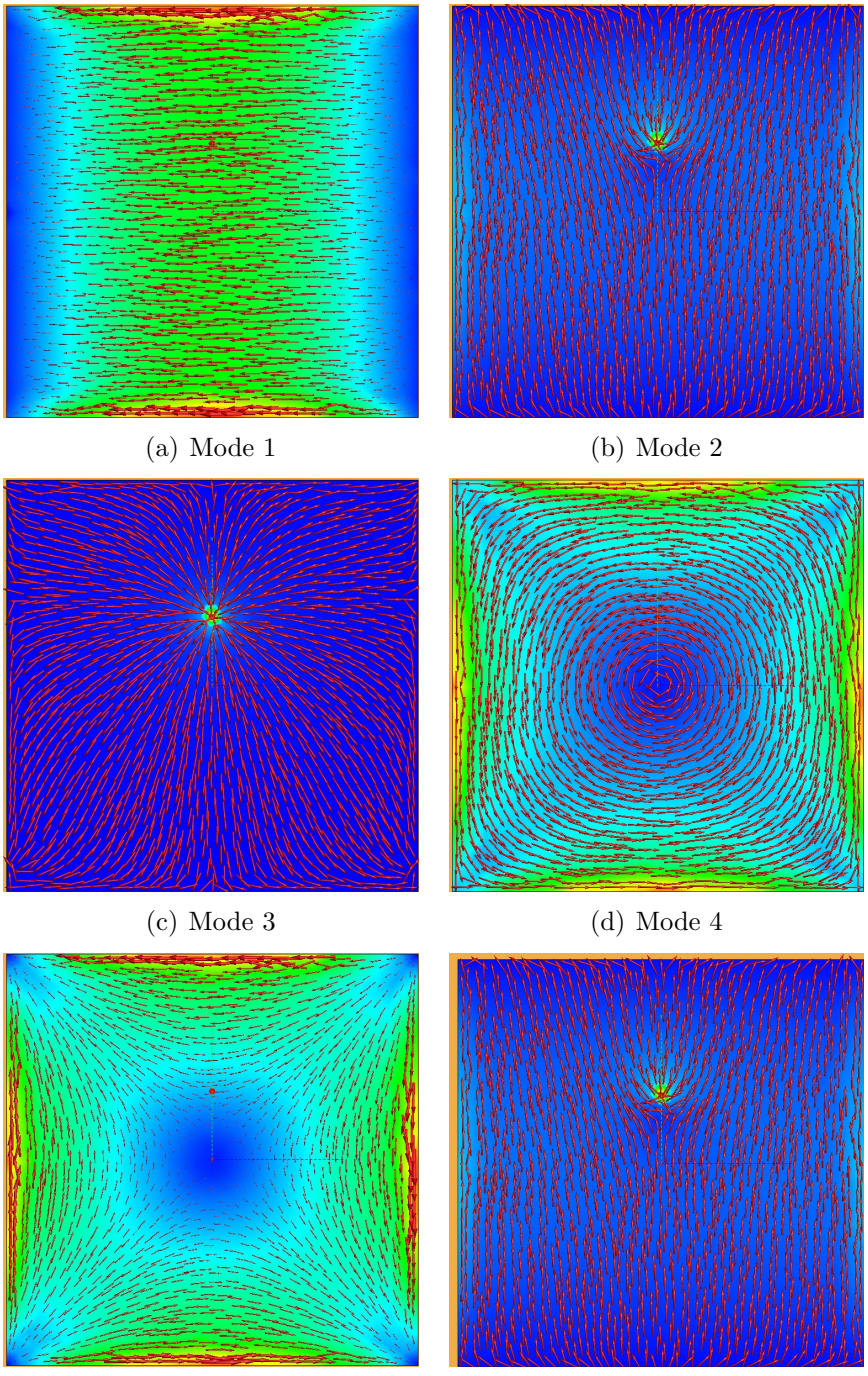

(a) Mode 1 (b) Mode 2

(c) Mode 3 (d) Mode 4

(e) Mode 5 (f) Total Current

Figure 3.5: Surface currents on a rectangular patch over an infinite ground plane at 3 GHz

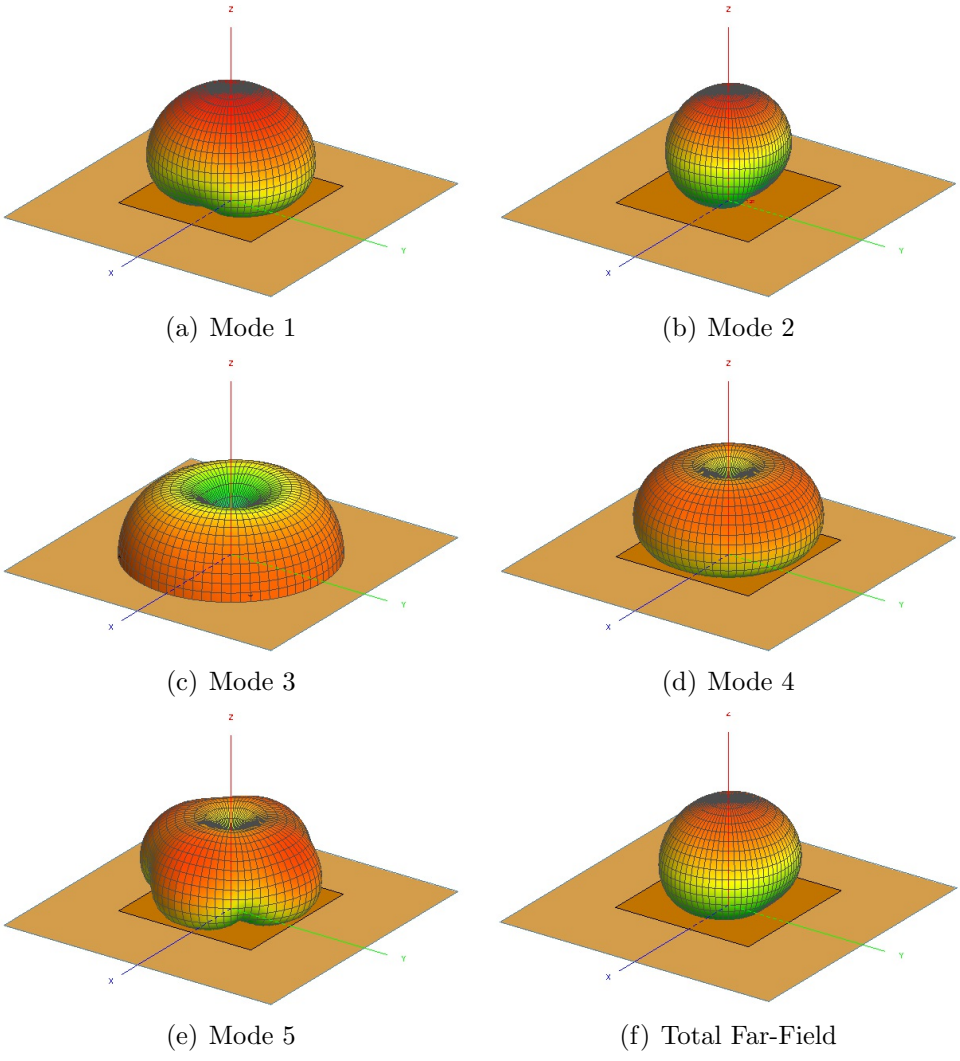

(a) Mode 1 (b) Mode 2

(c) Mode 3 (d) Mode 4

(e) Mode 5 (f) Total Far-Field

Figure 3.6: Characteristic far-fields corresponding to the modal currents for a rectangular patch over an infinite ground plane at 3 GHz

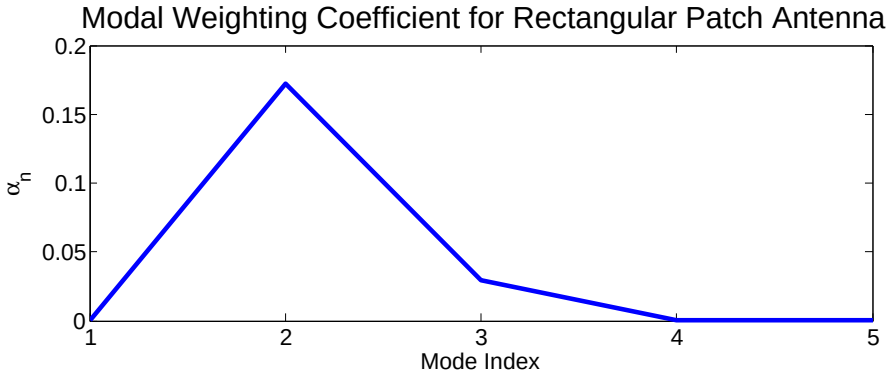

Figure 3.7: Magnitude of the modal weighting coefficients of the first 5 modes for the rectangular patch antenna

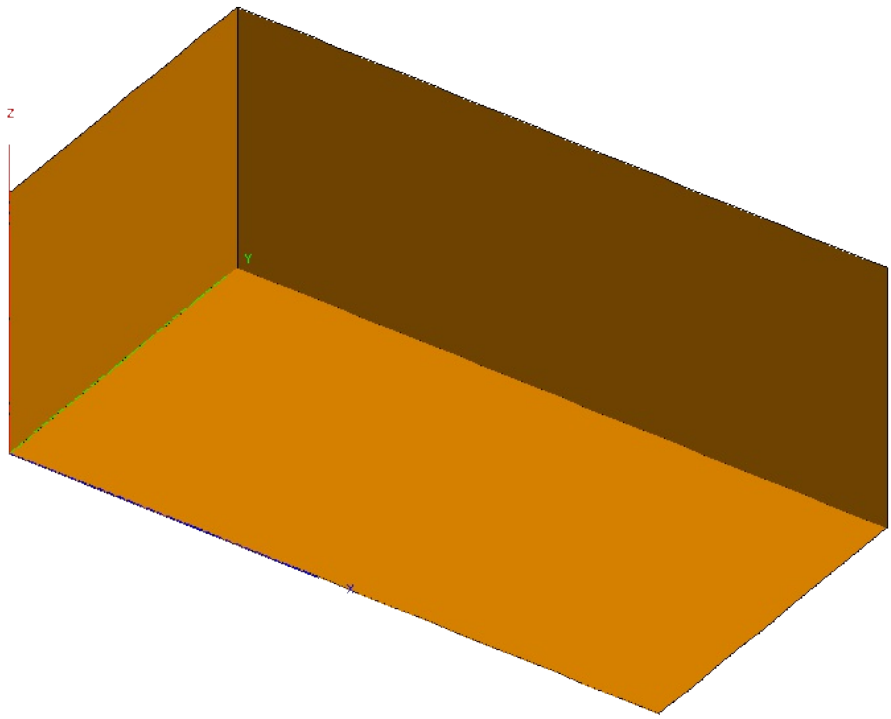

Figure 3.8: Three-sided box with dimensions 0.5λ x 0.25λ x 0.2λ and a center frequency of 600 MHz

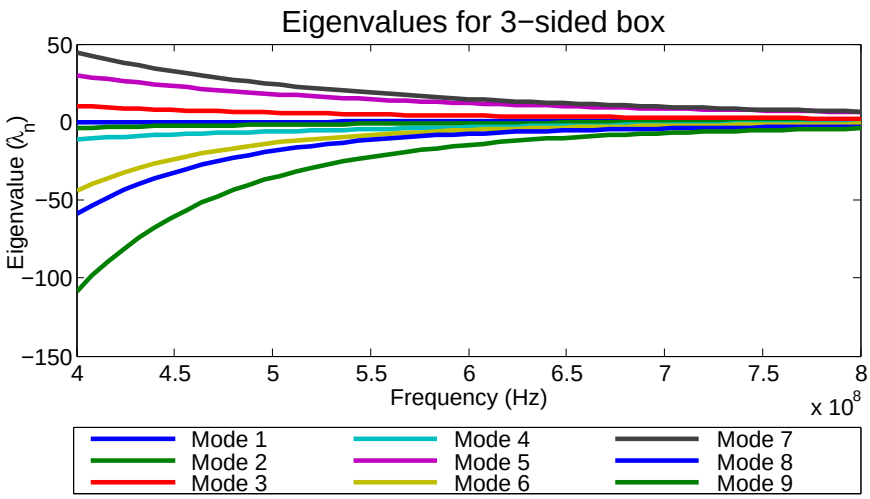

Figure 3.9: Eigenvalues for first 9 modes on a three-sided box

0.1. All higher modes have smaller modal significance values at the frequency of interest. The modal currents and characteristic far-fields corresponding to the first six modes on the three-sided box are shown in Figures 3.11 and 3.12.

It may be possible to gain additional insight by examining the modes on a second structure, so the characteristic modes on a five-sided box were evaluated. The five-sided box was also 0.5λ x 0.25λ x 0.2λ and evaluated at 600 MHz. Figures 3.13 and 3.14 show the eigenvalues and modal significance for the modes on five-sided box. More modes are shown on the modal significance plot above 540 MHz to confirm all modes with modal significance above 0.1 at 600 MHz were included in the calculations. Because the structure has more metal, there are more modes that are closer to resonance at 600 MHz. Overall, however, there are still only a few significant modes.

The modes on the five-sided box can be compared to the modes on a rectangular plate [51]. The modal far fields and surface currents are shown in Figures 3.15 and 3.16 respectively. The first mode has surface currents that run parallel to the longest side of the plate. The second mode's corresponding surface current runs primarily parallel to the shorter side. Like the rectangular plate, the five-sided box's first mode is primarily along the outside of the longest side. The second mode is primarily along the second longest side. Because the five-sided box is three-dimensional instead of two, the next mode is parallel to the shortest dimension. The three-sided box shows similar patterns in its modal current structures for the first three modes. The

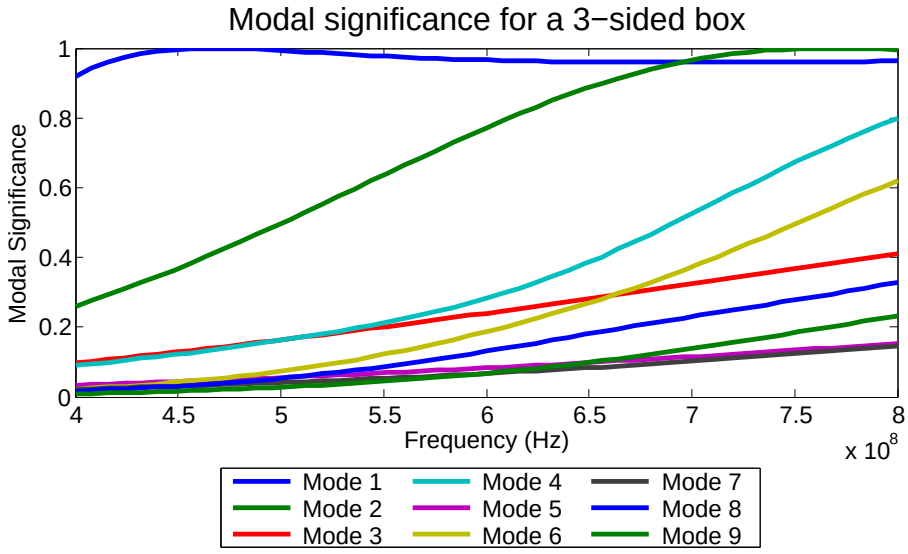

Figure 3.10: Modal Significance for first 9 modes on a three-sided box

next modes on the three-sided and five-sided box provide circulating currents about a center point very similar to the currents for the third mode on the rectangular plate. As the mode number increases, the modes start to have nulls for the plate, the three-sided box, and the five-sided box. Even with more complex geometry, there are similarities to simplified geometric shapes.

Typically references show that high current points at the mode of interest are where the structure should be fed [42, 43]. Looking at Figure 3.11, it is noticeable that different modes have markedly different surface currents but that the current maximums between modes occasionally overlap. For example, modes 1 and 3 have high current along the outer edge of the longest side of the box. Because of the overlapping current maximums, it is difficult to pick a feed point location simply by looking at pictures depicting the modal surface current. Because mode 1 has a higher modal significance, if a current maximum for both modes 1 and 3 is fed, the dominant pattern will be that of mode 1 with very little impact from mode 3. If mode 3 is the desired mode and far-field pattern, it becomes more difficult to understand where to place the feed point in order to approach the pattern of the mode of interest. It is important to find the feed position that limits the interaction between the mode of interest and other significant modes. By optimally placing the feed point, it may be possible to create a pattern that most closely resembles

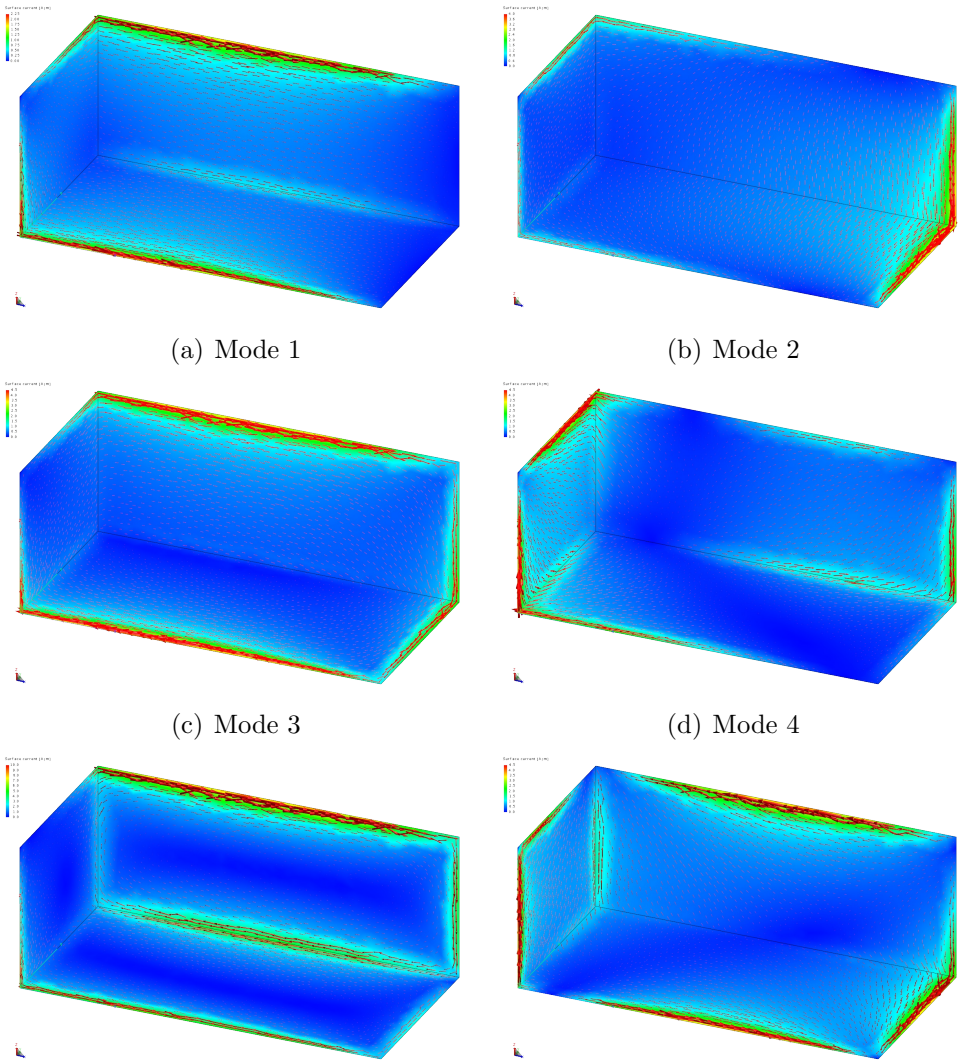

(a) Mode 1

(b) Mode 2

(c) Mode 3

(d) Mode 4

(e) Mode 5

(f) Mode 6

Figure 3.11: Modal surface currents corresponding to the first six modes on the three-sided box

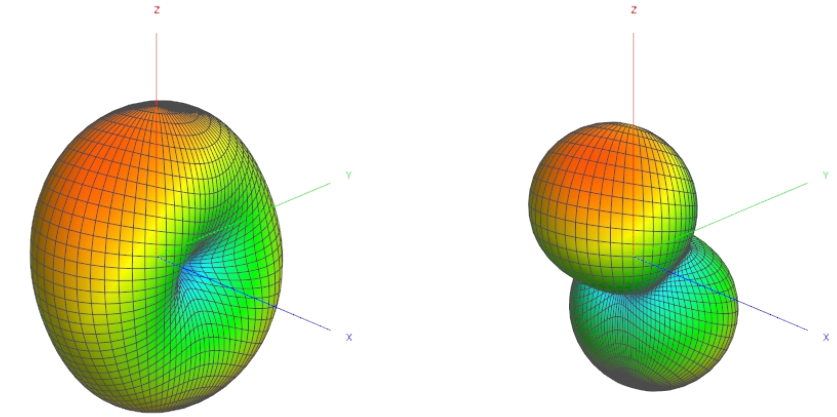

(a) Mode 1

(b) Mode 2

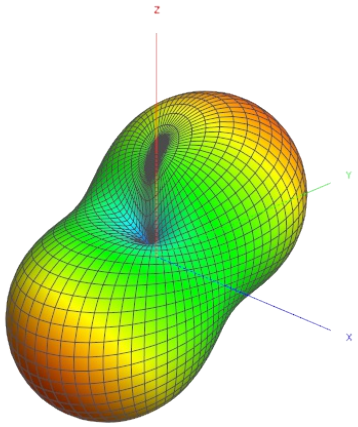

(c) Mode 3

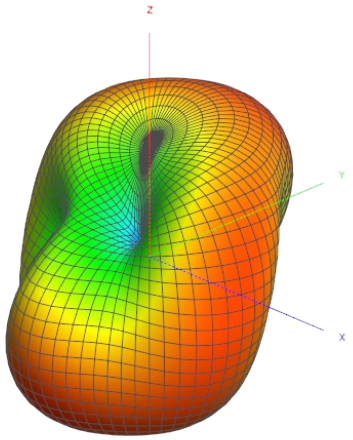

(d) Mode 4

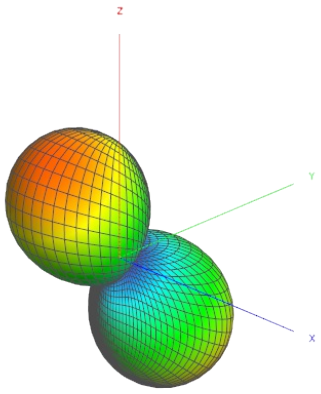

(e) Mode 5

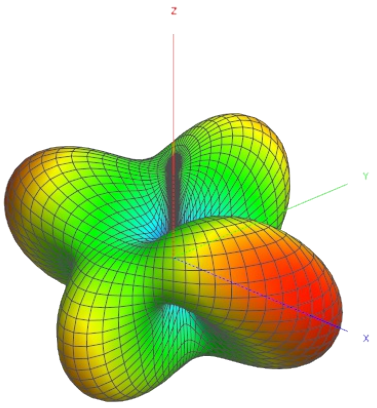

(f) Mode 6

Figure 3.12: Characteristic far-fields corresponding to the modal currents for a three-sided box at 600 MHz

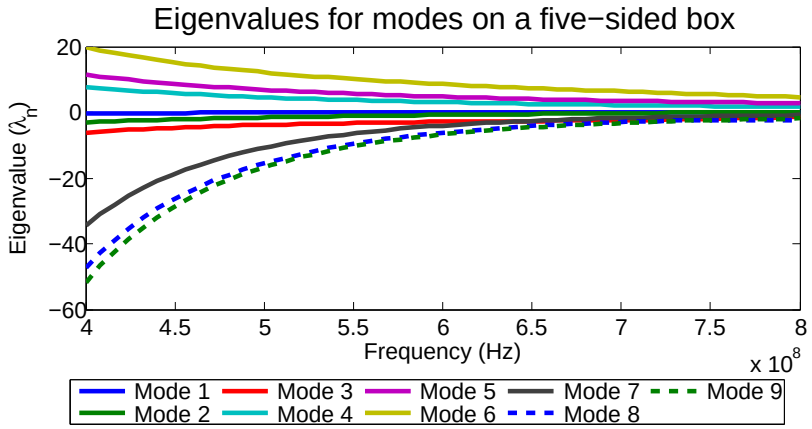

Figure 3.13: Eigenvalues for first nine modes on a five-sided box

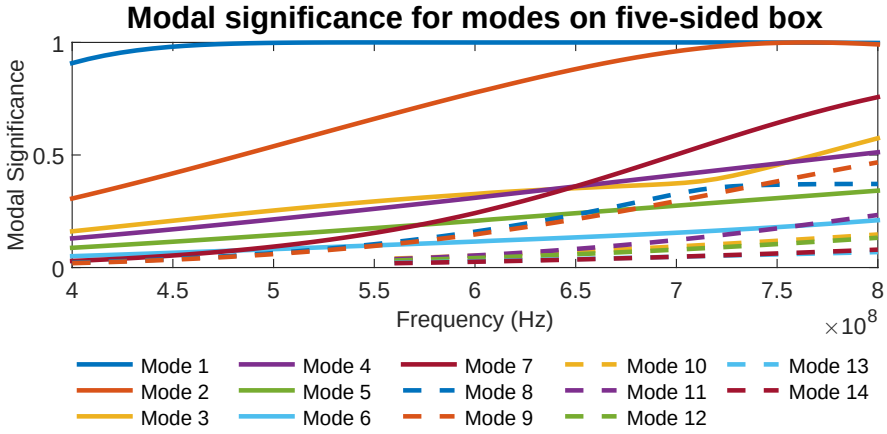

Figure 3.14: Modal significance for modes on a five-sided box

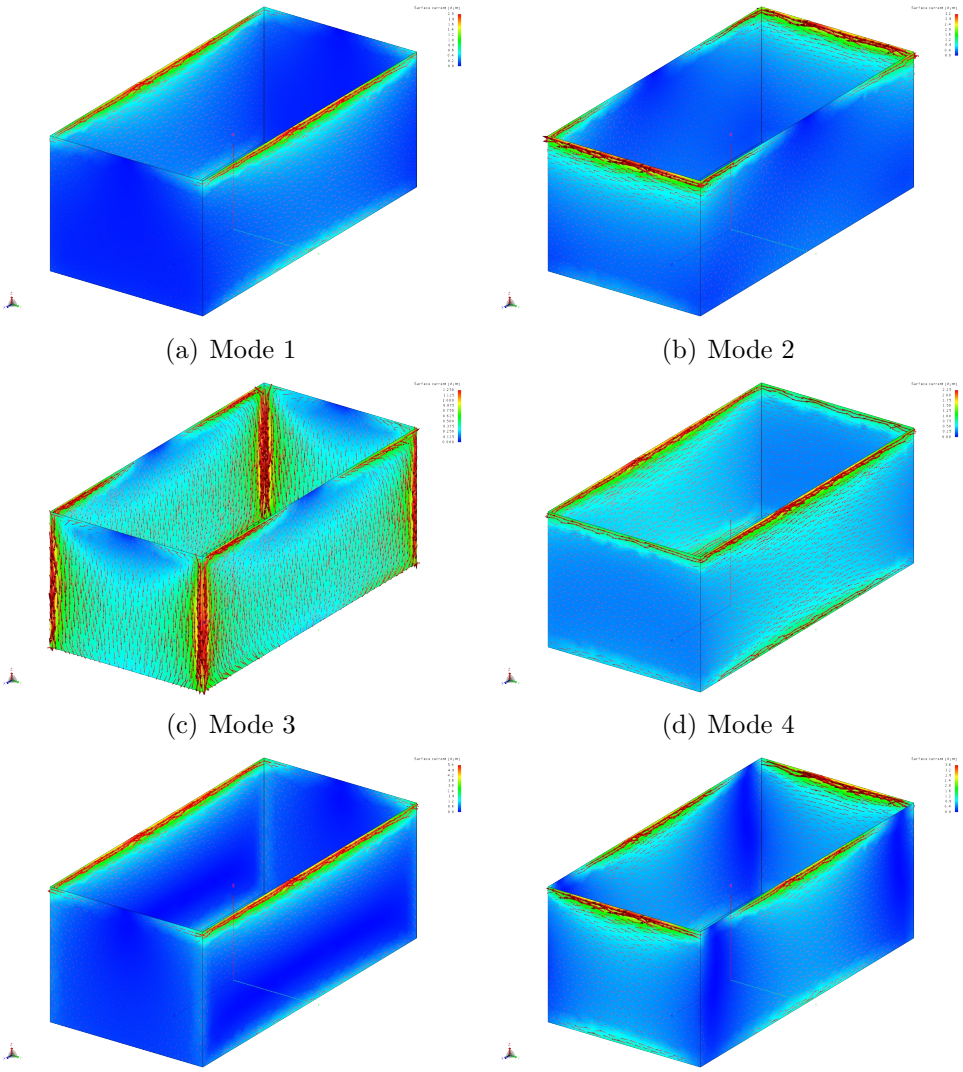

(a) Mode 1 (b) Mode 2

(c) Mode 3 (d) Mode 4

(e) Mode 5 (f) Mode 6

Figure 3.15: Modal surface currents corresponding to the first six modes on the five-sided box

mode 3 instead of mode 1.

To find the best excitation points, a comparison must be created to ensure that the chosen mode has the highest modal current at that point in relation to the other primary modes on the structure. This comparison allows the designer to choose a feed point and design the corresponding element. Because an element or a slot must be created in the existing structure in order to excite the existing structure, there is no need to worry about impedance matching at this stage.

The choice of desired mode can be made by studying the corresponding modal far-fields. For now, the assumption is that one mode on the structure corresponds to the needed far-field. The next chapter will address pattern synthesis for when no single characteristic far-field corresponds to the goal radiation pattern. There are two distinct methods for comparing modal currents and attempting to find the excitation point. Because modal currents are orthogonal over the entire surface and not point-wise, it may be important to take into account directionality when examining surface current to determine feed placement.

Taking into account the direction and magnitude of the normalized modal currents, the placement of the feed can be found by finding the point on the structure where

$$\sum_{m}^{m\neq i} J_m \cdot J_i - |J_i|^2 \tag{3.17}$$

is minimized where i denotes the index of the desired mode.

The other option is to not take into account the direction of the current at any particular point and just compare current magnitude. For this procedure

$$\sum_{m}^{m\neq i} |J_m|^2 - |J_i|^2 \tag{3.18}$$

is minimized to ensure that the feed point is where mode i is maximized compared to all other available and significant modes. Using only the magnitude can be a direct benefit when adding elements because it ensures that if small amounts of current are put in orthogonal directions, they are not significantly amplifying modes with higher modal significance than the mode of interest.

The two methods for determining feed point location were evaluated on

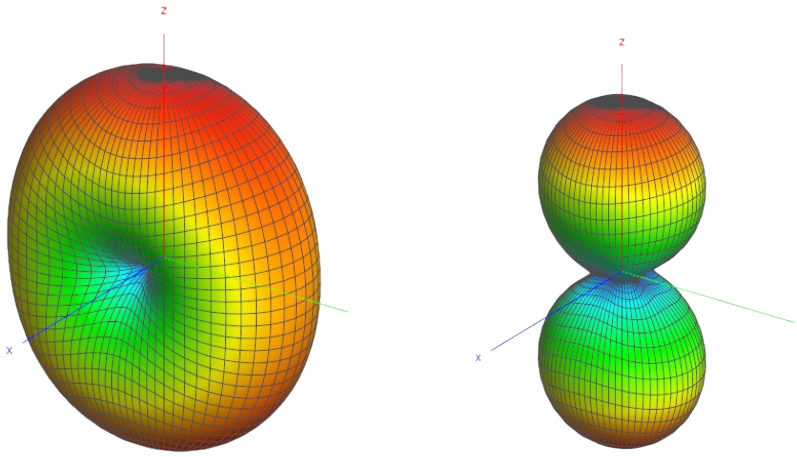

(a) Mode 1

(b) Mode 2

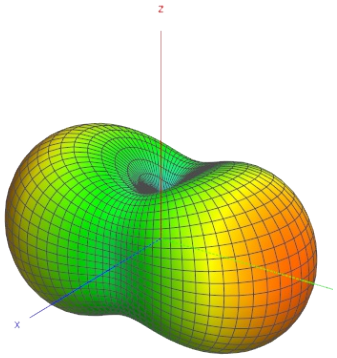

(c) Mode 3

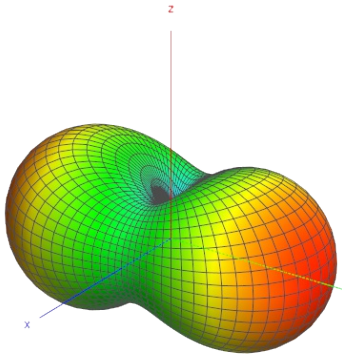

(d) Mode 4

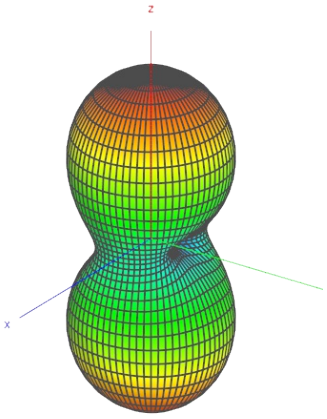

(e) Mode 5

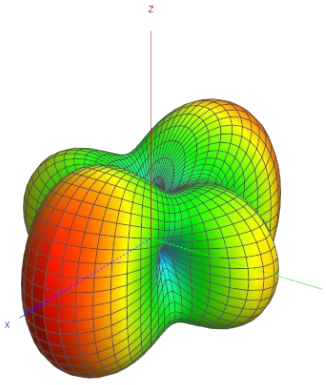

(f) Mode 6

Figure 3.16: Characteristic far-fields corresponding to the modal currents for a five-sided box at 600 MHz

the three-sided box first. Both methods were used to find the point on the three-sided box that should be used to excite the third mode. The feed point location returned is limited by the size of the mesh used when evaluating the surface currents and the modes on the structure. The nodes of the mesh are the only places recognized as potential placements for the feed point. Again, these methods do not take impedance into account because antenna elements will be added to the structure and those can be used for impedance matching. In this example, the results of running the minimization based on direction and magnitude or just magnitude were identical. The chosen feed point is on the outside corner of the structure along the z-axis as shown in Figure 3.17.

One example does not verify that this is always the case. It is possible that for different geometries, the two methods may deliver slightly different feed points. The five-sided box was then evaluated to find the appropriate feed points for the third mode. First, the calculation was completed when magnitude and direction were taken into account. It was then run again with only magnitude. The two output positions were still on the z-axis as with the three-sided box. The positions were not exactly the same; however, they were only one node apart. Figure 3.18 indicates the feed points on the five-sided box. Comparing the values given by Equations 3.17 and 3.18 at each mesh node, the two nodes have similar values and differ by small amounts. Therefore, while the exact position is different, the point is the same. Because the five-sided box is symmetric, each corner was a potential feed-point for the box. The slight variation in the meshing caused the program to output points only on the z-axis.

By studying the feed placement in relation to the desired modal surface current, it is clear the feed placement is not necessarily the highest current position for the desired mode. Both methods for computation result in similar outputs for the feeding position regardless of whether direction is taken into account. Although the feed placement site has now been chosen, it is also important to discuss the excitation needed to generate the needed current distribution. Simply feeding in the correct position does not impedance match the structure or ensure that needed current distribution will exist on the structure. The next step in designing the antenna system is to design an element that impedance matches the structure and results in a radiation pattern close to the desired pattern. The next section will provide an exam-

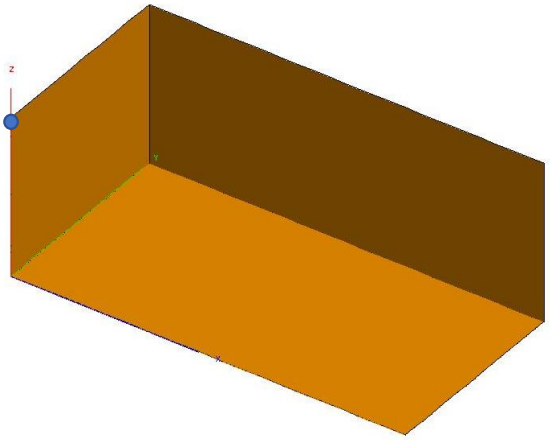

Figure 3.17: Feed point designated by both algorithms for the three-sided box is marked by a blue dot

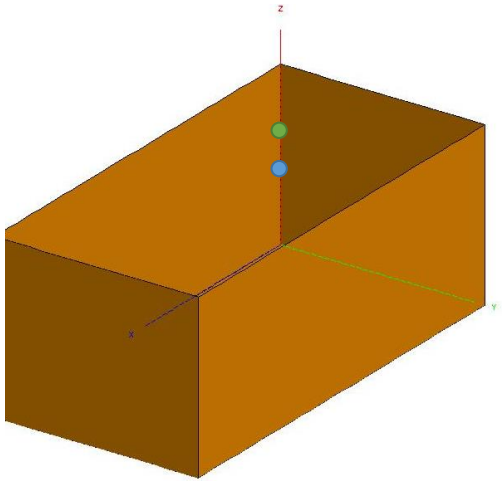

Figure 3.18: Possible feed points are marked on the five-sided box. The blue dot signifies the feed position using both magnitude and direction while the green dot signifies the feed position when using only magnitude.

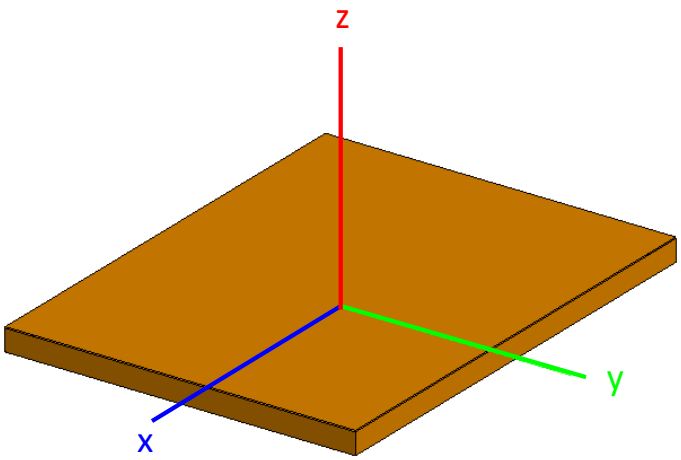

Figure 3.19: Modeled six-sided box being used as the existing structure

ple using the design methodology provide in this section. The example goes through the process of solving for the modal far fields and using the analysis to determine the feed point and design an element to excite the mode of interest.

3.3 Example Implementation

A six-sided box with a small slit around three sides on the top will be used as the existing structure for this example. The goal is to install an antenna along the top of the box at a center frequency of 400 MHz in order to produce a radiation pattern that allows for most of the power to radiate in the $x-y$ plane with almost no power radiating along the z-direction. Any additional metal should also add minimal volume to the original structure. The box is 32cm x 24.5cm x 1.5cm which is equivalent to 0.427λ x 0.327λ x 0.02λ. The model of the existing structure is shown in Figure 3.19.

The eigenvalues and modal significance of the first seven modes are shown in Figures 3.20 and 3.21. Because the length and width are close in size, the first two modes follow very similar trajectories. As before these modes correspond to particular far-field patterns. The far-field patterns are shown in Figure 3.22. Using the earlier described scenario where the power from

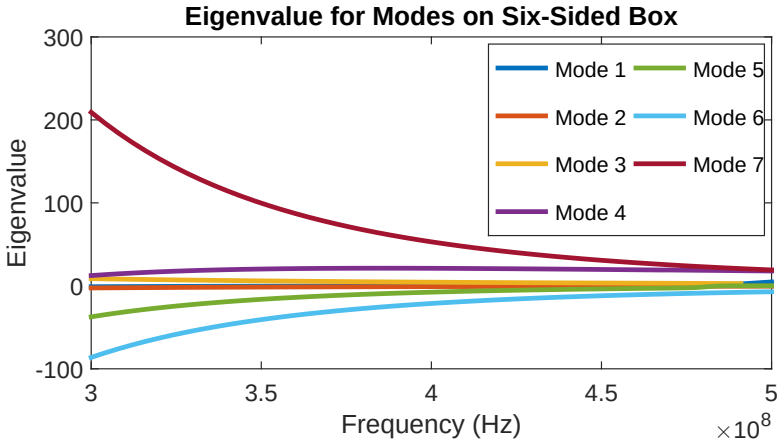

Figure 3.20: Eigenvalues for first 7 modes on a six-sided box

the antenna needs to radiate primarily along the $x-y$ plane, the desired modal pattern is from mode 3. From Equation 3.21, it can be seen that at the center frequency of 400 MHz, the modal significance is much lower than that of the lower modes. Thus it will be more difficult to make the third mode radiate and it will likely be mixed with some of the first two modes. Higher order modes do have some radiation in the $x-y$ plane; however, they also have nulls. Exciting these higher order modes may lead to nulls in the resulting pattern which are detrimental.

Based on the choice of the third mode as the desired mode, the modal surface currents at the frequency of interest are compared and the places on the structure corresponding to a minimum for Equations 3.17 and 3.18 are found. Like the five-sided box the resulting positions were slightly different based on the computational method used. The feed points were located along the same line down the center of the object and again only one mesh node apart. For ease of implementation, the feed point closest to the edge was chosen for this design.

While feed point is important, it is ultimately not enough to ensure that the proper mode is excited. The antenna being attached to the existing structure should have current parallel to the existing structure and in the direction of the desired modal current in order to excite the appropriate surface currents

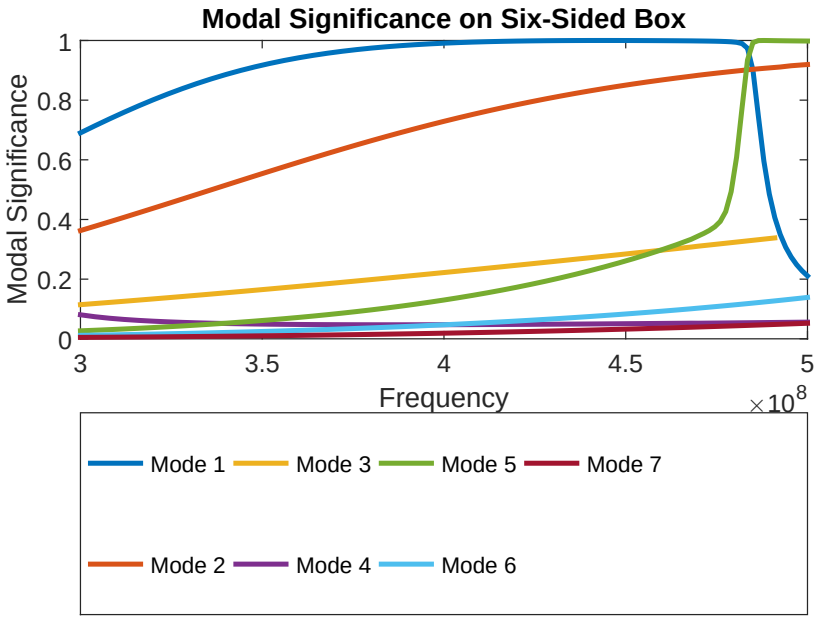

Figure 3.21: Modal significance for first 7 modes on a six-sided box

[52]. Requiring the element to be conformal limits the potential antenna designs. The surface current for each mode is shown in Figure 3.23. The surface current for the third mode is shown more clearly in Figure 3.24. It is important to note that current is spiraling around the outside of the six-sided box. In order to minimally increase the volume occupied by the antenna once installed, the antenna should be kept close to the shell of the box. Because the metal from the excitation will be close to the existing structure, the current on the structure needs to be close to the desired modal current. Simply including a large metal patch on top of the six-sided box, even using the chosen feed-point, will create a pattern that radiates primarily in the z direction. The shape of the additional structure must lend itself to a circulating current similar to the modal current needed on the existing structure.

For that reason a spiral element is chosen. The spiral allows for the circulating current that is required to excite mode 3 and it also allows the antenna to be easily impedance matched on the structure by utilizing a shorting pin. The chosen spiral structure can be seen in Figure 3.25.

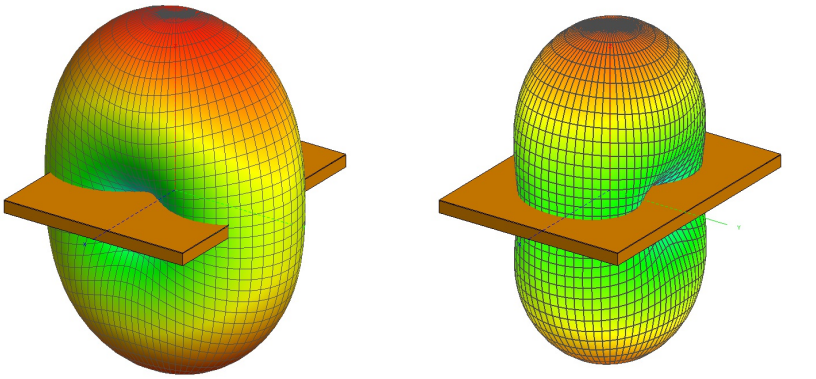

(a) Mode 1

(b) Mode 2

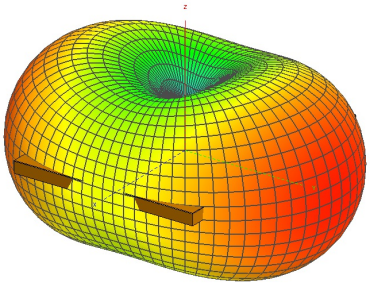

(c) Mode 3

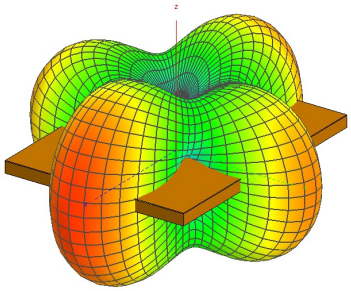

(d) Mode 4

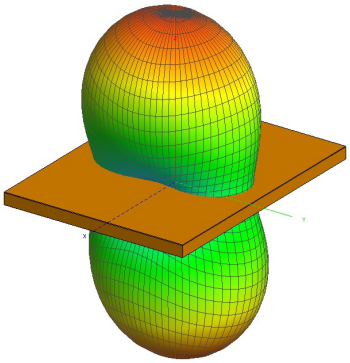

(e) Mode 5

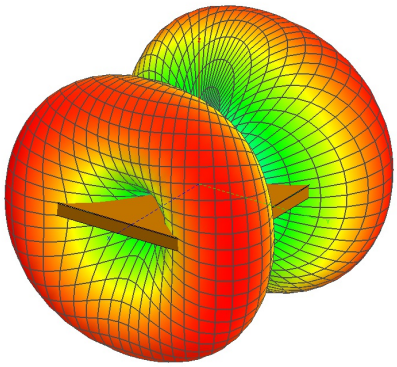

(f) Mode 6

Figure 3.22: Characteristic far-fields corresponding to the modal currents for a five-sided box at 400 MHz

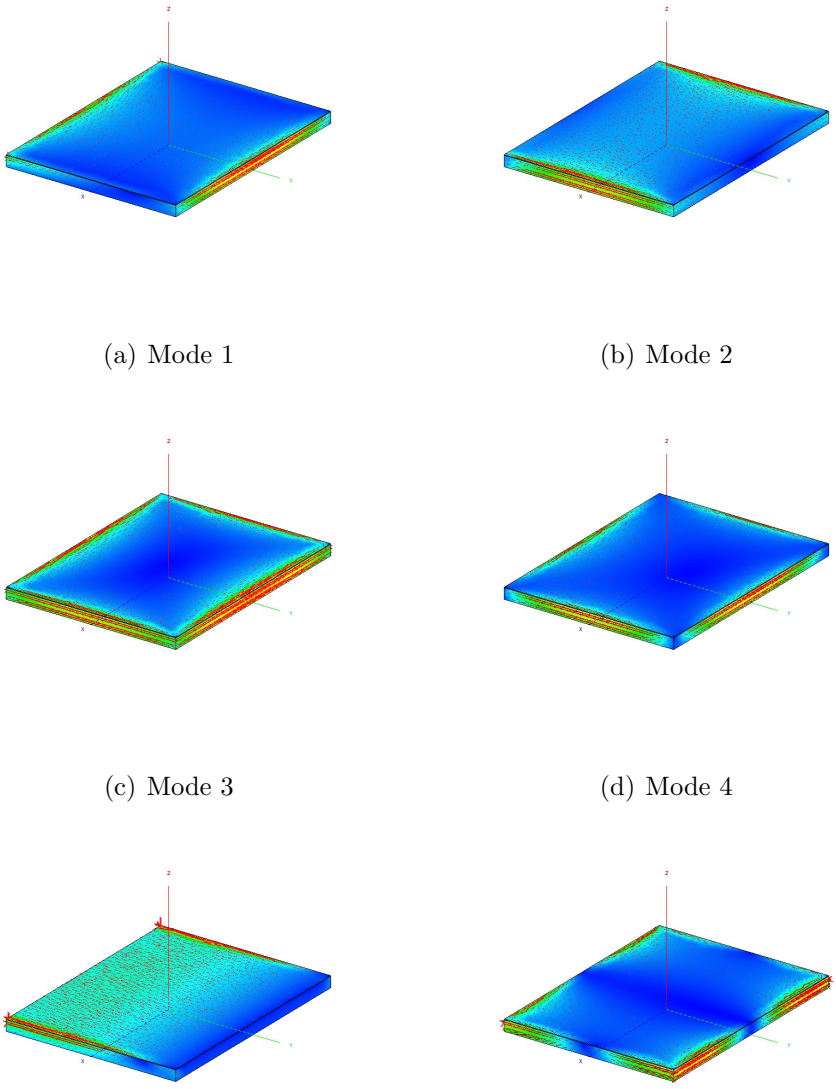

(a) Mode 1

(b) Mode 2

(c) Mode 3

(d) Mode 4

(e) Mode 5

(f) Mode 6

Figure 3.23: Modal surface currents corresponding to the first 6 modes on the six-sided box

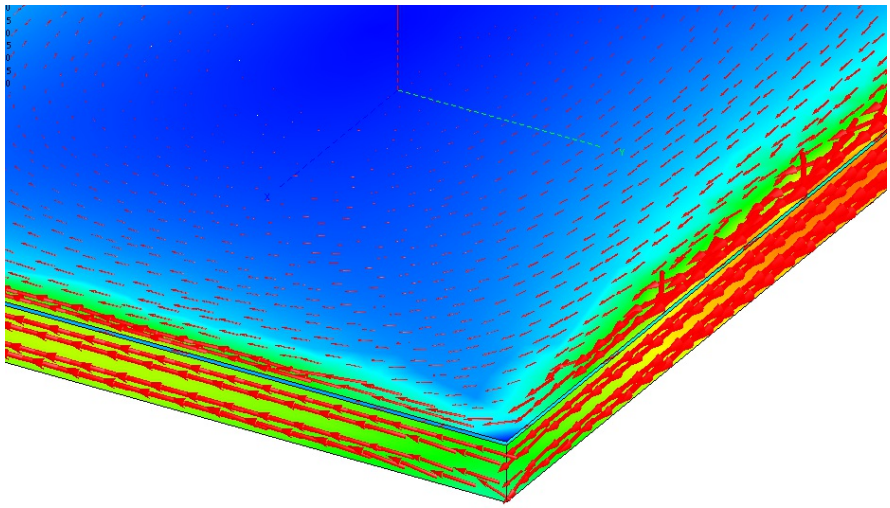

Figure 3.24: Zoomed in on surface current for the third mode on the box

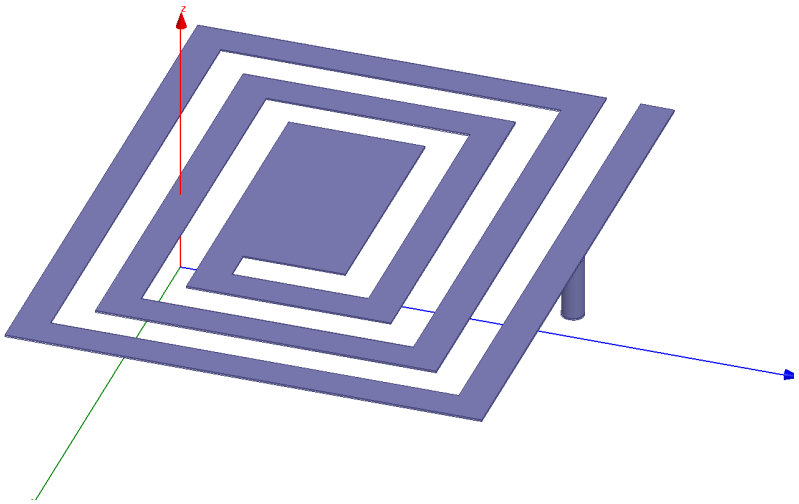

Figure 3.25: Spiral element to be installed on existing structure

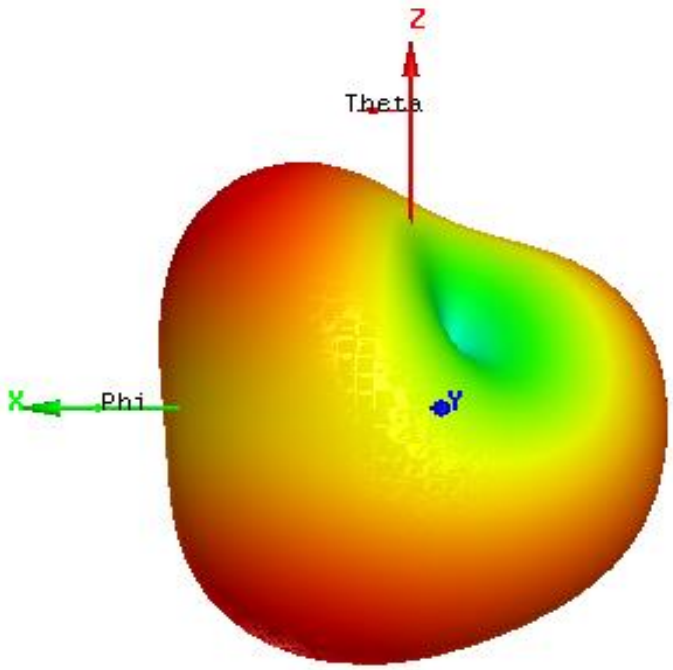

Figure 3.26: Simulated far-field for spiral installed on existing structure

Using the spiral element and the chosen feed point, an antenna was designed in HFSS®. A shorting stub is used to impedance match the structure at 400 MHz. The resulting total radiation pattern is shown in Figure 3.26. The far-field pattern has a null close to the positive z-axis much like the third mode. The resulting pattern also has a nearly omnidirectional pattern in the $x - y$ plane just as in the desired pattern. There is a slightly larger lobe in the resultant pattern that was not included in the original modal pattern. This result is from the combination of the first two modes with the third mode.

The simulated antenna was then built to verify the results. A picture of the antenna is shown in Figure 3.27. Measuring the impedance, the antenna's center frequency shifted to 377 MHz. The small downward shift in the center frequency of the antenna is likely due to the difference in copper thickness

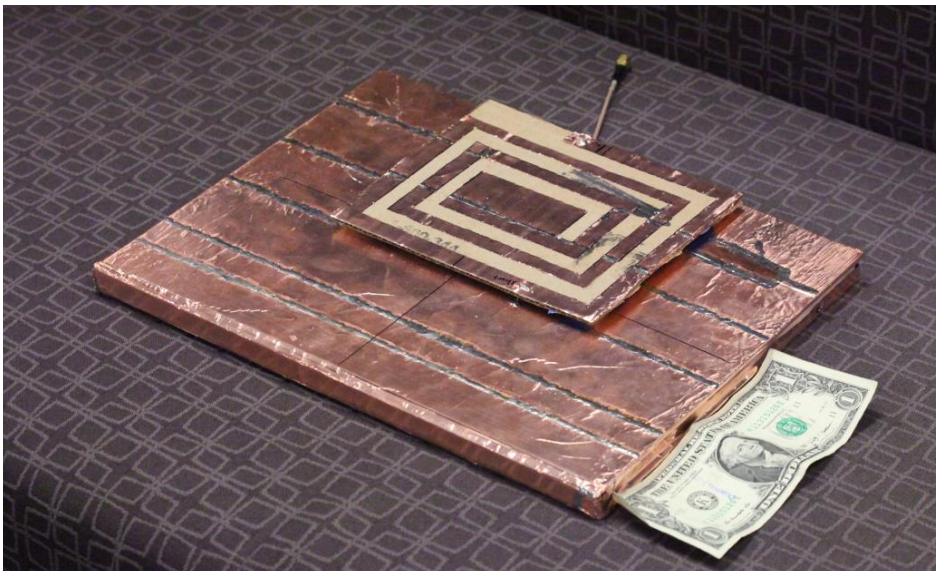

Figure 3.27: Picture of the antenna built to verify simulated results

between the model and the fabricated antenna [53]. There are also slight differences in the dielectric inside the box compared to the air dielectric that was used in simulation.

The far-field pattern was measured and compared to the simulated pattern. The pattern cuts are shown in Figure 3.28. The normalized measured patterns match well with the simulated patterns. The maximum gain on the built antenna was within 1 dB of the simulated value. Because the existing structure is smaller than 1.25λ and an irregular shape, it can be difficult to mitigate cable radiation inside the chamber. Although baluns were used to choke the cable radiation, the cable was still able to radiate and caused some deviation from the simulated patterns. The pattern measurements verify that the pattern is very close to omnidirectional in the $x - y$ plane as designed.

While the far-field pattern is far from purely that of mode 3, the resulting antenna does meet the design goals and approaches the radiation pattern designated by the third mode on the existing structure.

While both calculations for the feed point position are valid, a more rigorous approach to determining the feed point is desired. The methodology that utilizes both current magnitude and direction, neglects the impact of manufacturing differences while the secondary formulation neglects some of the theoretical framework for about orthogonal modes. For that reason the

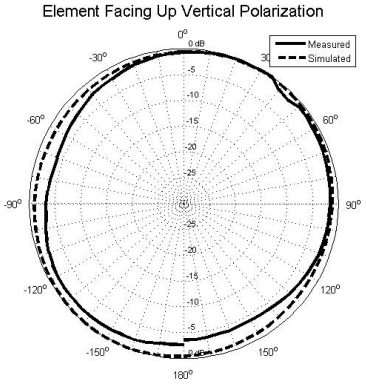

(a) E_θ in XY plane

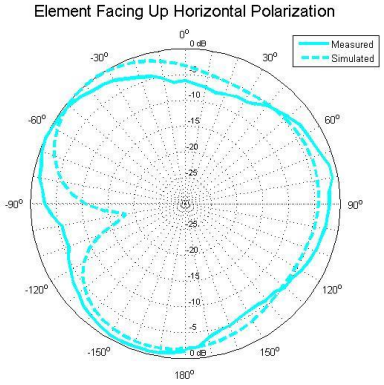

(b) E_ϕ in XY plane

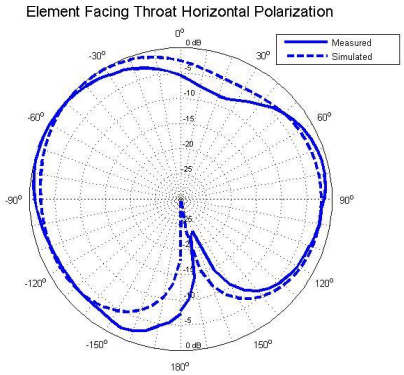

(c) E_θ in XZ plane

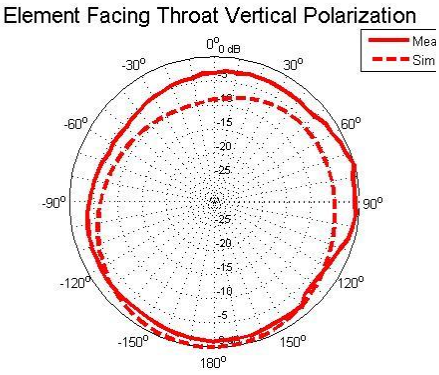

(d) E_ϕ in XZ plane

Figure 3.28: Measured and simulated results in four cut planes for the built antenna

design methodology was revised to mitigate these concerns.

3.4 Design Methodology

This section contains the revised design methodology allowing for the code to accommodate slight manufacturing and simulation differences while also taking into account the orthogonality of eigencurrents on the structure. The goal with this methodology is to provide more insight into an intelligent choice for a single feed point on the structure when the goal is to generate a radiation pattern associated with a higher order mode.

The first step in the process is to perform a characteristic mode analysis on the structure and solve for the characteristic radiation patterns. The designer can then choose which characteristic radiation pattern is desirable for their scenario based on the required power and/or polarization. The goal of this design methodology is to design an antenna whose radiation pattern matches the desired modes as closely as possible. There are many ways to capture which modes are significant. Some use stringent methods where significant modes have a modal significance greater than 0.707 [54]. In this case, a less stringent definition is used. The chosen mode must have a modal significance above 0.1 to ensure the mode will radiate properly and that the desired mode can be excited on the platform. Modes with MS below 0.1 have too much energy storage to excite them appropriately.

The next step is to find the feed point that will best excite the mode of interest. The impedance is not yet considered because an antenna will be connected to the platform that will assist in impedance matching. The feed point will be confined to one point. The goal is to find the mesh shape in the simulation that corresponds to the ideal feed point on the platform for the desired radiation pattern. Method of moments code is used to find the [Z] matrix and solve for the characteristic modes. In the process, the platform must be meshed to appropriately calculate the impedance matrix and solve for the characteristic modes. Ideally we would use this mesh as a baseline to establish the best feed position for the mode of interest. Unfortunately, feeds take up physical space and there are differences between simulated and constructed geometries. Often the size of the mesh shapes are small compared to these features. The methodology thus looks for the group of coupled mesh

shapes that provides the most favorable conditions for the feed position. The mesh shapes that are most closely coupled are grouped together and referred to as the neighborhood of a mesh shape of interest. This allows for the method to consider the currents in the area surrounding the mesh shape to choose the ideal group of shapes for feed placement.

The neighborhood of a mesh shape can be defined using the impedance matrix. The goal is to have the neighborhood consist of the other mesh elements that are most closely coupled to the chosen mesh shape. Mutual coupling plays a large role in antenna performance and can often be described using an impedance matrix [18, 21, 22, 23, 55]. Equations 3.1 and 3.2 demonstrate that the impedance matrix is used when solving for the characteristic modes. The impedance matrix can be reused to solve for the neighborhood of a mesh shape. The boundary of the original mesh shape is defined by several edges. The coupling between one edge and any others can be seen by using the row or column of the [Z] matrix corresponding to the specified edge. The edges that do not define the original mesh shape can then be ranked from the strongest coupling to weakest coupling for each edge of the original mesh shape. The edges that have a coupling value greater than a specified amount of the self-coupling between the edge and itself denote the edges contained within the neighborhood region about the original mesh shape. The specified amount should be chosen as a compromise between the size of the neighborhood created and the size of the platform. This will be dependent on the size of the mesh chosen by the designer. For the example later, the edges of the neighborhood of the original mesh shape have a coupling value greater than 10% of the self-coupling for the edges.

Once the neighborhood of each mesh shape has been defined, the definition can be used to designate the feed point region. For ease of notation, the mode corresponding to the desired radiation pattern is mode i and the corresponding modal current is J_i. The feed point region will be chosen as the neighborhood of a mesh shape that has the average maximum modal current for the mode of interest compared to all other radiating modes. In order to find this region, $a(r)$ is calculated for each mesh shape using Equation 3.19.

$$a(r) = \sum_{m}^{m \neq i} J_m(r) \cdot J_i(r) - |J_i(r)|^2. \tag{3.19}$$

The neighborhood about each mesh shape is then defined using the method described previously. Once the neighborhoods are defined, an average $a(r)$ can be calculated for the neighborhood about each mesh shape. The goal is to then find the neighborhood where the averaged $a(r)$ is a minimum and the original mesh shape for that neighborhood has current flowing through it. All regions based around mesh shapes where $|J_i(r)|^2$ is less than the median value are discarded to ensure current is flowing through all remaining neighborhoods. The feed region is then chosen as the region where the average $a(r)$ is minimized and $|J_i(r)|^2$ for the mesh shape at the center of the region is greater than the median $|J_i(r)|^2$.

Even after choosing the feed placement, the antenna element that will be attached to the feed point needs to be designed. The installed antenna element must be used to enforce the desired current flow on the platform much like in the previous methods described in this chapter. For conformal antenna elements, the element should follow the path of the modal current for the desired mode near the feed point. For example, if the currents run horizontally along the top of the structure, the antenna should follow the current lines. The length of the antenna should be changed to ensure the antenna is properly matched and the proper current has been induced onto the platform. The next section describes an example of how to use this methodology when designing an antenna for a rectangular platform.

3.5 Example

To show how this method is utilized, an element will be designed to similar specifications as the previous example in this chapter. The goal is to design an antenna with a VSWR better than 3:1 at 400 MHz that is installed on a box that measures 32cm x 24.5cm x 1.5cm (0.427λ x 0.327λ x 0.02λ) as seen in Figure 3.19. The scenario requires that the object has a null in the z-direction and an omnidirectional radiation pattern in the $x-y$ plane. In this case the antenna cannot extend significantly from the platform in any particular dimension. Based on the method described in the previous sections, the first step is to perform a characteristic mode analysis on the platform.

The characteristic mode analysis is the same as in Section 3.3. The char-

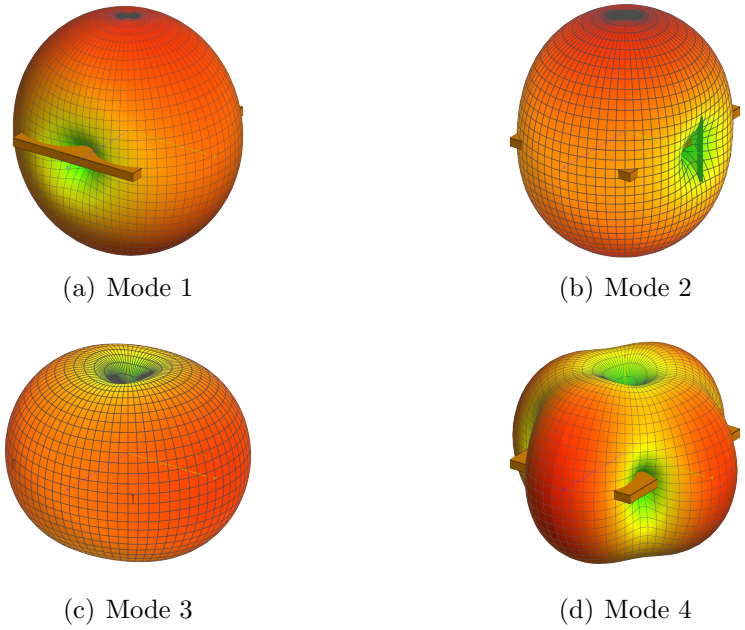

(a) Mode 1

(b) Mode 2

(c) Mode 3

(d) Mode 4

Figure 3.29: The characteristic far-fields associated with the first four modes on the box

acteristic mode analysis reveals that there are several modes with a modal significance above 0.1 at the frequency of interest (400 MHz). Refer to Figure 3.21 for a plot of the modal significance of the different modes on the structure. Figure 3.29 shows the radiation patterns corresponding to the first four modes. These are the same as the first four modes found in Figure 3.22. Because the goal is to have as little radiation as possible in the $+z-$direction, the patterns corresponding to modes 1 and 2 are not appropriate for this example. Mode 4 has nulls in the $x-y$ plane which are also undesirable according to the original scenario. Mode 3 shows a loop mode has been excited on the structure that generates a pattern that best suits the stated design goal.

Now that the desired far-field mode has been identified, the next step is to determine the appropriate feed position. This is where the new methodology can be implemented and this section differs significantly from Section 3.3. In the process of computing the characteristic modes, we had to solve for the [Z]-matrix corresponding to the platform. Using the developed methodology, neighborhoods were identified on the structure based on the strength of coupling between mesh elements on the platform. For this particular platform Figure 3.30 identifies the region where the feed should be placed. Because

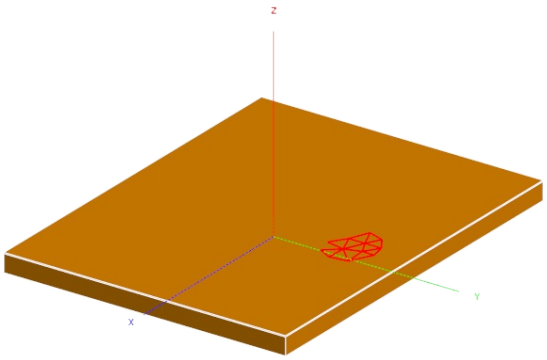

Figure 3.30: Mesh triangles corresponding to the neighborhood of the feed point are highlighted on the existing structure

the box and the mesh are symmetric about the y-axis, the feed placement region has a counterpart about the y-axis; however, for the purposes of this example we will use the region with the feed in the $-x$ portion of the top-side of the box.

The next step is to determine what the antenna that couples into the platform should look like. To excite the platform such that the radiation pattern for mode 3 is generated, the goal is to excite currents on the structure that resemble the corresponding characteristic surface current. Figure 3.31 shows what the current must look like on the platform to excite the needed radiation pattern. The circulating current flows along the outermost edges of the platform with little to no current flowing near the center of the platform.

The developed antenna needs to be conformal in order to ensure the path along the added antenna will excite currents on the platform. Because the desired currents on the platform are flowing around the outside of the platform, the antenna must also have an element that enforces the circulating current. In order to create the desired circulating currents, a meander is added on the top side of the box near the outer edge.

The designed antenna element is shown in Figure 3.32. The resulting radiation pattern is shown in Figure 3.33. The radiation pattern has a null in the $+z$-direction and is omnidirectional in the $x - y$ plane, as desired. VSWR was also simulated and is shown in Figure 3.34. The methodology allowed for the design of a conformal, single feed antenna that is matched at 400 MHz and has the desired radiation pattern.

The assumption in this section has been that the desired mode is found

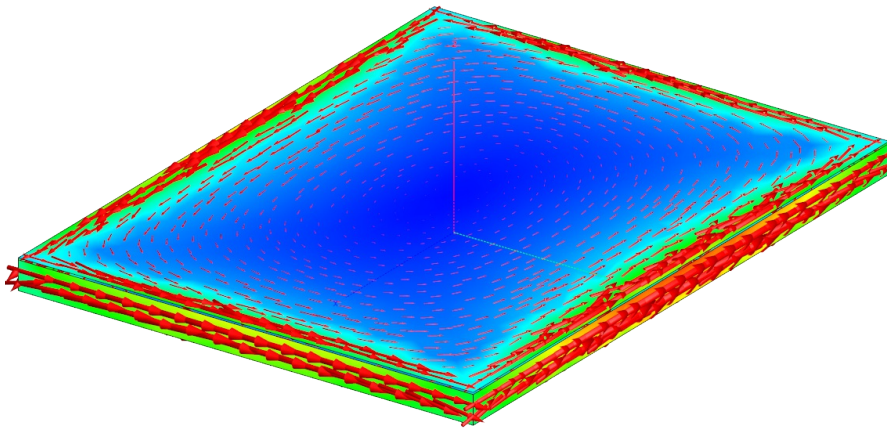

Figure 3.31: Surface current corresponding to mode 3

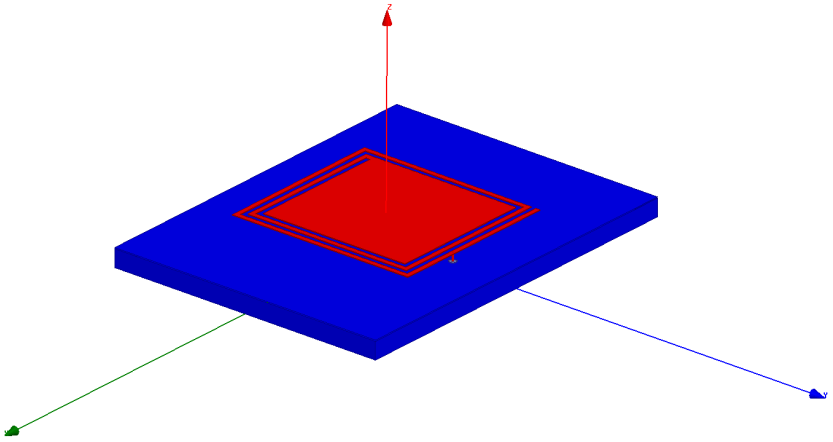

Figure 3.32: Antenna installed on the platform to create desired radiation pattern

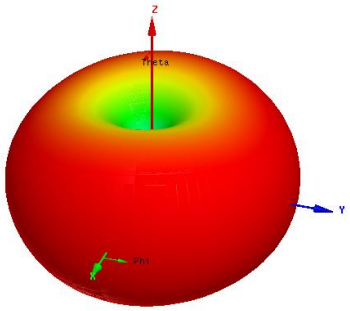

Figure 3.33: Simulated radiation pattern associated with designed antenna

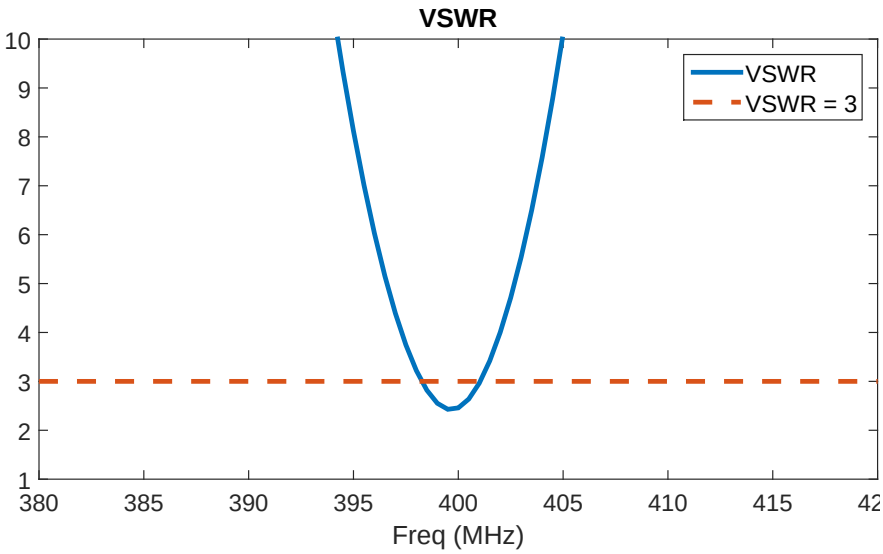

Figure 3.34: VSWR for designed antenna

within the set of characteristic far-fields that have modal significance values above 0.1. This may not always be the case. It is possible to combine modes in order to create different radiation patterns. Because the overall design of the antenna will be limited by the existing structure, it is important to examine which antenna radiation patterns are possible given the existing structure. Because the existing structure is often large compared to the space allotted to the antenna element, it is important to excite the existing structure, if possible, in order to improve the gain, bandwidth, or a variety of other performance metrics. The next chapter explores what radiation patterns are achievable given an existing structure.

CHAPTER 4

PATTERN SYNTHESIS

Often the desired radiation pattern does not align exactly with one of the characteristic far-fields on the existing structure. Because of the geometry of the existing structure, not all radiation patterns may be achievable; however, it is important to be able to solve for the modal weighting coefficients that result in a radiation pattern that best approximates the goal pattern. In order to better understand how to compute the modal weighting coefficients and to see if other pattern synthesis methods would be better suited for this problem, the first section evaluates previous research on pattern synthesis.

4.1 Background

Antenna researchers have long been attempting to understand how to generate arbitrary radiation patterns. The earliest studies examined creating arbitrary radiation patterns from finite size sources. One of the most cited early works considers more specifically just at line sources of arbitrary length [56]. The goal is to find aperture-limited functions that will best approximate the specified radiation pattern. The authors use prolate spheroidal functions as their basis because they are the eigenfunctions of the finite Fourier transform in order to ensure the aperture distribution is realizable given the slight differences between simulated and built antennas. Being constrained to a line source, the authors create the distribution by exciting the line with different signals. Later researchers extended the work to include aperture distributions for circular apertures in an infinite perfectly conducting ground plane [57].

Because antenna designers are often given little control over signal input to the antenna, this signal cannot be used to optimize the antenna pattern. The use of the prolate spheroidal wave functions also becomes more difficult

as object geometries become more complex. Other methods were developed in order to simplify the optimization process, especially when the sources were lines or uniformly spaced arrays. One such method was the iterative sampling method where the designer starts with a design and then adds progressively more correction patterns to attempt to better approximate the desired pattern [58]. Many different aperture distributions can approach a similar radiation pattern with a variety of different trade-offs. Unfortunately, many of those distributions may have high stored energies or be difficult to realize. It is also possible that for some geometries, no acceptable solution can be found that is both realizable and close to the desired pattern [59].

In order to constrain the space to radiation patterns that are realizable, later researchers applied characteristic mode theory to pattern synthesis problems [60]. The authors assume that all the modes have the same phase on their modal weighting coefficient and then proceed to use the minimum mean-square error to solve for the modal weighting coefficients that correspond to the desired pattern. This result is limited to cases where the modal weighting coefficients have the same phase across modes, which is not always true. This assumption is made as the reference was using real current at port voltages versus the sum of modal surface currents. The previous method also requires knowledge of both the desired pattern and polarization in any particular direction. The complete specification of the radiation pattern may not be necessary or desired for some applications. The theory was further extended to N-port scatterers, focusing on iterative methods for approaching the appropriate solution [61, 62]. The functional implementation using characteristic modes does ensure that the resulting pattern is physically realizable; however, it also may result in solutions that are farther from the desired radiation pattern. The implementations using characteristic modes also require that the modal currents be real such that the modal weighting coefficients all have the same phase across modal index. For many applications this many not be a realistic condition that can be met.

Treatments for power patterns were developed but are still very much iterative. They also involve solving for the phase of the desired pattern as part of the development. The iterative methods reach local solutions that are not able to find minimums over all possible values [63, 61, 62]. Eventually the goal of pattern synthesis research became to determine the shape of the structure needed to excite desired radiation pattern [64]. The

author focuses on rotationally symmetric patterns to simplify the synthesis but also discussed issues with feeding arrangements to excite desired modes on the structure. Later work shows that this method does not extend to end-fire radiation patterns, making it difficult to do shape synthesis for certain pattern types [65].

Other modal structures besides characteristic modes were also used to do pattern synthesis. Spherical Bessel functions and weighted Inagaki modes were also chosen as possibilities for pattern synthesis [66, 67]. While spherical Bessel functions can be useful for spherical antenna shapes and transforming to free space, they become more difficult to use for arbitrary antenna shapes. Inagaki modes are more general than characteristic modes but can be used very similarly to characteristic modes for pattern synthesis. There have also been several articles attempting to create a general formulation for the synthesis problem [68]. These articles designate an appropriate design within a specified subset of antenna types. While the approach is general, it still requires specific knowledge about each antenna type for the approach to be applied, making it difficult to implement.

Based on the existing research, the original research using line sources is difficult to implement because of the arbitrary existing structures. Because the existing structure may not be a canonical shape, it is important to choose a pattern synthesis method that works for arbitrary structures. The characteristic mode interpretations allow for use on arbitrary structures and utilize the modes that are most likely to radiate. There is a limit to how many modes should be included based on the associated eigenvalue. While higher eigenvalue modes may allow for closer approximations to the desired pattern, they may also be more difficult to solve for and implement. The characteristic mode interpretation is based on the geometry of the structure and orthogonality of the characteristic far-fields at radiation sphere, making the modal structure well-suited for pattern synthesis. Lastly, characteristic mode theory is widely used so commercial solvers have the ability to evaluate the characteristic modes on arbitrary structures. The next section in this chapter focuses on the scenario where both the power and polarization are specified. The final section considers the case where only the power is specified and aims to understand how to approximate the modal weighting coefficients in that scenario.

4.2 Pattern Synthesis Specifying Power and Polarization

Harrington and Mautz developed a method for calculating modal weighting coefficients based on a desired power and polarization; however, it requires equiphase modal weighting coefficients [60]. The modal weighting coefficients are not always equiphase so a new method must be developed that can solve for complex modal weighting coefficients. The first subsection will describe the method developed by Harrington and Mautz and then the next subsections will show how I adapted the method to solve for non-equiphase modal weighting coefficients and characteristic far-fields.

4.2.1 Harrington and Mautz Pattern Synthesis Method

The literature assumes an equiphase current J that approximates the goal radiation pattern F [60]. The modal weighting coefficients for each modal weight, α_n, are assumed to be equiphase and can be represented by

$$\alpha_n = e^{j\beta}\gamma_n. \tag{4.1}$$

J is assumed to be a superposition of N modal currents where

$$J = e^{j\beta}\sum_{n=1}^{N}\gamma_n J_n. \tag{4.2}$$

Based on characteristic mode theory, the corresponding radiation field is

$$E = e^{j\beta}\sum_{n=1}^{N}\gamma_n E_n \tag{4.3}$$

where E_n are the characteristic far fields. The goal pattern, F, is then specified at M points on the radiation sphere. If $M > N/2$ then there are more equations than unknowns. The equations can then be evaluated to solve for the modal weighting coefficients that result in the minimum mean-square

error. The equation that describes the error is given by

$$\epsilon = \sum_{m=1}^{M} |e^{j\beta} \sum_{n=1}^{N} \alpha_n E_n^m - F^m|^2 \tag{4.4}$$

where the m subscript denotes the mth point on the radiation sphere. This can be simplified using matrix notation as

$$\epsilon = [e^{j\beta} A\gamma - F]^{*T} [e^{j\beta} A\gamma - F] \tag{4.5}$$

where $[\gamma]$ is a column vector of the modal weighting coefficients, $[F]$ is a column vector of the goal electric field corresponding to the radiation pattern, and $[A]$ is a matrix such that

$$A_{mn} = E_n^m. \tag{4.6}$$

The next step is to evaluate the variation in the error, ϵ, when $[\alpha]$ is varied. The variation in this case is described by

$$\delta\epsilon = 2[\delta\alpha]^T [Re(A^{*T} A)\alpha - Re(e^{-j\beta} A^{*T} F)]. \tag{4.7}$$

For $\delta\epsilon$ to be zero for arbitrary $[\delta\alpha]$, then

$$[\alpha] = [Re(A^{*T} A)]^{-1} [Re(e^{-j\beta} A^{*T} F)]. \tag{4.8}$$

The error is then given by

$$\epsilon = -Re[e^{-j\beta} A^{*T} F] + [F]^{*T} [F]. \tag{4.9}$$

For a fixed phase β, then the modal weighting coefficients are determined by 4.8. However, β can still be adjusted to further minimize ϵ. The next step is to take the derivative of 4.9 with respect to β and set it to 0.

$$\beta = \frac{1}{2} \tan^{-1} \frac{c_3}{c_1 - c_2} \tag{4.10}$$

where

$$c_1 = -[Re(A^{*T} F)]^T [Re(A^{*T} A]^{-1} Re[A^{*T} F] \tag{4.11}$$

$$c_2 = -[Im(A^{*T} F)]^T [Re(A^{*T} A]^{-1} Im[A^{*T} F] \tag{4.12}$$

$$c_3 = -2[Im(A^{*T}F)]^T[Re(A^{*T}A]^{-1}Re[A^{*T}F]. \tag{4.13}$$

Solving Equation 4.10 results in two solutions. One of the solutions for β will have a significantly lower ϵ compared to the other and thus is the β to use.

As described before, this technique requires equiphase currents. When the modal currents are not equiphase it is important to realize that the characteristic far fields are not necessarily real and neither are the modal weighting coefficients. A new method must be developed to solve for the modal weighting coefficients when the characteristic far-fields and therefore the modal weighting coefficients are complex.

4.2.2 Developed Pattern Synthesis Method with no ϕ or θ Variation

The simplest case occurs when the existing structure and the radiation pattern have no ϕ variation or no θ variation. When the structure lacks ϕ or θ variation, the resulting far-field will also lack the same variation, making it difficult for the structure to meet a goal pattern with variation. Using a similar derivation to Harrington and Mautz, the desired radiation pattern is specified at M points along the radiation sphere. Again the matrix A is formed where the components for the matrix are defined as

$$A_{mn} = E_n^m \tag{4.14}$$

where the mth row and the nth column of A is occupied by the value of the characteristic far-field of the nth mode at the mth point along the radiation sphere. $[\alpha]$ is defined as a column matrix where the nth element is the modal weighting coefficient for the nth mode. The total characteristic field of the resulting structure can then be written as

$$E = A[\alpha] \tag{4.15}$$

where E is a column matrix and the mth element corresponds to the value of the field at point m on the radiation sphere. F is a column vector with the mth element being the desired field at the mth point on the radiation

sphere. Therefore the error in the far-field can be defined according to

$$\epsilon = [A[\alpha] - F]^{*T}[A[\alpha] - F]. \tag{4.16}$$

If α is varied slightly by $\delta\alpha$, then the error, ϵ, will be varied by $\delta\epsilon$.

$$\epsilon + \delta\epsilon = [A[\alpha + \delta\alpha] - F]^{*T}[A[\alpha + \delta\alpha] - F] \tag{4.17}$$

$$\begin{aligned}\epsilon + \delta\epsilon =& [\alpha]^{*T}A^{*T}A[\alpha] + [\alpha]^{*T}A^{*T}A[\delta\alpha] - [\alpha]^{*T}A^{*T}F \\ &+ [\delta\alpha]^{*T}A^{*T}A[\alpha] + [\delta\alpha]^{*T}A^{*T}A[\delta\alpha] - [\delta\alpha]^{*T}A^{*T}F \\ &- F^{*T}A[\alpha] - F^{*T}A[\delta\alpha] + F^{*T}F\end{aligned} \tag{4.18}$$

$$\begin{aligned}\delta\epsilon =& [\alpha]^{*T}A^{*T}A[\delta\alpha] + [\delta\alpha]^{*T}A^{*T}A[\alpha] - [\delta\alpha]^{*T}A^{*T}F \\ &- F^{*T}A[\delta\alpha] + [\delta\alpha]^{*T}A^{*T}A[\delta\alpha]\end{aligned} \tag{4.19}$$

$$\begin{aligned}\delta\epsilon =& [\delta\alpha]^{*T}A^{*T}A[\delta\alpha] + [\delta\alpha]^{*T}A^{*T}A[\alpha] + ([\delta\alpha]^{*T}A^{*T}A[\alpha])^{*T} \\ &- [\delta\alpha]^{*T}A^{*T}F - ([\delta\alpha]^{*T}A^{*T}F)^{*T}\end{aligned} \tag{4.20}$$

$$\delta\epsilon = [\delta\alpha]^{*T}A^{*T}A[\delta\alpha] + 2Re([\delta\alpha]^{*T}A^{*T}A[\alpha]) - 2Re([\delta\alpha]^{*T}A^{*T}F). \tag{4.21}$$

The next step is to minimize $\delta\epsilon$. Because $\delta\alpha$ is arbitrary, the minimum is obtained by minimizing $2Re([\delta\alpha]^{*T}A^{*T}A[\alpha]) - 2Re([\delta\alpha]^{*T}A^{*T}F)$. Because $[\delta\alpha]$ is complex and arbitrary, Equation 4.30 must be satisfied regardless of the choice of $[\delta\alpha]$. Thus because $[\delta\alpha]$ is arbitrary and could be complex, then

$$A^{*T}A[\alpha] = A^{*T}F. \tag{4.22}$$

Solving for α gives

$$[\alpha] = \frac{A^{*T}F}{(A^{*T}A)^{-1}} \tag{4.23}$$

To use this with a practical example, a dipole 5cm in length ($\lambda/2$ at 3GHz) was simulated in FEKO®. The first 12 characteristic modes were found. The

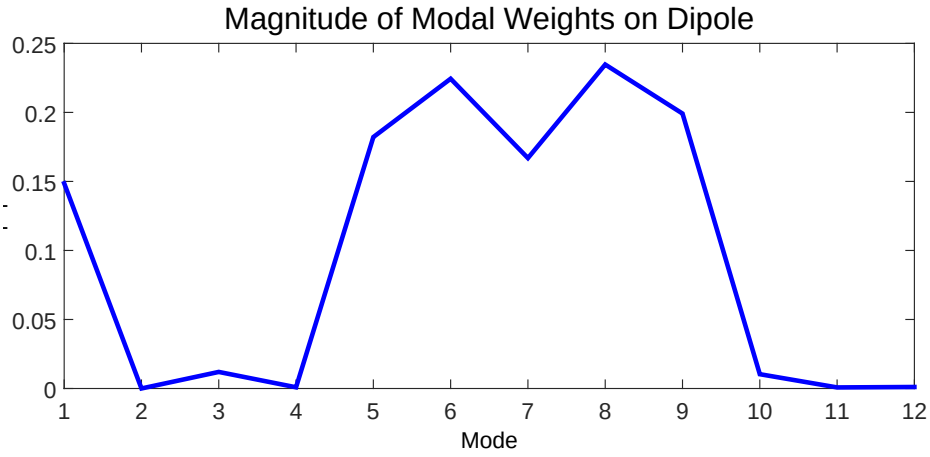

Figure 4.1: Magnitude of modal weighting coefficients from antenna synthesis procedure

desired far-field was chosen to be 4.24.

$$f(\theta, \phi) = \cos\theta. \tag{4.24}$$

Using the characteristic far-fields and the desired pattern, $[\alpha]$ is determined using Equation 4.23. The magnitude for the resulting modal weighting coefficients are shown in Figure 4.1.

Theoretically a resonant dipole has a far-field specified as

$$F_\theta = \frac{\cos((\pi/2)\cos(\theta)}{\sin(\theta)}. \tag{4.25}$$

Because the goal pattern is slightly different from the traditional far field, the higher order modes have significant modal weighting coefficient magnitudes.

The error is then evaluated at each point on the sphere. A plot of the error is found in Figure 4.2. The average error over all the points is $1.22 * 10^{-9}$. The program does a good job of using a finite number of modes to closely mirror the goal pattern on the antenna. The far-field pattern and the goal pattern, when plotted together, cannot be distinguished from one another as shown in Figure 4.3. The error is very small because the goal pattern is achievable using the dipole structure. If the goal pattern could only be

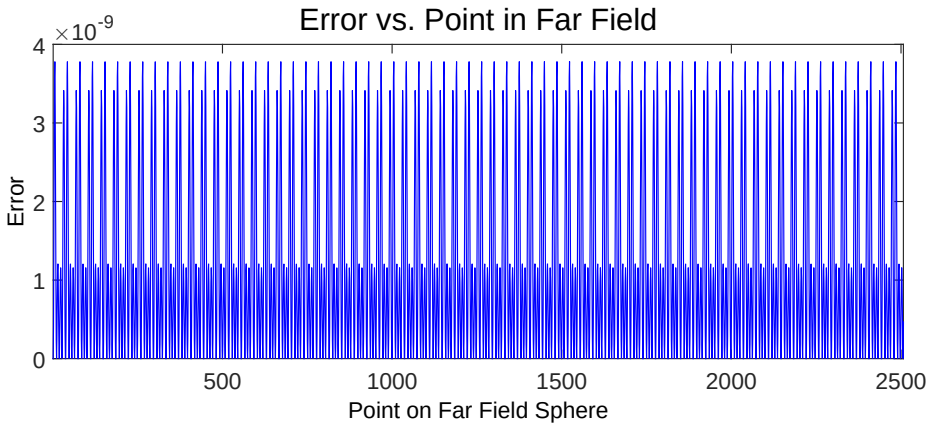

Figure 4.2: Error at each point in the far field

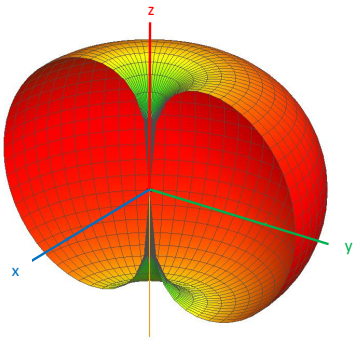

Figure 4.3: Goal and the resulting total far-field patterns

approximated by the existing structure, the error would grow substantially.

4.2.3 Pattern Synthesis with ϕ and θ Variation

This section extends the scenario to when the goal pattern has both θ and ϕ variation. It calculates modal weighting coefficients when the modes are not equiphase and the goal pattern, F, will be specified independently for the θ and ϕ components of the electric field at M points on the radiation sphere. Now the modal weighting coefficients can be represented by a complex column vector, $[\alpha]$. Using the same matrix notation, the error between the goal

pattern and the achieved pattern can be written as

$$\epsilon = [A_\theta[\alpha] - F_\theta]^{*T}[A_\theta[\alpha] - F_\theta] + [A_\phi[\alpha] - F_\phi]^{*T}[A_\phi[\alpha] - F_\phi]. \tag{4.26}$$

The minimum mean-square error now examines the total error for both polarizations. To solve for $[\alpha]$, $[\alpha]$ is varied by a small $[\delta\alpha]$. This results in

$$\begin{aligned}
\epsilon + \delta\epsilon =& [\alpha]^{*T} A_\theta^{*T} A_\theta[\alpha] + [\alpha]^{*T} A_\theta^{*T} A_\theta[\delta\alpha] - [\alpha]^{*T} A_\theta^{*T} F_\theta \\
&+ [\delta\alpha]^{*T} A_\theta^{*T} A_\theta[\alpha] + [\delta\alpha]^{*T} A_\theta^{*T} A_\theta[\delta\alpha] - [\delta\alpha]^{*T} A_\theta^{*T} F_\theta \\
&- F_\theta^{*T} A_\theta[\alpha] - F_\theta^{*T} A_\theta[\delta\alpha] + F_\theta^{*T} F_\theta \\
&+ [\alpha]^{*T} A_\phi^{*T} A_\phi[\alpha] + [\alpha]^{*T} A_\phi^{*T} A_\phi[\delta\alpha] - [\alpha]^{*T} A_\phi^{*T} F_\phi \\
&+ [\delta\alpha]^{*T} A_\phi^{*T} A_\phi[\alpha] + [\delta\alpha]^{*T} A_\phi^{*T} A_\phi[\delta\alpha] - [\delta\alpha]^{*T} A_\phi^{*T} F_\phi \\
&- F_\phi^{*T} A_\phi[\alpha] - F_\phi^{*T} A_\phi[\delta\alpha] + F_\phi^{*T} F_\phi.
\end{aligned} \tag{4.27}$$

Solving for the small change in error, $\delta\epsilon$,

$$\begin{aligned}
\delta\epsilon =& [\alpha]^{*T} A_\theta^{*T} A_\theta[\delta\alpha] + [\delta\alpha]^{*T} A_\theta^{*T} A_\theta[\alpha] \\
&+ [\delta\alpha]^{*T} A_\theta^{*T} A_\theta[\delta\alpha] - [\delta\alpha]^{*T} A_\theta^{*T} F_\theta \\
&- F_\theta^{*T} A_\theta[\delta\alpha] + [\alpha]^{*T} A_\phi^{*T} A_\phi[\delta\alpha] \\
&+ [\delta\alpha]^{*T} A_\phi^{*T} A_\phi[\alpha] + [\delta\alpha]^{*T} A_\phi^{*T} A_\phi[\delta\alpha] \\
&- [\delta\alpha]^{*T} A_\phi^{*T} F_\phi - F_\phi^{*T} A_\phi[\delta\alpha]
\end{aligned} \tag{4.28}$$

remains. This can be simplified to

$$\begin{aligned}
\delta\epsilon =& [\delta\alpha]^{*T} A_\theta^{*T} A_\theta[\delta\alpha] + [\delta\alpha]^{*T} A_\phi^{*T} A_\phi[\delta\alpha] \\
&+ 2Re([\delta\alpha]^{*T} A_\theta^{*T} A_\theta[\alpha]) + 2Re([\delta\alpha]^{*T} A_\phi^{*T} A_\phi[\alpha]) \\
&- 2Re([\delta\alpha]^{*T} A_\theta^{*T} F_\theta) - 2Re([\delta\alpha]^{*T} A_\phi^{*T} F_\phi).
\end{aligned} \tag{4.29}$$

To minimize the error, Equation 4.29 must be minimized. The first two terms are both depend heavily on $[\delta\alpha]$. Because $[\delta\alpha]$ is small and arbitrarily chosen, these two terms cannot be minimized. The focus must then be to minimize the remaining four terms for an arbitrary complex $[\delta\alpha]$. Minimizing

Table 4.1: Resulting modal weighting coefficients when goal pattern is a linear combination of modes

Mode	Coefficients
1	0.5+j
2	0.5
3	0.2+0.2j
4, 5, 6	$< 10^{-16}$

the remaining four terms leads to

$$Re([\delta\alpha]^{*T} A_\theta^{*T} A_\theta[\alpha]) + Re([\delta\alpha]^{*T} A_\phi^{*T} A_\phi[\alpha]) = Re([\delta\alpha]^{*T} A_\theta^{*T} F_\theta) + Re([\delta\alpha]^{*T} A_\phi^{*T} F_\phi). \quad (4.30)$$

Because $[\delta\alpha]$ is complex and arbitrary, Equation 4.30 must be satisfied regardless of the choice of $[\delta\alpha]$. One such solution is when

$$(A_\theta^{*T} A_\theta + A_\phi^{*T} A_\phi)[\alpha] = A_\theta^{*T} F_\theta + A_\phi^{*T} F_\phi. \quad (4.31)$$

Solving this equation for the modal weighting coefficients yields

$$[\alpha] = \frac{A_\theta^{*T} F_\theta + A_\phi^{*T} F_\phi}{(A_\theta^{*T} A_\theta + A_\phi^{*T} A_\phi)^{-1}}. \quad (4.32)$$

This result allows for the calculation of the modal weighting coefficients that create a characteristic far-field that best approximates the specified goal pattern.

To test this, a square plate with a side length of $\frac{\lambda}{2}$ at 3 GHz was modeled and the goal pattern was chosen to be a simple linear combination of modal far fields. The first six modes on the structure were found along with the associated characteristic far-fields. The goal function was chosen to be a linear combination of the first three modes. Equation 4.33 shows the values chosen to weight the modes.

$$F_{goal} = (0.5 + j)E_1 + 0.5E_2 + (0.2 + 0.2j)E_3 \quad (4.33)$$

Solving for the modal weighting coefficients using the method developed yields the coefficients found in Table 4.1.

A plot of the error at each point m on the radiation sphere is shown in

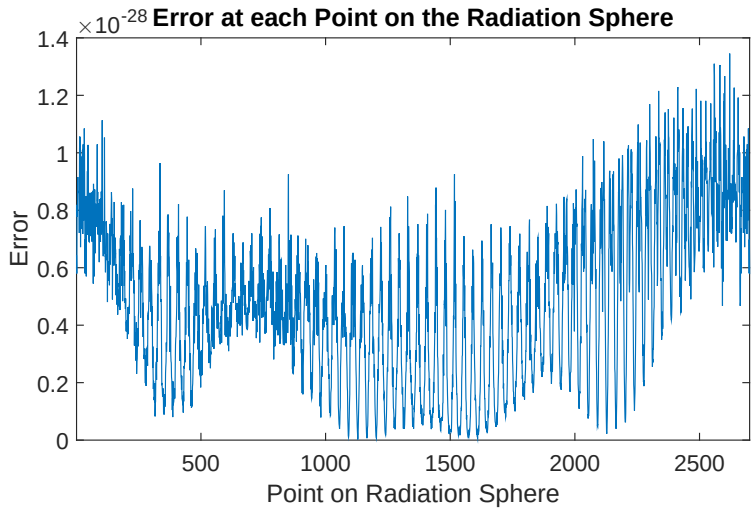

Figure 4.4: Error at each point using a linear combination of characteristic fields as the goal pattern

Figure 4.4. This plot shows the squared difference between the desired electric field and the electric field resulting from the modal weighting coefficients. The mean error at each point is $4.9 * 10^{-29}$ which is within the computational error of the computational software used. The goal pattern and the resulting far-field pattern are shown in Figure 4.5.

For the next test, the goal function was again specified as a linear combination of modes, but this time noise was added. The noise was added separately to the real and imaginary parts of the goal pattern's $\hat{\theta}$ and $\hat{\phi}$ components. The noise is uniformly distributed between 1 and -1. With this goal function, the resulting modal weighting coefficients are found in Table 4.2. While there are some slight deviations for the modal weighting coefficients that were input, these are easily attributed to the added noise. The resulting error at each point on the sphere is shown in Figure 4.6. The average value of the noise is 1.3479. The average error is also equal to the expected value of the magnitude of the sum of two random variables uniformly distributed between -1 and 1. The standard deviation of the error is 0.58 which is equal to the standard deviation of a random variable that is uniformly distributed between -1 and 1. The goal pattern is shown in Figure 4.7 and the resulting pattern is shown in Figure 4.8.

The plate was then used with a different goal function. The goal function was defined with F_θ and F_ϕ equal to one to specify an isotropic power pattern. This pattern is not physically realizable, but the developed method solves for

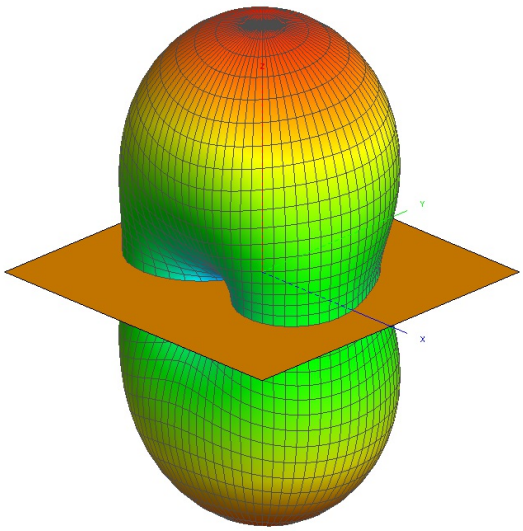

Figure 4.5: Goal and resulting radiation pattern

Table 4.2: Resulting modal weighting coefficients when goal pattern is a linear combination of modes plus noise

Mode	Coefficients
1	0.526+1.002j
2	0.4985+0.0006j
3	0.2013+0.200j
4	-0.000301-0.0000329j
5	0.0016-0.0020j
6	0+0.0017j

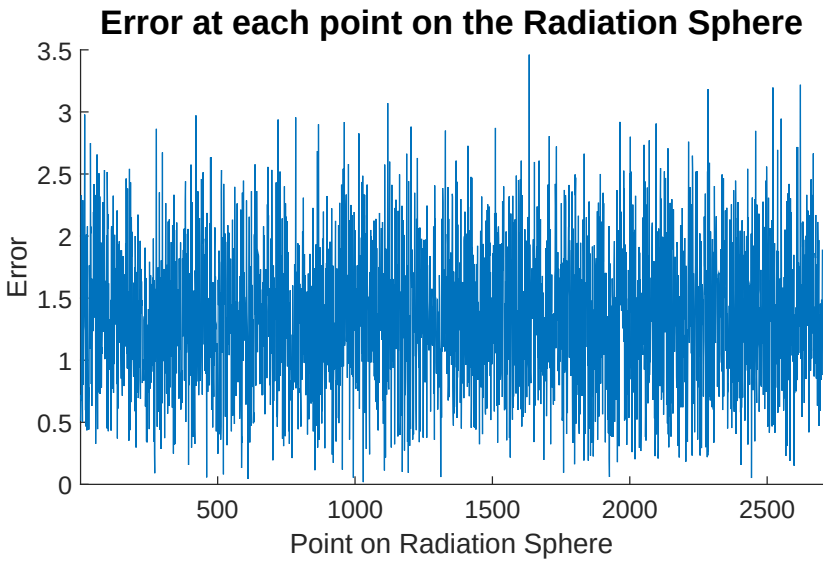

Figure 4.6: Mean-squared error between the desired electric field and the goal at each point when the goal pattern is a linear combination of characteristic far-fields plus random noise at each point on the radiation sphere

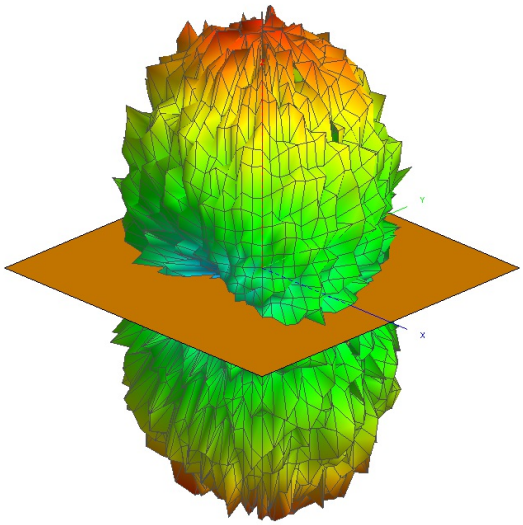

Figure 4.7: Goal radiation pattern

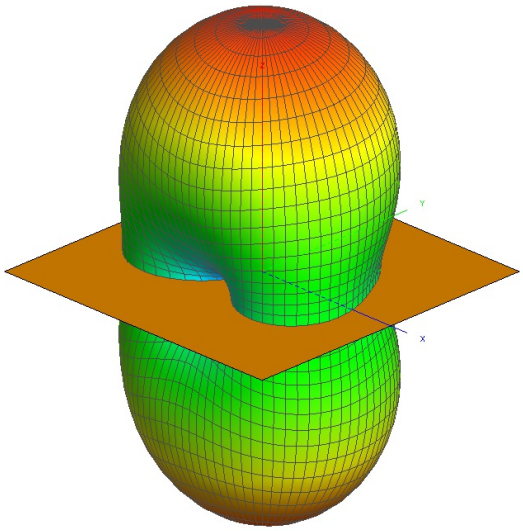

Figure 4.8: Resulting radiation pattern

Table 4.3: Resulting modal weighting coefficients when goal pattern is a an isotropic power pattern

Mode	Coefficients
1	0.0000036+0.00049j
2	-0.0000038+0.00012j
3	0.0000022+0.000000097j
4	-0.000301-0.0000329j
5	-0.0000066+0.00000016j
6	-0.0000020+0.000000081

the modal weighting coefficients that minimize the amount of error.

Based on the input goal pattern the resulting modal weighting coefficients are in Table 4.3. While the weights are small, comparatively, the fourth mode has a larger magnitude compared to the other five modes. The average error is 1.1731. If the error in the ϕ polarization is evaluated, the average error is .1731. Therefore, the average error for the $\hat{\phi}$-polarized field is very small. The resulting field in the θ direction is 0 which explains why the average error contribution at each point from the θ direction is 1. The plot for the error is shown in Figure 4.9. The total resulting pattern is omni-directional and ϕ-polarized. Figure 4.10 depicts the resulting far field in the isotropic case. There is a null along the z-axis which accounts for the peaks in Figure 4.9 as the points get closer to the z-axis.

The three different goal patterns for the square plate showcase the power of this method to solve for complex modal weighting coefficients when the characteristic far fields are also complex. When a goal pattern was constructed using a linear combination of modes, the method was able to almost perfectly retrieve the modal weighting coefficients. Even with addition of random noise, the program was able to get modal weighting coefficients that resulted in the minimum mean-square error. When the input pattern was impossible to achieve, modal weighting coefficients were returned that generated the pattern that was closest to the goal radiation pattern. The resulting radiation pattern contained a null, which is expected given the geometry of the square plate. These patterns also all arose from the same geometry, showing a range of different achievable radiation patterns. While the structure is not capable of achieving all possible goal radiation patterns, it is important to come as close as possible.

The last verification test compares the solved modal weighting coefficients

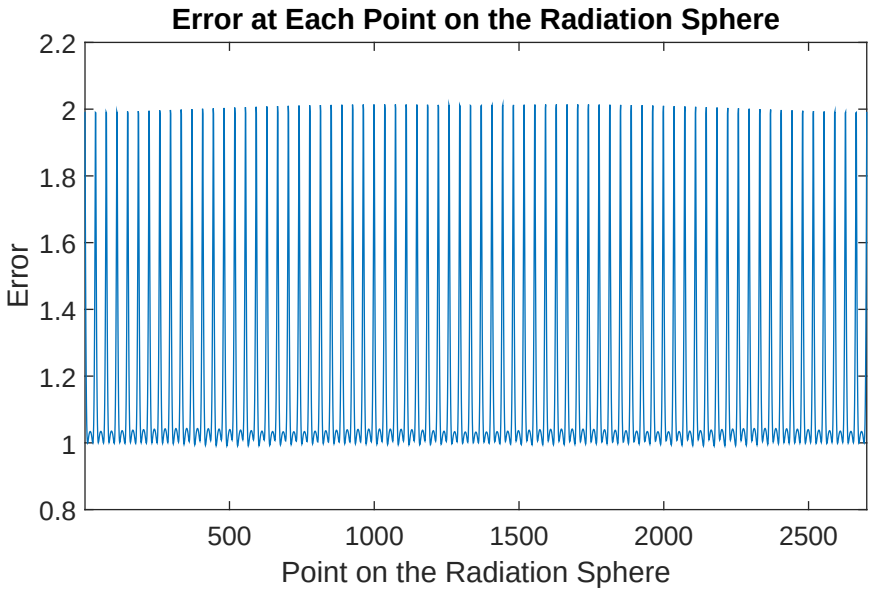

Figure 4.9: Error at each point using an isotropic goal pattern

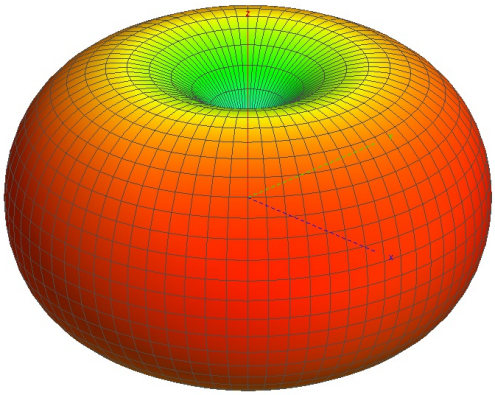

Figure 4.10: Radiation pattern resulting from an isotropic goal pattern for a square plate

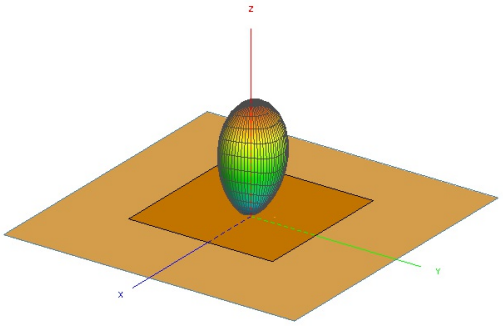

Figure 4.11: Radiation pattern resulting from a patch antenna over an infinite ground plane

to the actual modal weighting coefficients for an excited antenna. Once the antenna is excited, the radiation pattern and true modal weighting coefficients can be calculated. The radiation pattern for the excited structure is used is the goal pattern for the developed method. If the method works, the method should output similar modal weighting coefficients to those calculated from model with the excitation.

A 3 GHz patch antenna matched to 50 Ω with the far field shown in Figure 4.11 was designed to test this method. Table 4.4 shows the differing modal weights. The modal weights given by the excitation are very close to the ones calculated by the program. The differences could very easily be due to computer numerical error due to the reporting accuracy of the output goal pattern and the characteristic far-fields. The average error between the goal pattern and the recreated pattern is $1.5997 * 10^{-5}$ and the maximum is $3.8730 * 10^{-5}$. This is compared to goal patterns where the maximum field strength is 3. This patch antenna over an infinite ground plane shows that for a typical antenna, the software can work to produce the modal weighting coefficients corresponding to the pattern goal.

While this method works extremely well, it relies on the specification of both power and polarization for many points on the radiation sphere. The next section will derive a similar method for the case where only the power, not the polarization, is specified.

Table 4.4: Modal weighting coefficients calculated once using the excitation and again using the developed method to minimize the mean-square error between the goal pattern and the weighted sum of the characteristic far-fields

Mode	Excitation	Minimum Error
1	$0.1813e^{j36.88^\circ}$	$0.1813e^{j36.8880^\circ}$
2	$0.0002e^{j136.8248^\circ}$	$0.0002e^{j137.5103^\circ}$
3	$0.0251e^{j91.1762^\circ}$	$0.0252e^{j91.1714^\circ}$
4	$0.000000127e^{j89.60616^\circ}$	$0.000000734e^{-j9.2192^\circ}$
5	$0.000000241e^{j89.7139^\circ}$	$0.000000884e^{j157.6534^\circ}$

4.3 Pattern Synthesis Specifying Only Power

As previously stated, it can be advantageous to specify only the power and not both power and polarization. I will first derive the method for solving for the modal weighting coefficients in this case and then verify this method using a variety of tests, similar to those completed for the last section.

The error function for the power pattern is

$$\epsilon = \sum_{m=1}^{M} ||A_\theta^m[\alpha]|^2 + |A_\phi^m[\alpha]|^2 - F^m|^2 \tag{4.34}$$

where A_θ, A_ϕ, and $[\alpha]$ are defined as they were in the previous section. F is the goal power. This can be rewritten as

$$\epsilon = \sum_{m=1}^{M} |[\alpha]^{*T} A_\theta^{m*T} A_\theta^m[\alpha] + [\alpha]^{*T} A_\phi^{m*T} A_\phi^m[\alpha] - F^m|^2. \tag{4.35}$$

To simplify the notation

$$B^m = A_\theta^{m*T} A_\theta^m + A_\phi^{m*T} A_\phi^m. \tag{4.36}$$

With the simplified notation, the error becomes

$$\epsilon = \sum_{m=1}^{M} |[\alpha]^{*T} B^m[\alpha] - F^m|^2. \tag{4.37}$$

This can be expanded to

$$\epsilon = \sum_{m=1}^{M} [[\alpha]^{*T} B^m [\alpha] - F^m]^{*T} [[\alpha]^{*T} B^m [\alpha] - F^m]. \tag{4.38}$$

$[\alpha]^{*T} B^m [\alpha] - F^m$ is simply a number. The number must be real because both $[\alpha]^{*T} B^m [\alpha]$ and F^m are magnitudes. With this in mind, the error can simplified further to

$$\epsilon = \sum_{m=1}^{M} ([\alpha]^{*T} B^m [\alpha])^2 - 2[\alpha]^{*T} B^m [\alpha] F^m - (F^m)^2. \tag{4.39}$$

Use

$$x^m = [\alpha]^{*T} B^m [\alpha] \tag{4.40}$$

and substitute into Equation 4.39 to get

$$\epsilon = \sum_{m=1}^{(} M)(x^m)^2 - 2x^m F^m - (F_m)^2. \tag{4.41}$$

To minimize the error, take the derivative of ϵ with respect to x and find the minimum. The derivative of Equation 4.41 can be written as

$$\frac{d\epsilon}{dx} = \sum_{m=1}^{M} 2x^m - 2F^m. \tag{4.42}$$

By setting the derivative to 0, Equation 4.42 can be rewritten as

$$\sum_{m=1}^{M} 2x^m = \sum_{m=1}^{M} F^m. \tag{4.43}$$

Because the sums are identical, this reduces to solving for where

$$[\alpha]^{*T} B^m [\alpha] = F^m. \tag{4.44}$$

Equation 4.44 can be used to derive a system of equations to best identify the real and imaginary parts of the modal weighting coefficients whose weighted sum has the far field pattern that most closely approximates the goal power pattern. Because Equation 4.44 has to be evaluated at each

point on the radiation sphere, this can be viewed as a set of M equations to find 2N unknowns (real and imaginary component of each modal weighting coefficient).

Because the goal is a power pattern with polarization left unspecified, there may be multiple sets of modal weighting coefficients that produce identical errors. I use a variety of estimates for the initial guess of the modal weighting coefficients to ensure attempt to ensure the calculated solution minimizes the error in the radiation pattern.

To better understand how to solve for the real and imaginary parts of α, Equation 4.44 can be written out for when N = 4. Before Equation 4.44 is written out explicitly for a specific N, it is important to note some properties of B^m. Because of the definition of Equation 4.36, B^m must be a NxN Hermitian matrix where the diagonal elements are real valued. When N = 4, Equation 4.44 looks like the matrix equation found in 4.46 when B^m is represented as

$$\begin{bmatrix} a_m & b_m & c_m & d_m \\ b_m^* & e_m & f_m & g_m \\ c_m^* & f_m^* & h_m & i_m \\ d_m^* & g_m^* & i_m^* & j_m \end{bmatrix} \tag{4.45}$$

$$\begin{bmatrix} \alpha_1^* & \alpha_2^* & \alpha_3^* & \alpha_4^* \end{bmatrix} \begin{bmatrix} a_m & b_m & c_m & d_m \\ b_m^* & e_m & f_m & g_m \\ c_m^* & f_m^* & h_m & i_m \\ d_m^* & g_m^* & i_m^* & j_m \end{bmatrix} \begin{bmatrix} \alpha_1 & \alpha_2 & \alpha_3 & \alpha_4 \end{bmatrix} = F^m. \tag{4.46}$$

By multiplying out the matrices and simplifying, this can be written as

$$\begin{aligned} F^m =& |\alpha_1|^2 a_m + 2Re(\alpha_1^*\alpha_2)Re(b_m) + 2Im(\alpha_1^*\alpha_2)Im(b_m) + 2Re(\alpha_1^*\alpha_3)Re(c_m) \\ &+ 2Im(\alpha_1^*\alpha_3)Im(c_m) + 2Re(\alpha_1^*\alpha_4)Re(d_m) + 2Im(\alpha_1^*\alpha_4)Im(d_m) + |\alpha_2|^2 e_m \\ &+ 2Re(\alpha_2^*\alpha_3)Re(f_m) + 2Im(\alpha_2^*\alpha_3)Im(f_m) + 2Re(\alpha_2^*\alpha_4)Re(g_m) \\ &+ 2Im(\alpha_2^*\alpha_4)Im(g_m) + |\alpha_3|^2 h_m + |\alpha_4|^2 j_m + 2Re(\alpha_3^*\alpha_4)Re(i_m) \\ &+ 2Im(\alpha_3^*\alpha_4)Im(i_m). \end{aligned} \tag{4.47}$$

The equation can be further expanded using

$$\alpha_1 = m + nj, \tag{4.48a}$$
$$\alpha_2 = o + pj, \tag{4.48b}$$
$$\alpha_3 = q + rj, \tag{4.48c}$$
$$\alpha_4 = s + tj. \tag{4.48d}$$

The expanded form is written as

$$\begin{aligned} f_m =&(m^2+n^2)a_m + 2(mo+np)Re(b_m) + 2(pm-no)Im(b_m) \\ &+ 2(mq+nr)Re(c_m) + 2(mr-nq)Im(cm) + 2(ms+nt)Re(d_m) \\ &+ 2(mt-ns)Im(d_m) + (o^2+p^2)e_m + 2(oq+pr)Re(f_m) \\ &+ 2(or-pq)Im(f_m) + 2(os+pt)Re(g_m) + 2(ot-ps)Im(g_m) \\ &+ (q^2+r^2)h_m + 2(qs+rt)Re(i_m) + 2(qt-rs)Im(i_m) + (s^2+t^2)j_m. \end{aligned} \tag{4.49}$$

From Equation 4.49, it is very clear that the equations being used to solve for the real and imaginary parts of the modal weighting coefficients are nonlinear. The Newtown-Raphson method for finding roots of a real-valued function can be used to find possible solutions for the modal weighting coefficients based on the system of nonlinear equations. Newton's method can result in a variety of solutions, especially if the problem is not convex. Additionally, because the goal is a power pattern and not a particular polarization, there may be multiple sets of modal weighting coefficients that produce similar errors. By starting from a variety of different places and comparing the error of different solutions, it is possible to find a solution that does its best to minimize over all possible values for modal weighting coefficient. For some starting values the method may not converge. For this reason it is important to start at a variety of randomly selected starting points and compare the resulting error. The modal weighting coefficients that result in the minimum error should be used.

To verify that this method works, similar tests will be run to those to verify the method for the previous section.

Table 4.5: Magnitude of the modal weighting coefficients calculated using the excitation and calculated to find the minimum mean-square error between the goal power pattern and the weighted sum of the modal characteristic fields for a dipole

Mode	Excitation	Minimum Power Error
1	0.0964	.0963
2	$2.149 * 10^{-13}$	$1.719 * 10^{-11}$
3	0.000136	.00358

4.3.1 Dipole

The dipole will be the first geometry evaluated using the power pattern technique. A 5 cm dipole is simulated at 3 GHz and the first three characteristic far-fields are found. The goal power pattern is chosen to be the power associated with the theoretical far-field pattern for a dipole of a resonant length. Using the characteristic far-fields and the goal pattern, the developed method can be used to solve for the modal weighting coefficients. The dipole can then be excited in the software and the resulting modal weighting coefficients can be compared to the ones that were calculated using the characteristic far-fields.

The magnitudes of the modal weighting coefficients can be found in Table 4.5. The magnitudes of the coefficients are seen to be very close. Because the modal weighting coefficients have extremely similar magnitudes, the next step is to evaluate the error between the resulting pattern and the power pattern for a dipole. For the dipole, the average error is $5.0851 * 10^{-8}$ and the maximum error at any one point is $2.6904 * 10^{-7}$. The error at each point is plotted in Figure 4.12.

4.3.2 Patch Antenna

The patch antenna over an infinite ground plane from the previous section was used to verify the method for the power method as well. The goal pattern was chosen to be the power from the resulting far field of a probe-fed patch. The modal weighting coefficients calculated using the characteristic far-field can then be compared to those calculated using the excitation of the patch. The resulting modal weighting coefficients are found in Table 4.6. The magnitude of the modal weighting coefficient for each mode closely matches

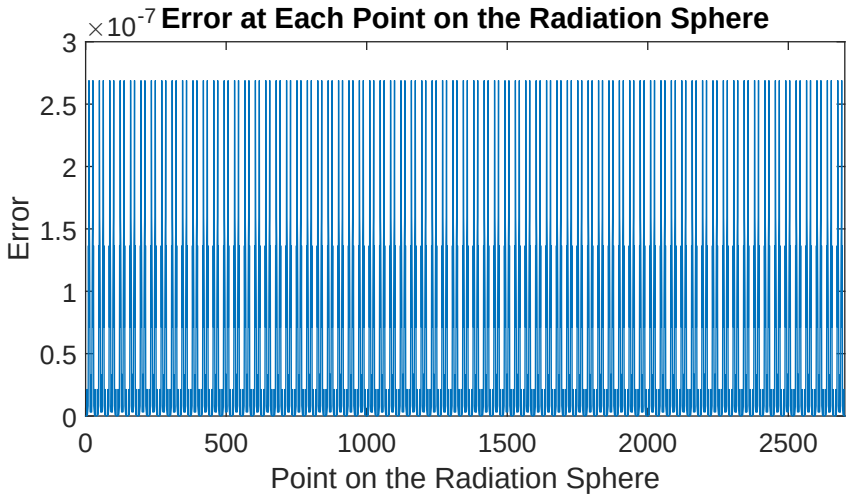

Figure 4.12: Error in power pattern at each point for the power patter of a dipole

Table 4.6: Modal weighting coefficients calculated once using the excitation and again using the developed method to minimize error between the goal power pattern and the weighted sum of the characteristic far-fields

Mode	Excitation	Minimum Error
1	$0.1813e^{j36.88°}$	$0.1876e^{-j40.6278°}$
2	$0.0002e^{j136.8248°}$	$0.0115e^{j61.6658°}$
3	$0.0251e^{j91.1762°}$	$0.0242e^{-j93.0749°}$
4	$0.000000127e^{j89.60616°}$	$0.000963e^{-j137.367°}$
5	$0.000000241e^{j89.7139°}$	$0.00606e^{j142.374°}$

those given by the patch antenna. The mean of the error is $6.08 * 10^{-5}$. The error for the patch antenna is still very small even though the patch antenna uses both polarizations unlike the dipole example.

The power at each point in the radiation sphere is compared and the resulting error is plotted in Figure 4.13. The mean of the error is $6.08 * 10^{-5}$. This error is extremely small and thus the far-field power pattern for the patch antenna is the same as Figure 4.11.

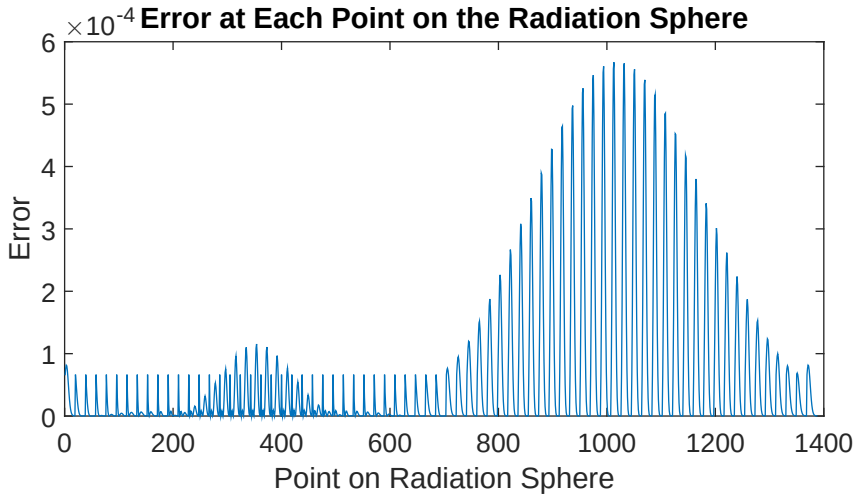

Figure 4.13: Error in power pattern at each point for the power pattern of a patch antenna over an infinite ground plane

4.3.3 Isotropic Antennas

Isotropic antennas provide an interesting test case for a power pattern. Unlike when specifying isotropic power and polarization, isotropic power patterns are achievable for some types of antenna geometries. Saunders uses a distribution of infinitesimal turnstile antennas to show that it is possible to create an antenna with unit power in all directions; however, the polarization will change throughout [69]. A distribution of turnstile antennas is difficult to model and build and not extremely practical. To combat this issue, Saunders also shows that a simple array of two electrically small turnstile antennas produces a nearly isotropic far field for practical applications.

For this reason a two-element array of turnstile antennas is chosen as the geometry to find the modal weighting coefficients that best approximate an isotropic radiated power antenna. Each turnstile antenna element is $\frac{\lambda}{10}$ at the center frequency of 3 GHz. The turnstile antenna elements are spaced $\frac{\lambda}{2}$ apart. The modeled turnstile array is shown in Figure 4.14. The turnstile array is evaluated as one combined structure, not multiple individual structures. Using these modal weighting coefficients, it is possible to solve for the resulting far field.

The goal pattern is specified at every point with a power of 1. The first 4

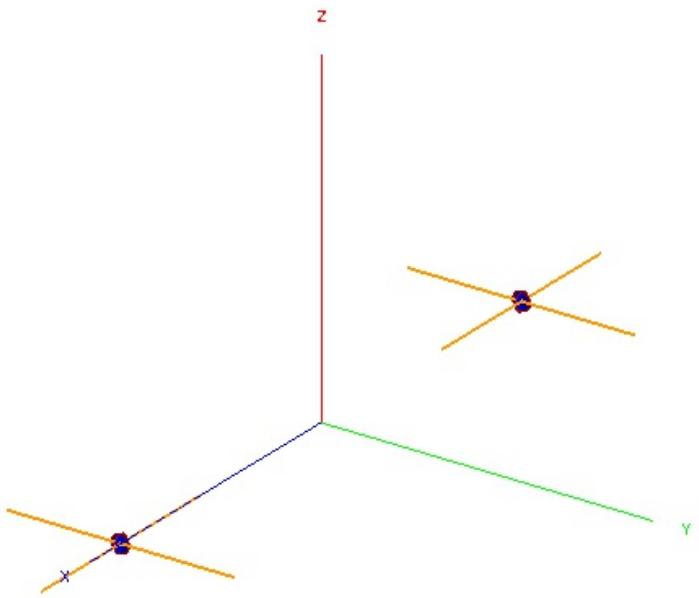

Figure 4.14: Geometry of modeled turnstile array

Table 4.7: Magnitude of the modal weighting coefficients to approximate an isotropic radiation pattern for turnstile array

Mode	Minimum Power Error
1	$0.1131 - 0.0519$j
2	$-0.0264 - 0.0565$
3	$0.0325 + 0.0707$j
4	$-0.0738 + 0.0343$j

modes of the turnstile array are used in finding the optimal modal weighting coefficients. The modal coefficients are in Table 4.7. Using these modal weighting coefficients, it is possible to solve for the resulting far-field. Figure 4.15 shows the output power at each point on the sphere in dB. The largest null in the radiation pattern is 1.443 dB deep and the peak gain is only .7503 dB. The overall pattern has only 2.1950 dB of variation over its entirety making the pattern very close to the isotropic power antenna desired. The far-field pattern in dB is shown in Figure 4.16.

Another common antenna that is used to achieve isotropic power is an electrically small array of three loops and three dipoles. Each dipole is oriented along either the x, y, or z-axis and the loops are in the XY, XZ, and YZ planes all centered at the origin. The radius of the element is $\frac{\lambda}{10}$ at the

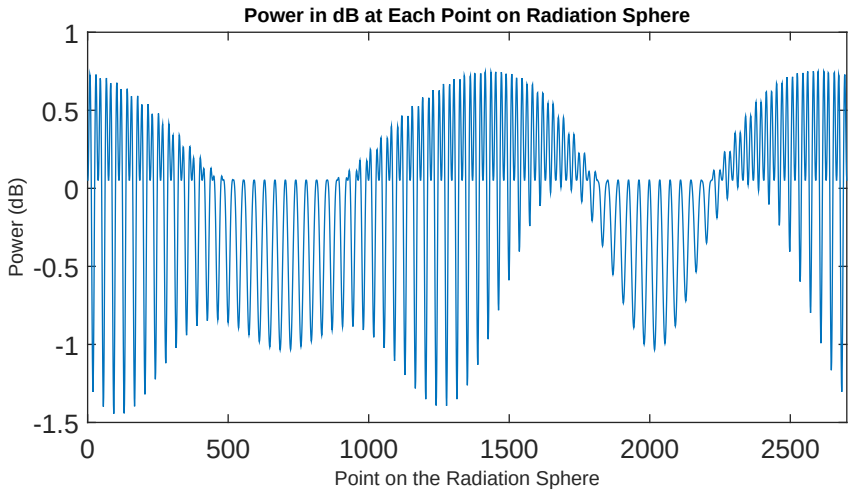

Figure 4.15: Power in dB at each point on the radiation sphere resulting from pattern optimization of a turnstile array

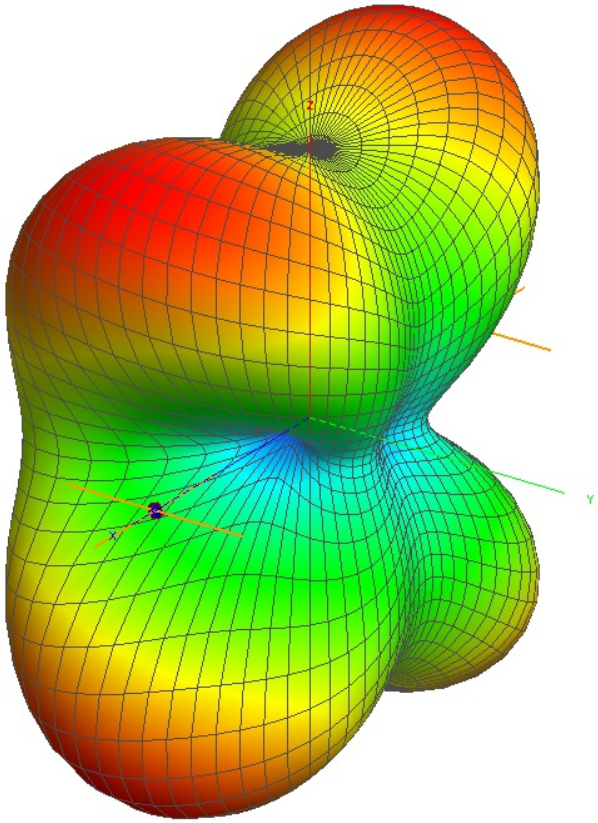

Figure 4.16: Isotropic power pattern for turnstile array

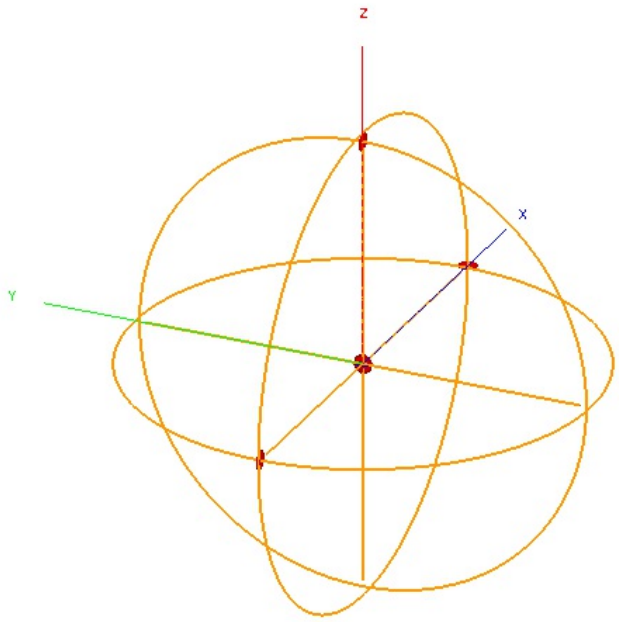

Figure 4.17: Geometry of modeled 3-loop, 3-dipole antenna

center frequency of 3 GHz as shown in Figure 4.17.

Using the first fourteen characteristic far-fields, the developed process is used to solve for the modal weighting coefficients leading to the smallest difference between the radiation pattern and an isotropic power pattern. The corresponding modal weighting coefficients can be found in Table 4.8. The maximum field variation over the sphere is 0.0299 dB. This verification test highlights that while the turnstile array can get close, the 3-loop, 3-dipole configuration can produce a radiation pattern much closer to a truly isotropic pattern.

The power at each point on the radiation sphere can be seen in Figure 4.18. The error range for this antenna is much smaller than for the turnstile antenna modeled previously. For this antenna the largest power is 1.0035 and the smallest is at 0.9966. To better put this in perspective, the power in dB is plotted in Figure 4.19. Figure 4.20 shows the resulting far-field.

The difference in error size when approaching an isotropic power pattern using the turnstile array and the 3-loop, 3-dipole antenna element exemplifies the power of characteristic modes for developing an understanding of what is physically realizable. It shows that the turnstile array is a close approx-

Table 4.8: Magnitude of the modal weighting coefficients to approximate an isotropic radiation pattern

Mode	Minimum Power Error
1	$0.0010 - 0.0024\text{j}$
2	$0.0253 - 0.0756\text{j}$
3	$-0.0109 - 0.0031\text{j}$
4	$-0.0431 + 0.1268\text{j}$
5	$-0.0822 - 0.0283\text{j}$
6	$-8.433 * 10^{-4} - 4.0175 * 10^{-4}\text{j}$
7	$-0.0031 + 0.0093\text{j}$
8	$-0.0069 + 0.0203\text{j}$
9	$0.0033 + 0.0096\text{j}$
10	$0.0156 + 0.0053\text{j}$
11	$-0.0088 - 0.0031\text{j}$
12	$0.0032 - 0.0098\text{j}$
13	$-0.0048 + 0.0142\text{j}$
14	$-0.0042 - 0.0014\text{j}$

imation to an isotropic power pattern while the 3-loop, 3-dipole antenna is able to create a pattern that is much closer to unity gain.

The developed method calculates modal weighting coefficients that will result in the closest physically realizable pattern to the goal pattern. The development allows for the use of complex characteristic far-fields compared to past methods that relied on using equiphase modal weighting coefficients.

Knowing the modal weighting coefficients shows what current distribution must be achieved on the surface of the platform to create a desired radiation pattern. Based on the required current distribution, feed positions and matching networks can be developed that allow for the platform to radiate in the desired fashion. The methods also allow an antenna designer to demonstrate the best possible scenario for the pattern given the current platform. If that pattern is insufficient for the communication system, it is possible to redesign or reevaluate the platform to find a shape that is better suited to radiate in the desired fashion.

The next chapter describes a novel synthesis method that uses the developed techniques from this chapter to design and install antenna elements for multiple frequency bands onto the same platform.

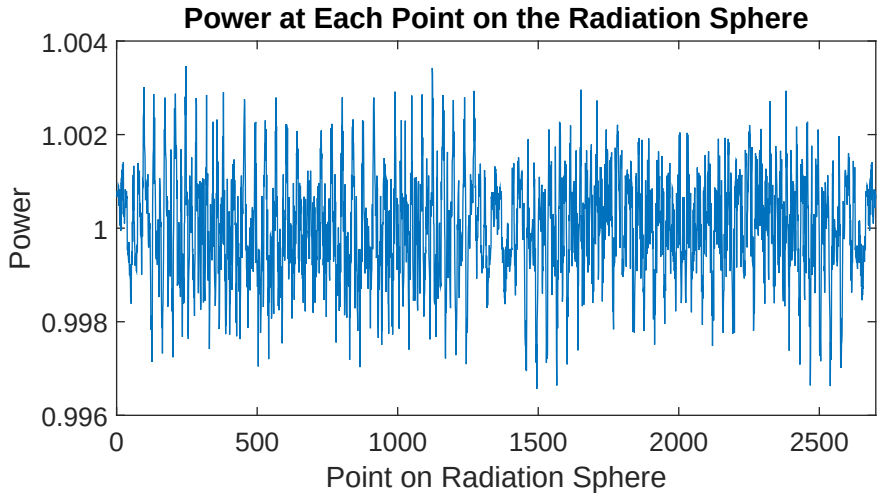

Figure 4.18: Power at each point on the radiation sphere resulting from pattern optimization of 3 loops and 3 dipoles

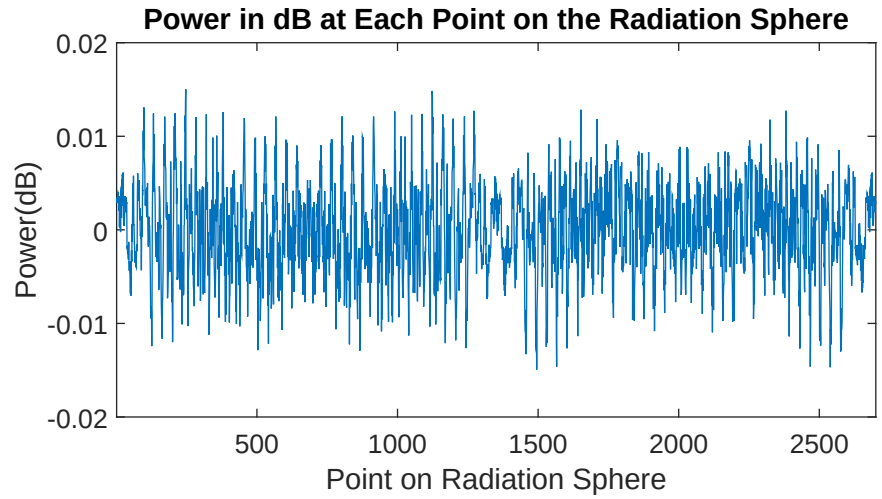

Figure 4.19: Power in dB at each point on the radiation sphere resulting from pattern optimization of 3 loops and 3 dipoles

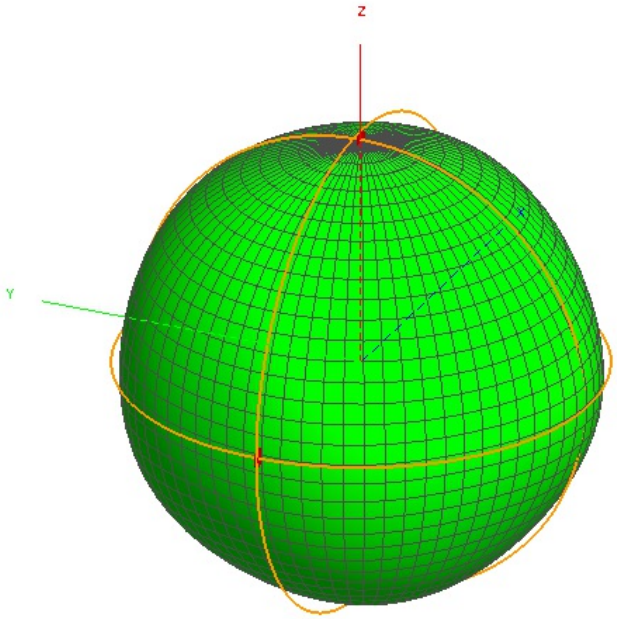

Figure 4.20: Isotropic power pattern for three loops and three dipoles

CHAPTER 5

SYNTHESIS METHOD

The methods described in the two previous chapters calculate the necessary surface current on the structure to achieve the desired radiation pattern. These methods can be combined to create a synthesis method for antennas that are installed on platforms and need to have a desired radiation pattern. The most common methodology for installing multiple antennas on platforms seems to be to design elements, install them on the platform, and then check the radiation pattern [3, 70]. In cases where a certain radiation pattern is required, this method will only show the distortion of the original element pattern by the platform and other installed antennas. This leads to sub-optimal gains, patterns and isolation when the antennas are finally installed together on a platform. The provided synthesis method utilizes the desired surface currents on the platform to better understand which elements to install, how to install them, and how to ensure one band does not interfere with another band on the structure itself. This synthesis method describes how to install multiple antennas on a single platform where each band has a desired radiation pattern.

The synthesis method begins by solving for the characteristic modes on the structure at all frequencies of interest. The designer may want to solve for relevant modes on the structure from the low end of the lowest frequency band to the high end of the highest frequency band to gain better insight into how the modes track across frequency on the structure. Tracking the modes across frequency is not necessary but it does lend insight to latter parts of the design process if it becomes difficult to achieve the desired radiation pattern and a match at the desired frequency. The next step is to evaluate the modal radiation patterns for each frequency band of interest. If any of the modal characteristic far fields achieves the desired radiation pattern, the desired surface current for that band is equivalent to the modal surface current. If no mode displays the characteristics of the desired radiation pattern, one

of the methods from Chapter 4 must be used to determine the closest the platform can get to radiating the desired radiation pattern and the surface current on the platform required at the frequency band of interest to generate the appropriate radiation pattern.

Once the surface currents have been calculated for the bands of interest, the surface currents must be compared to one another. Feed points should go in a position with higher than average current. The feed point is not required to be the current maximum but there should be substantial current at the frequency of interest near the feed point. The feed point should be chosen, if possible, to be at a higher current point for that frequency that is a low current point for all other frequencies of interest. This attempts to ensure that the feed point position causes minimal interference on the structure. If two feeds should be near the same place, it is possible, but the element design can get substantially trickier to ensure the appropriate currents are excited for each band.

In addition to just evaluating areas of high current and low current, there are other important factors to note about the desired current structures. For surface currents with multiple areas of high current, it is important to evaluate the phase difference between the high current points. This phasing must be enforced to ensure the appropriate surface current and thus the radiation pattern is achieved. When phasing points on the structure together, it is important to note if other surface currents will be significantly disrupted by any connection. For example if another has high current at some of the points but not all, it is important to ensure the additional structure meets the phasing needs for all frequency bands of interest. If this is not taken into account, one could tie two points on the structure together using the element and disrupt operation on the antenna for the other bands of interest.

With the ideas from the previous two paragraphs, the designer then chooses feed points in areas of high current for the desired surface current. These feed points will be the basis of the next step that will start the element design and come close to achieving the desired radiation patterns when all the elements are installed together on the platform.

Once the surface currents have been evaluated for the high points, the next step is to start with the low frequency band and the platform. It is important to start from the lower frequency and work up because the lower frequency bands often require more added elements to be appropriately

matched. The additional metal is more likely to cause issues with the higher bands. The lower band is also less susceptible to the smaller changes from higher frequencies. For this reason the lower band elements are designed first and then the higher bands are added. Starting from the desired high current point identified earlier, the element should remain close to the surface of the platform and along the direction of current flow from that point. Shorts can be added back to the structure at various distances to create other current high points and provide for matching, especially when the platform is fairly small compared to a wavelength. This is much like the process for designing antenna elements for the examples in Chapter 3.

Once the lowest band antenna has been designed and is functioning properly, the next step is to evaluate and design the antennas for the second lowest frequency using the same techniques. Once this element has been designed, check and ensure the radiation pattern from the low band is still functioning properly. As long as the high current points for the lowest frequency band do not significantly overlap with high current points for the next highest frequency band, there should be little impact to the lowest frequency band's radiation pattern. If the lowest frequency band's pattern is not as expected, the current can be evaluated on the structure at the lowest frequency band to see if it has deviated significantly from the magnitude and phase of the desired platform current. If the pattern/current have diverged from the desired patterns, the designer should redesign the antenna element for the lowest band until the platform surface current looks sufficiently like the goal current and the radiation pattern resembles the desired radiation pattern.

The method then has an antenna designer continue working methodically higher in frequency. After designing and adding an element for a new frequency, all the lower frequencies bands should be checked to ensure they are still tuned and radiating appropriately. The designer can make small adjustments to the elements here to account for any small differences in coupling that may lead to the elements tuning out of band or small shifts in radiation pattern nulls. This will also give insight into slight adjustments that may need to be made in the implementation of the structure due to slight differences between simulation and the fabricated antenna. By moving up the frequencies methodically and checking the lower frequencies after each new installation, the designer will know exactly which elements have the

strongest coupling and gain an understanding of how to tune the antennas properly keeping the radiation pattern in mind. Once the highest frequency element has been installed and all the lower band elements checked to ensure they are still tuned appropriately, the antenna system can be fabricated and the radiation patterns for each band will be close to the designed radiation patterns.

This synthesis method gives a systematic way to install antennas on a platform to ensure that they are phased appropriately and utilize the entire platform as part of their radiating structure. This can lead to greater gains and ensures that the radiation patterns are designed appropriately instead of just installing antennas together on a platform and hoping that the platform distortion to the pattern is minimal.

To show how this would be implemented in practice, multiple antennas will be installed on a CubeSat chassis. For a CubeSat, the antennas must take up minimal physical volume in order to preserve the remaining space for instrumentation. The CubeSat also has additional limitations because nothing can exceed the dimensions of the launch vehicle on launch. The antennas cannot exceed the outer dimensions. With these antennas one also does not want to traverse the center because most of the center of the antennas will be filled with electronics. If significant portions of the elements are in the center of the CubeSat, the electronics will be in the near field of the elements. If the resulting radiation pattern is dependent on the propagation from the internal elements, this will most certainly be disrupted by the additional electronics. By constraining the elements to the outside of the antenna, the impact of additional electronics can be limited. Current CubeSat antennas often rely on small crossed dipoles that pop out after launch to be able to communicate with the CubeSat once it has reached orbit [71].

CubeSat antennas have been the subject of many different research projects. Many often use stacked patches and other planar antenna design to avoid having to deploy the antenna while also achieving optimal gain [72, 73]. The authors utilize stacked patches in lieu of the deployable solutions to have more gain towards earth for communication. This, however, is not always a valid strategy if the CubeSat is taking scientific measurements towards Earth. Many of these developments require a camera or sensors on the side of the CubeSat facing towards the Earth's surface. The patch antenna designed in the article must be on the Earth-facing side in order to point the maximum

antenna gain toward the ground station. If the instrumentation has be to on the face pointing towards Earth, the patch antenna cannot be located on that face. If the patch was placed on a different face, the radiation pattern would be significantly weaker towards Earth and the CubeSat would lose the benefit of the directional gain that the patch antenna provides. The goal of this example is to show the strength of the developed synthesis method for the very challenging CubeSat application.

5.1 CubeSat Example

The 3U CubeSat is a very common size for current CubeSat deployments. While some CubeSats are moving to 6U, 12U, and larger builds, the 3U CubeSat allows for some scientific instrumentation along with the necessary subsystems for flight. Because 3U CubeSats are common, it is less difficult to find space on a launch versus some of the larger CubeSat's currently being built and developed. The 3U CubeSat has a very specific profile for the size, and must have certain features so that it can be properly launched from the standard launch vehicles [74]. The basis for this example will be using the required pieces of the 3U CubeSat frame. Figure 5.1 shows the simulated version of the 3U CubeSat to validate this synthesis method.

The 3U CubeSat dimensions are approximately 100 mm x 100 mm x 340.5 mm. The radius of the circular cutout is 12.5 mm and the rectangular cutout is 66 mm x 20 mm. The cutouts are to accommodate instrumentation and other equipment. For this particular CubeSat, there are three communication channels that require antennas installed on the structure. When the CubeSat is in orbit, the CubeSat will measure data from Earth's ionosphere through instrumentation looking through the circular cutout. For this reason, the circular cutout must be facing Earth at all times. There are three important communication paths for this CubeSat. The details about the frequencies, usage, and desired radiation patterns are listed below.

1. Data Reporting- The scenario for this CubeSat includes collecting scientific data and then relaying that information back to a ground station. 400 MHz will be used to send data from the CubeSat to the ground station. The goal for this frequency is to provide a radiation pattern that gets as much power toward Earth as possible. The goal pattern for this frequency has a

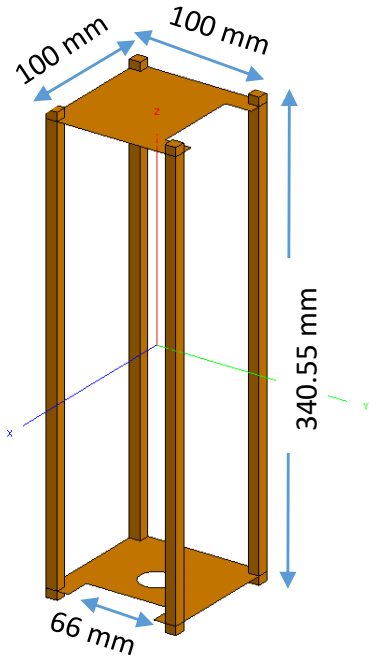

Figure 5.1: Simulated 3U CubeSat structure

linear polarization to align with the station and directs power towards the ground station.

2. Command and Control- The CubeSat also requires an additional channel for command and control separate from the data reporting. This will allow the ground station to communicate with the CubeSat and possible do upgrades or correct any errors after the satellite has launched. This link will utilize the 435 MHz amateur radio band. Much like the previous frequency, this antenna must have a radiation pattern that directs as much power as possible towards Earth. The polarization is more flexible but the power pattern must direct power toward earth.

3. Inter-CubeSat communication - This CubeSat will work as part of a network of other CubeSats in order to collect as much data as possible in conjunction with one another. The CubeSats can send data to one another. This channel also allows for secondary access to a particular CubeSat if the command/control link or the data reporting link go down. This networking will occur at 915 MHz. Because there is no clear idea of where the other CubeSats may be located in space, the target pattern is an omnidirectional pattern in the x-y plane. The CubeSat should be able to effectively commu-

nicate in any direction around the azimuth. The gain will be less towards Earth and directly away from Earth as the CubeSat is oriented in orbit.

Previous research often uses patch antennas facing towards Earth. Because of the instrumentation in this scenario and the lower frequencies being used, the traditional patch antenna facing Earth is not a possible solution for this implementation. There must be a different possibility that can convey the information to the ground station without having an antenna directly on the bottom face. There are additional limitations on the installed antennas. First, the outside of the CubeSat must typically be covered in solar panels to operate all of the inner electronics. For this reason, the side panels cannot be taken up by antennas to ensure that the CubeSat receives maximum solar power to keep it running. In addition, the antennas cannot intrude on, or rely on radiation through, the center of the chassis. Typically electronics fill the center cavity. For this reason the antennas must also occupy little volume in the interior of the CubeSat.

The first step in the process is to complete a characteristic mode analysis on the CubeSat structure to see how many modes are on the structure and how the different modes radiate at the frequencies of interest. Figures 5.2 and 5.3 show the eigenvalues and modal significance values respectively for the 3U CubeSat structure.

Modes with a modal significance below 0.1 are difficult to excite and they do not radiate well enough to couple into the mode effectively as was stated in previous chapters. For this design example, at each of the three frequencies there are a number of modes with modal significance above 0.1. Based on the synthesis method described, the 400 MHz band will be analyzed first.

At 400 MHz, the desire is to build an antenna that whose radiation pattern provides linearly polarized power towards the Earth. There are three modes that have modal significance above 0.1. These three modes have eigenvalues of 0.095, 0.2437, and 0.6725. Figure 5.4 shows the far fields associated with each mode. Based on the far fields pictured, none have a pattern that strongly points towards the ground. Mode 2 even has a large null directly towards Earth in its radiation pattern. Because none of the modal far fields correspond to the desired far field, the next step is to calculate what the best achievable far field would be and the surface current required to achieve that surface current. The reason there is no $-z$ directed far field is because overall there is little current on the bottom of the structure. The reason for

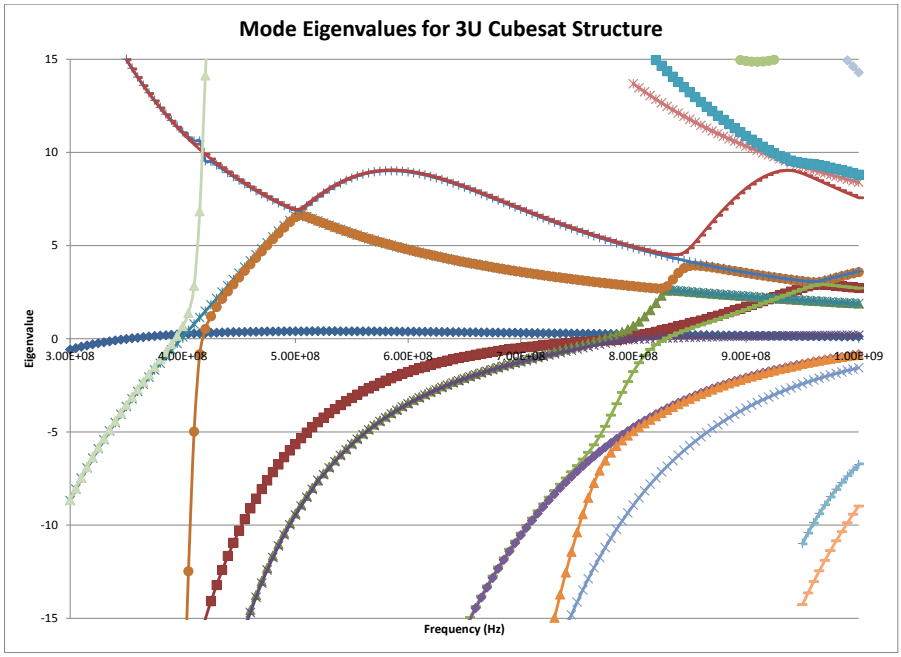

Figure 5.2: Eigenvalue plot for the simulated structure

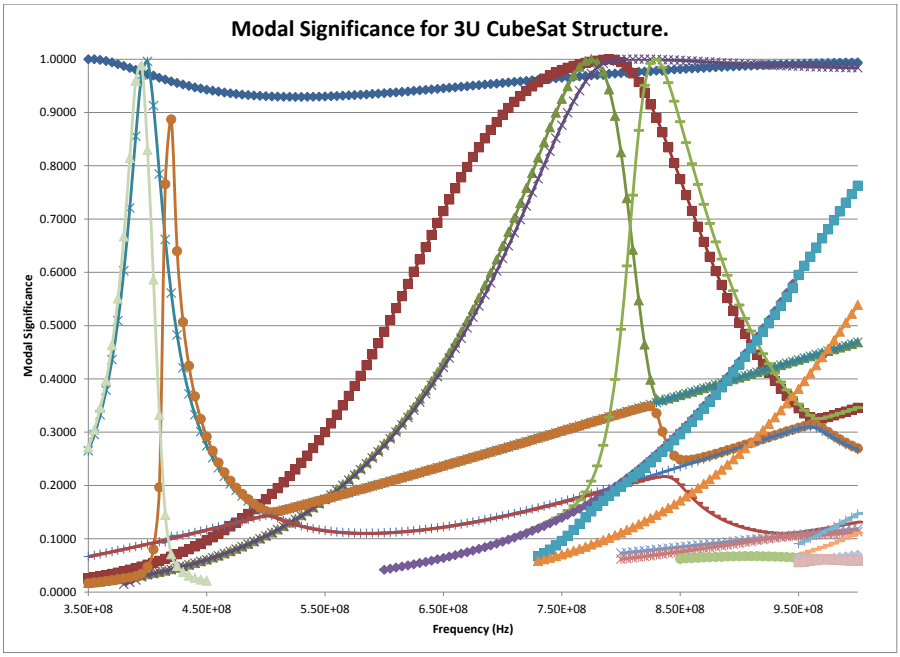

Figure 5.3: Modal significance plot for the simulated structure

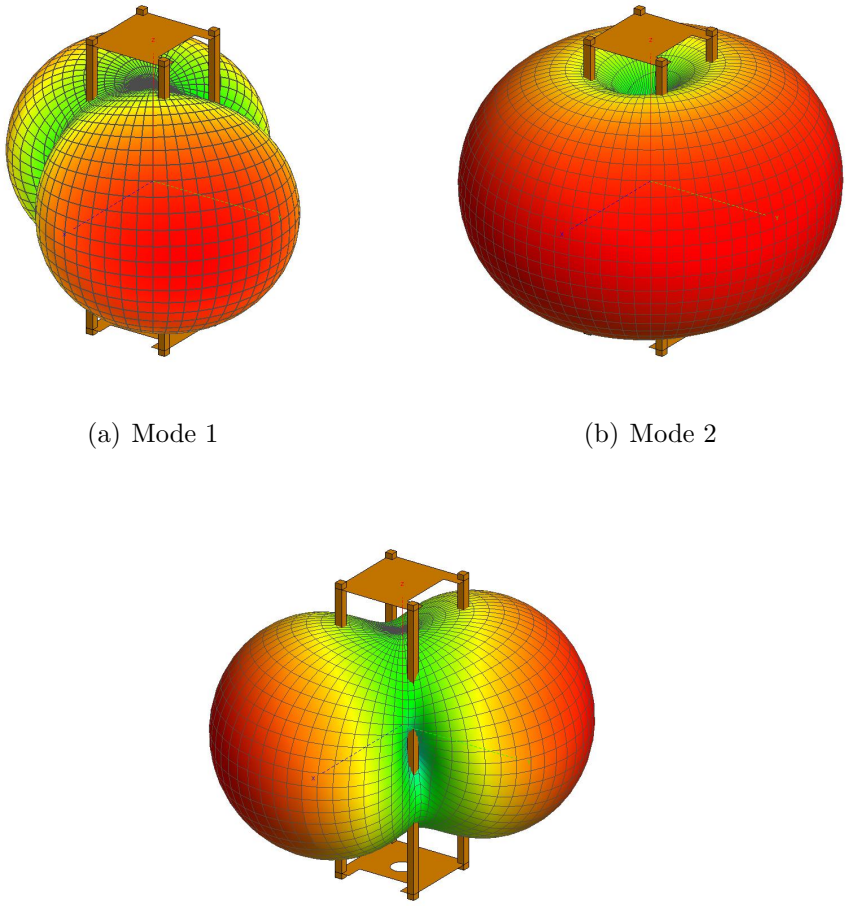

(a) Mode 1

(b) Mode 2

(c) Mode 3

Figure 5.4: Modal far fields for 3U CubeSat at 400 MHz

this is that the bottom plate is small compared to a wavelength. Even if the current is circulating around the edge, the plate is still too small to support the necessary current at 400 MHz. The first method utilizing power and polarization from Chapter 4 will be used to find the best possible achievable pattern as well as solve for the surface current corresponding to that radiation pattern.

The goal pattern at 400 MHz will be the pattern of a patch antenna if it had been facing directly toward Earth. Because the main concern is the power towards Earth and not the power in the remainder of the sphere, only points at or below where θ is 110 degrees will be included in the optimization.

The resulting output from solving for the closest pattern to the goal pattern that is achievable given the structure gives the modal weighting coefficient values of 0.0710 - j0.0369, 0.0356-j0.0048, and 0.0751-j0.0396 respectively. The far field is shown in Figure 5.5 and the corresponding surface current is shown in Figure 5.6. In the figure for the surface current, areas with high current have larger orange arrows. Areas with lower current are marked by short blue arrows. As the color gets closer to red and the arrows get longer, the surface current gets higher. The highest current point is on the lower plate on the edge of the rectangular cutout. Most of the current is on the bottom plate and circulating around the edge. There is a secondary current hot spot near rectangular cutout on the top of the CubeSat. This spot of high current has lower magnitude than the one on the bottom. The resulting far field does not resemble the patch pattern; however, it is the best achievable pattern given the modes on structure.

Now that the optimized pattern and goal surface current are known for the first band, the goal is to produce the same results for each of the higher bands. For 435 MHz, the goal radiation pattern points as much power as possible toward Earth. The characteristic mode analysis performed earlier at this frequency shows 5 modes with modal significance above 0.1. The eigenvalues are 0.330, 2.134, 2.495, 9.117, and 9.171. These five modes all correspond to modal far fields shown in Figure 5.7.

Examining the modal far fields at 435 MHz, none of these far fields come close to having a majority of their power pointing towards Earth. While some of these patterns have power toward Earth, none are particularly strong. For command and control, the goal is to ensure the CubeSat receives instructions from the ground station. The goal with the antenna on the CubeSat is to accept as much power as possible from Earth directions regardless of the polarization. Because the goal in the optimization is power, the method from the second half of Chapter 4 will be used to find the modal weighting coefficients and the surface current that correspond to the pattern that most closely approximates the goal pattern. For this optimization, the pattern is optimized over the bottom hemisphere and the goal pattern has a large gain toward Earth. Instead of using both power and polarization, this will use only power to ensure as much of the pattern as possible is directed towards the Earth. This will hopefully ensure the greatest chance of the CubeSat receiving the command and control signals. Unlike at 400 MHz, where the

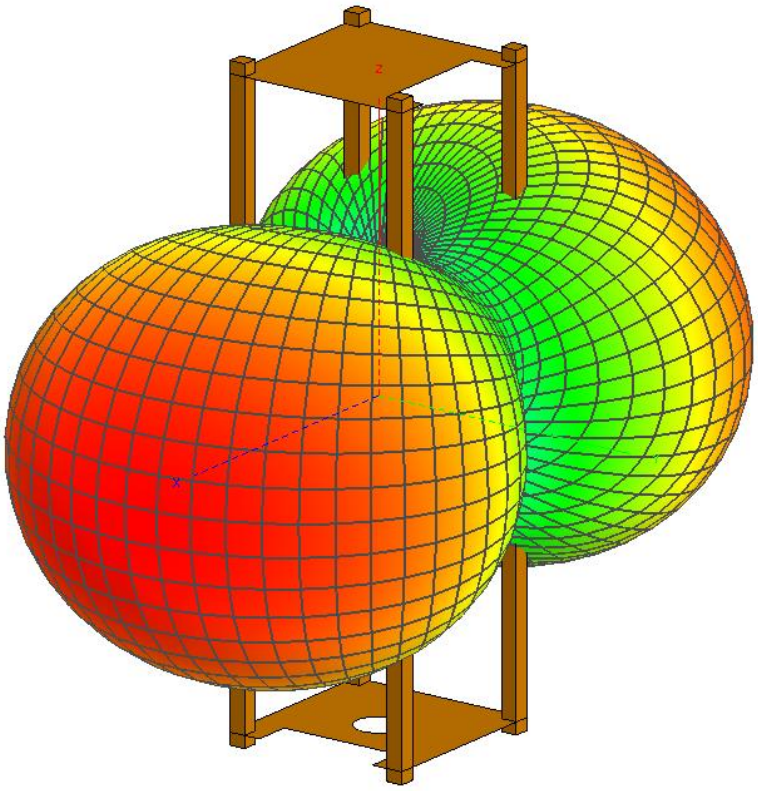

Figure 5.5: Optimized far field at 400 MHz

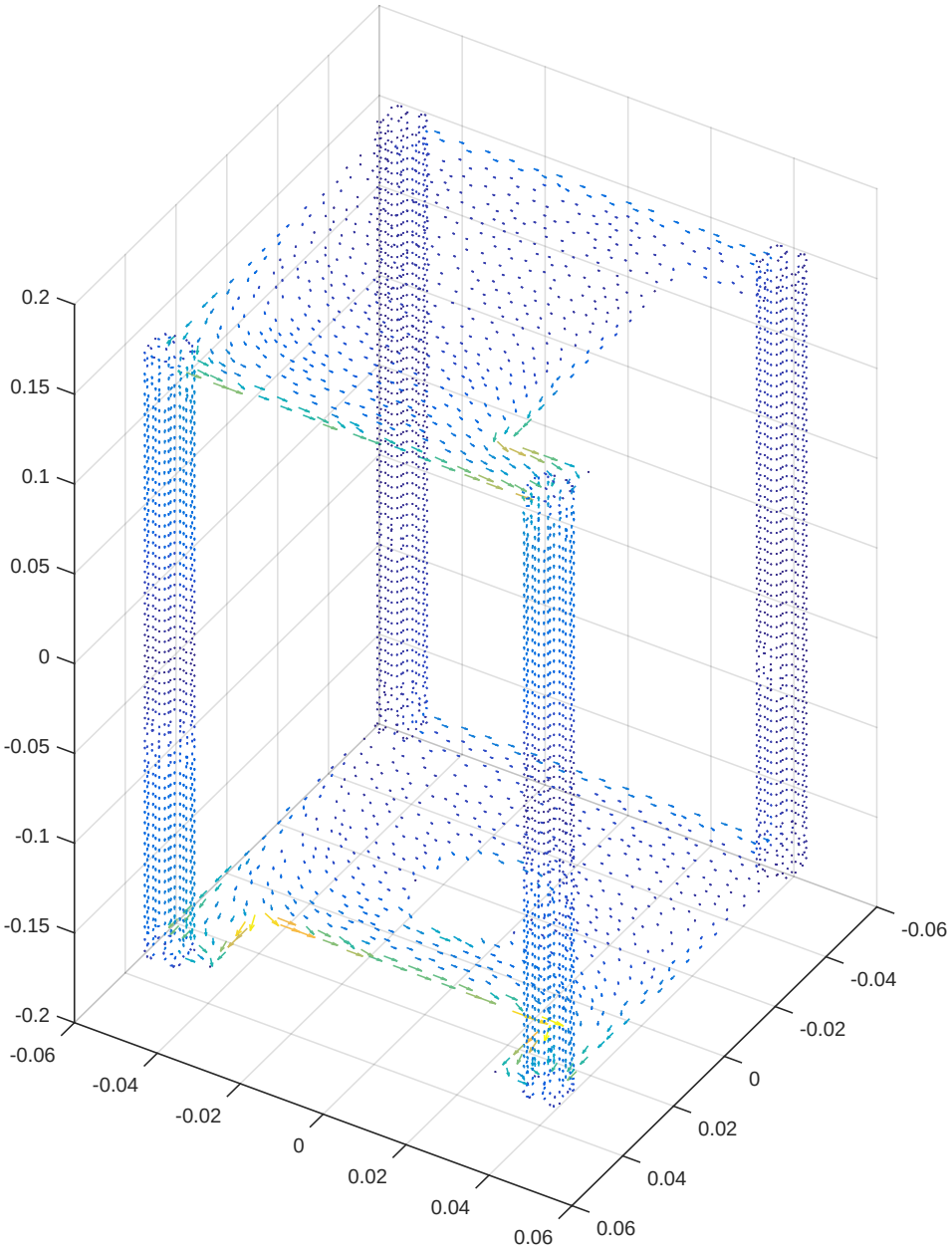

Figure 5.6: Surface current corresponding to optimized far field

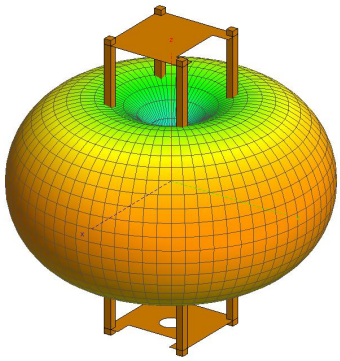

(a) Mode 1

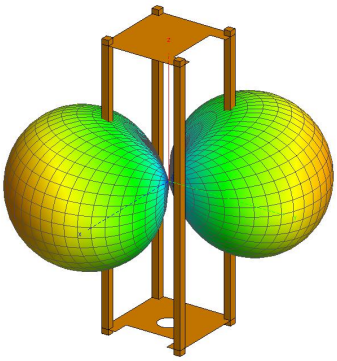

(b) Mode 2

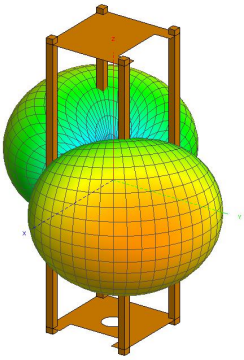

(c) Mode 3

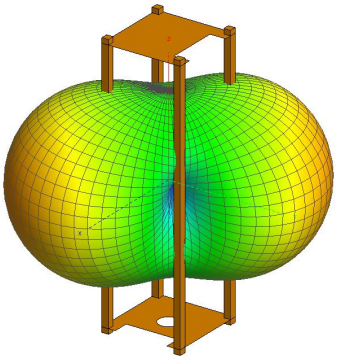

(d) Mode 4

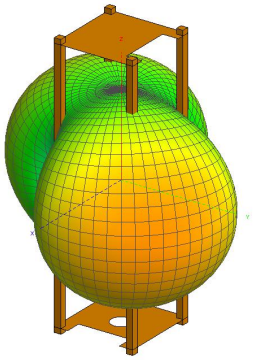

(e) Mode 5

Figure 5.7: Modal far fields for 3U CubeSat at 435 MHz

technique could specify circular versus linear polarization, the technique here will only specify the overall power and not the orientation. Traditionally satellite based communication systems use circular polarization to combat the Faraday effect [75]. Linearly polarized antennas will rotate their polarization vector as the signal travels through the atmosphere. To collect the signal at all times, the receiver should be circularly polarized to ensure reception at all times. This unfortunately will lead to a 3 dB loss at all times. Ice crystals and rain can also depolarize the signal as it travels through the atmosphere [75]. The system designer must make a decision about whether the increased gain compensates for the depolarization effects and the polarization mismatch loss of 3 dB.

The resulting modal weighting coefficients for the first five modes are 0.0089+j0.0099, -0.0221+j0.2954, 0.3449+j0.0558, 0.0675-j0.5198, and -0.4930-j0.0794. The main point is that the first mode is not a desirable contributor for this antenna. All the other modes have approximately the same magnitude. Based on the goal function over the lower hemisphere, Figure 5.8 shows the resulting far field from the optimization. Unlike the far field for 400 MHz, the total radiation pattern is close to omnidirectional. The far field is also very different from the goal radiation pattern over the lower hemisphere. The power of the synthesis method shows the best that is achievable using the structure so that extra effort is not spent trying to create a pattern that the structure will not support. Figure 5.9 shows the surface current resulting from this method.

For the higher 435 MHz band, the current on the $-\hat{y}$ side of the top plate has the highest current. The bottom plate also has high current at the corner in the -x,-y quadrant. There are more high current spots spread along the bottom plate and the top plate compared to the lower frequency. For both 400 MHz and 435 MHz most of the current is confined to the rectangular plates and only low current is found on the poles connecting the two plates.

There is one more frequency and goal pattern to consider. At 915 MHz, the structure should radiate in an omnidirectional pattern in the x-y plane. Going back to the previous characteristic mode analysis, 13 modes have a modal significance above 0.1 at 915 MHz on the structure. 915 MHz has many modes because the structure is starting to get large compared to a wavelength. For 400 MHz and 435 MHz, the distance from the center of the structure and the farthest point is between 0.235λ and 0.26λ limiting the

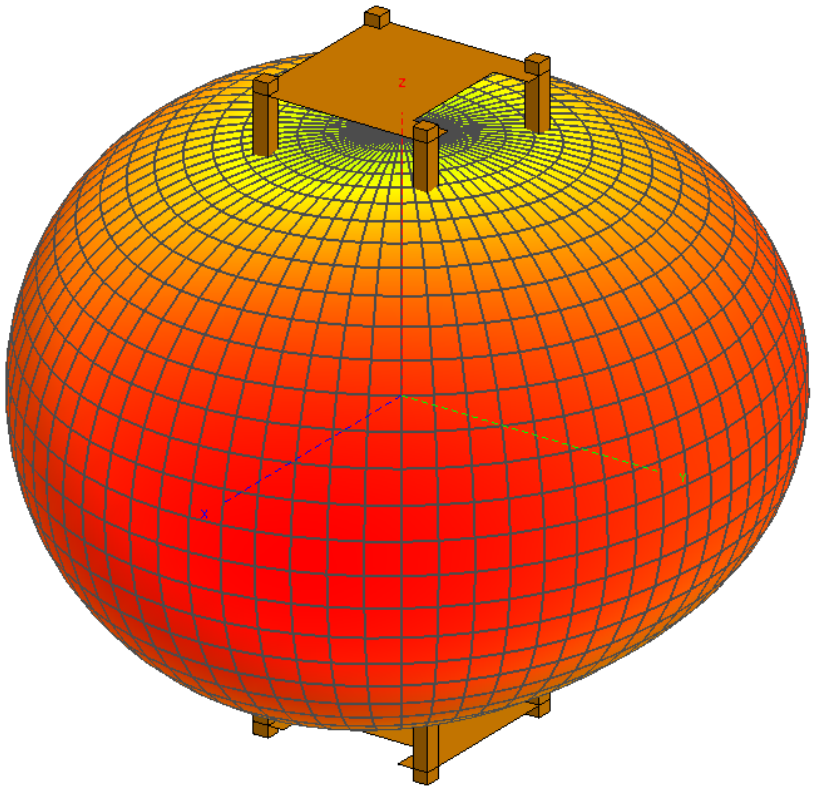

Figure 5.8: Optimized far field at 435 MHz

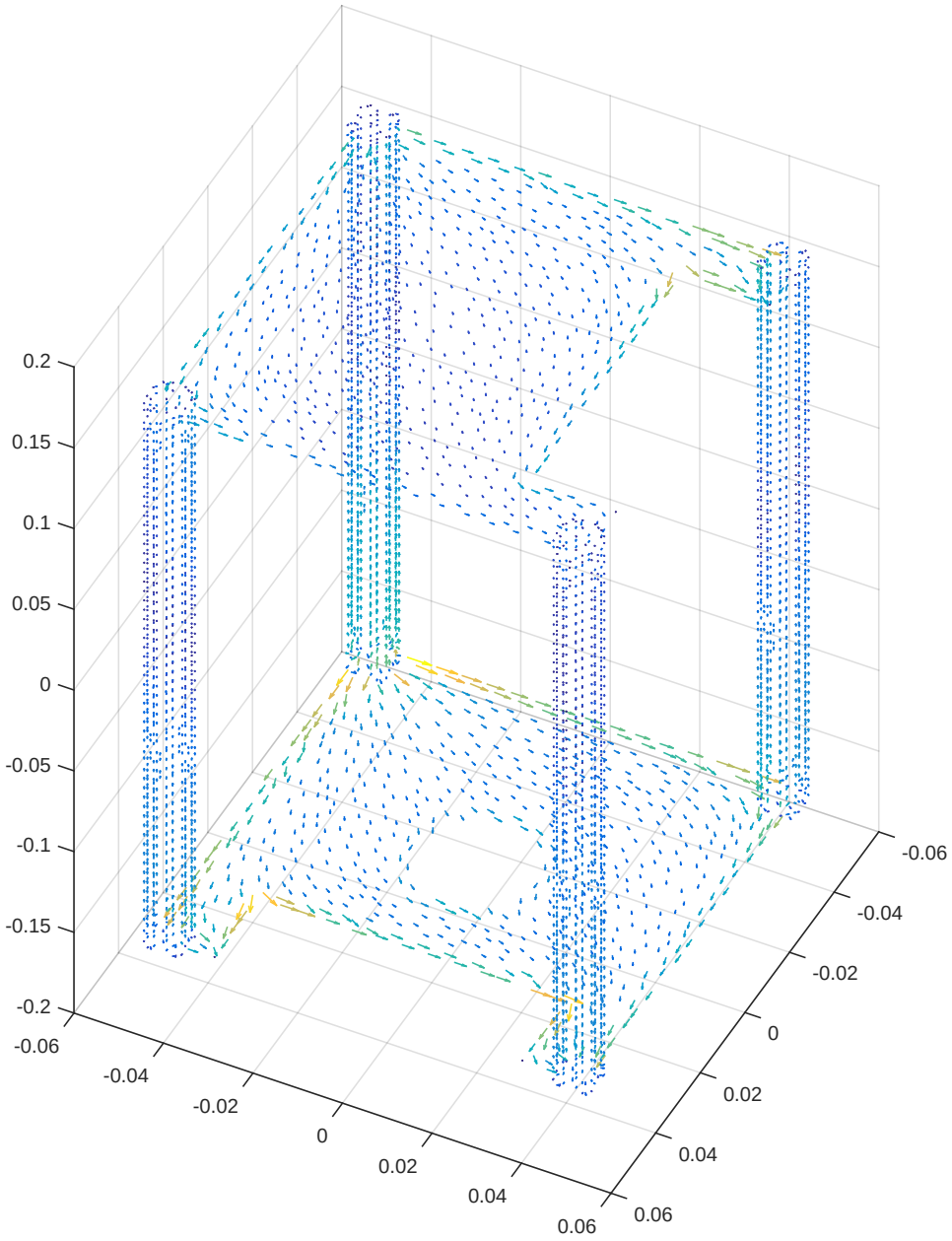

Figure 5.9: Surface current corresponding to optimized far field

number of modes that are relevant to this analysis. At 915 MHz, the first two modes are close to resonant and the remaining modes above 0.1 are also below 0.5. This hints that it may be simpler to excite the first or second modes versus the remaining modes on the structure. The eigenvalues for the first six modes are 0.1433, 0.1546, -1.8318, -1.8640, 1.882, and 1.997. The magnitude continues to increase as the modal index goes up.

Figure 5.10 shows the modal far fields associated with the first six modes on the structure. Beyond the first two modes, the other modal far fields pictured have many nulls in a variety of places. The large number of nulls persists as the mode number increases. For that reason the rest of the significant modes are not included in this discussion. The far field corresponding to the second mode is omnidirectional in the x-y plane corresponding to the goal pattern. Because the goal pattern is the second modal far field, the goal surface current is the surface current associated with the second mode. If the goal was to use only one feed, the method from Chapter 3 could be used to find the desired feed position. Figure 5.11 shows where the feed would go if one were only going to use one feed. Each mesh element that is part of the feed area is outlined in red.

The surface current associated with the second mode is shown in Figure 5.12. The surface current is strong at the center of each of the posts. All the current on the posts are in phase with each other to facilitate the generation of an omnidirectional pattern. From a single feed, it would have to create strong current at the center of each post and create equal in phase excitations on each post. 400 MHz and 435 MHz mainly utilize the rectangular plates while 915 MHz surface current mainly utilizes the posts.

Viewing the surface currents for each frequency leads to the design possibilities for the antenna elements. When the feed is placed on the structure, strong currents will be generated near the feed input. For that reason, the antennas should be fed at the frequency of interest near where the current is maximized. For 400 MHz, the largest current is on the bottom rectangular plate near the corners of the rectangular cutout. For this reason the feed will be placed at the corner of the cutout that is also below the cutout on the top rectangular plate, corresponding to the cutout with its position corresponding to positive values for x and y. The guiding principle for the design of each element is to have the element run parallel to the high current path on the structure. The current at 400 MHz seems to circulate around the bottom

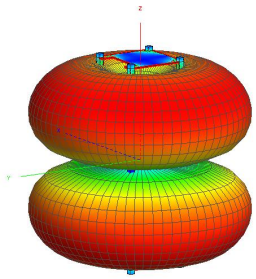

(a) Mode 1

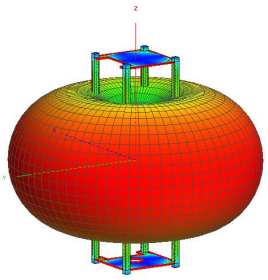

(b) Mode 2

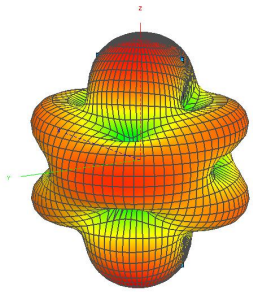

(c) Mode 3

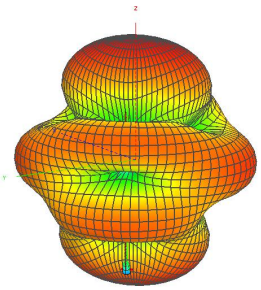

(d) Mode 4

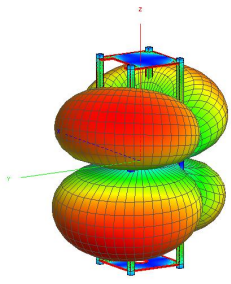

(e) Mode 5

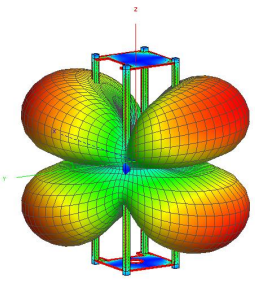

(f) Mode 6

Figure 5.10: Modal far fields for 3U CubeSat at 915 MHz

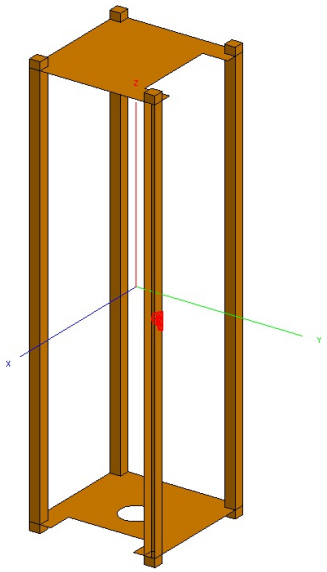

Figure 5.11: Feed Area for 915 MHz band

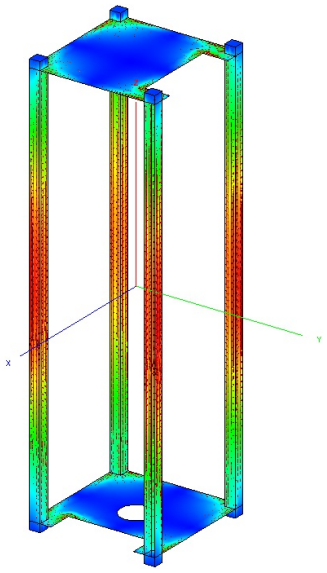

Figure 5.12: Desired surface current for 915 MHz band

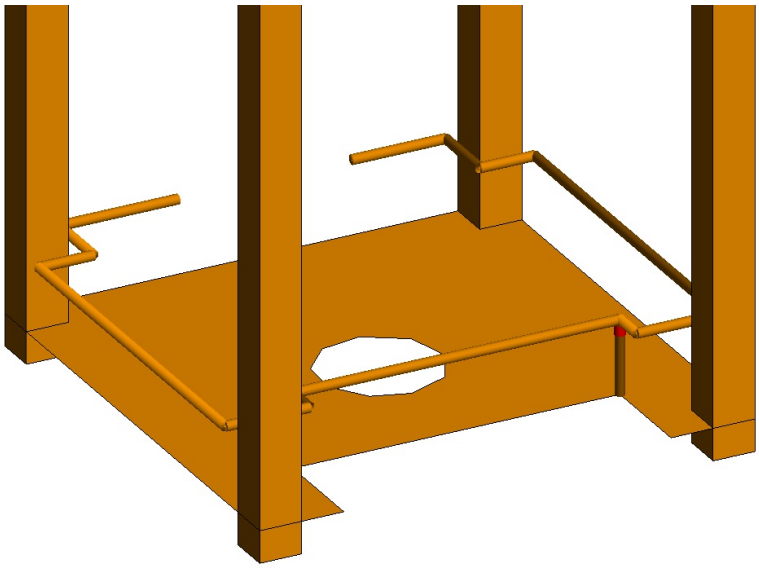

Figure 5.13: Element for 400 MHz band

rectangular plate. The element is designed to create circulating current. The element for 400 MHz goes from the feed and wraps around each side of the structure. The design of the element at 400 MHz installed on the structure is shown in Figure 5.13. The element is added to the CubeSat structure and simulated using FEKO®.

The 400 MHz element creates the appropriate surface current and generates the far field pattern shown in Figure 5.14. The far field has nulls in the same places as the desired goal pattern and has the same polarization. Additionally the design ensures the VSWR at 400 MHz is below 2. With the VSWR being below 2, the design is well-matched to a 50 Ω load. The gain is relatively still low in the desired direction; however, it is consistent with the optimized pattern. If one could put an antenna outside of the platform, the gain in the desired direction would be better. Much of the gain is lost because of the constraint for the CubeSat that the elements must be inside of the platform.

Now that the lowest band is complete, the next step is to look at the 435 MHz band. For the middle band, there is strong current on both the top and bottom rectangular plates. For this it is important to develop an excitation that will excite surface current on both the top and bottom plates without significantly disturbing the currents required for the low or high frequency bands. Because the high band has symmetry about the posts near the center

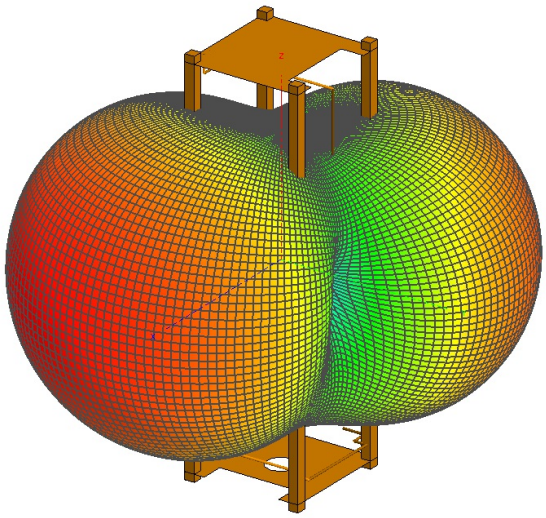

Figure 5.14: Total simulated far field for 400 MHz band

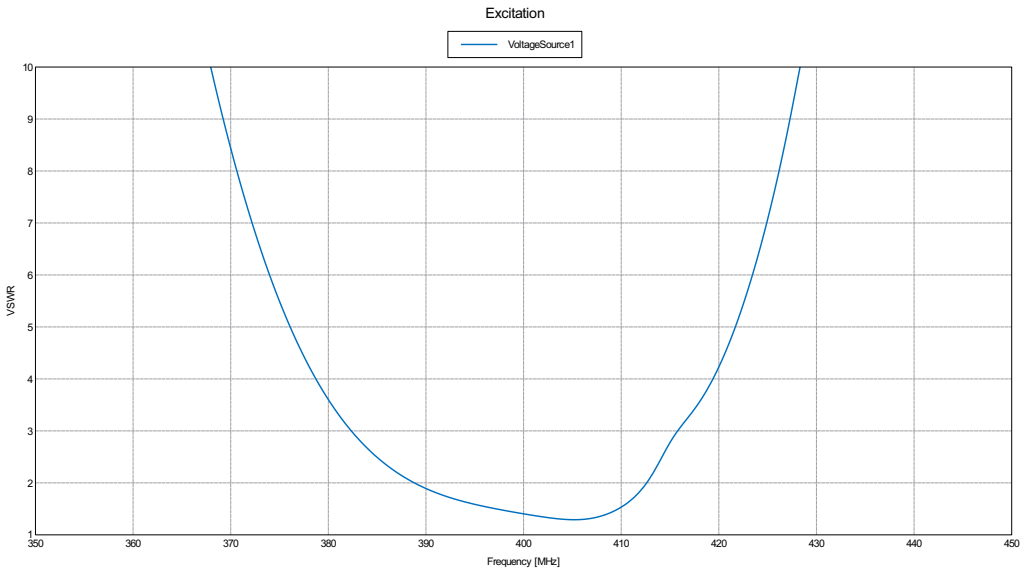

Figure 5.15: Simulated VSWR for 400 MHz band

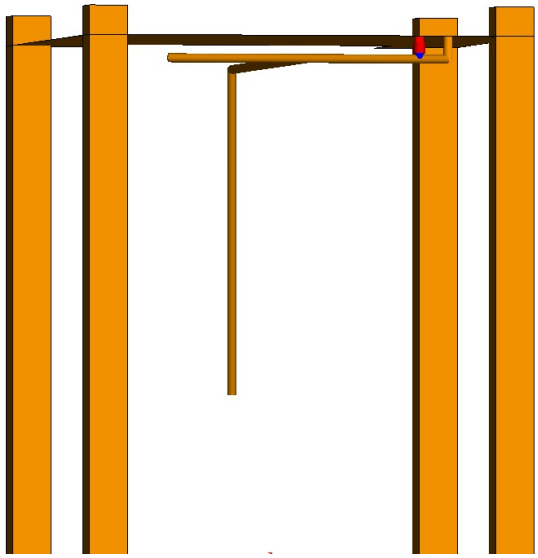

Figure 5.16: Element for 435 MHz band

of the structure, it is important to preserve the symmetry in the posts. The designer does not want to add any additional posts or connections between the top and bottom to ensure that it is possible to achieve the required surface current for the 915 MHz band. The far field for 435 MHz is approximately omnidirectional so the element should make it possible to create that current. The element also needs to radiate and excite the bottom rectangular plate. Figure 5.16 shows the designed element for 435 MHz. The part of the element underneath the cutout in the top rectangular plate radiates and excites the bottom plate. The element is very narrowband but is matched at 435 MHz as seen in Figure 5.18. The resulting far field is shown in Figure 5.17.

After designing and installing the 435 MHz element, the next step is to check the 400 MHz element. Because the elements are physically separated and most of the high current areas for one element are in the areas of low current for the other element, there are no large effects to the 400 MHz band from the addition of the 435 MHz band. Because there is little impact it is possible to continue and design the element for the 915 MHz antenna element.

As stated previously, each post has a maximum at the center and they are in phase with one another. These current maximums that are in phase create an overall omnidirectional pattern. While it is possible to create this pattern from one feed, it is much simpler to use four feeds. If there is only

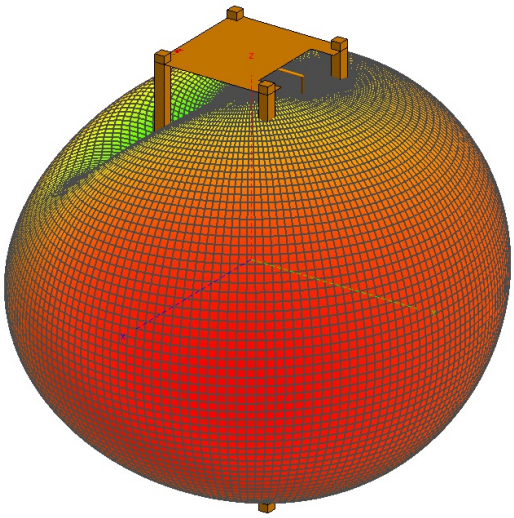

Figure 5.17: Total simulated far field for 435 MHz band

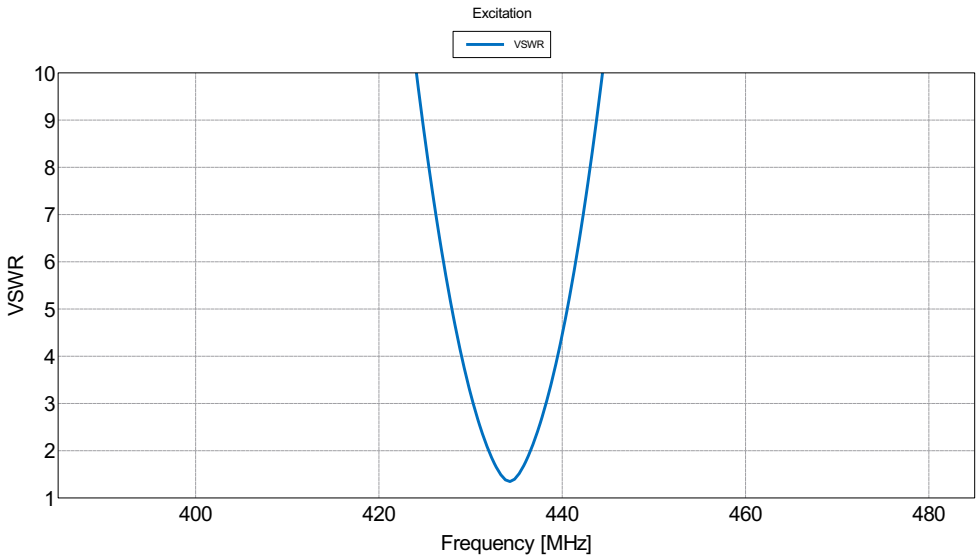

Figure 5.18: Simulated VSWR for 435 MHz band

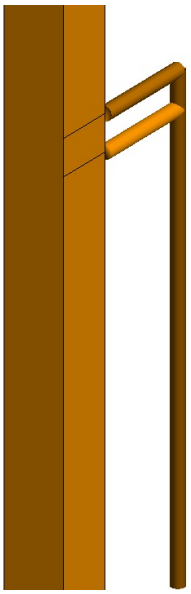

Figure 5.19: One element for 915 MHz band

one input to the electronics, a splitter or combiner can be used to achieve the same impact. An inverted-f antenna (IFA) is used on each post to excite one quadrant. Because the antennas are in phase, the element patterns installed on the platform should add up constructively to create the desired omnidirectional pattern. Figure 5.19 shows one IFA element designed for this antenna. Together the four IFAs combine their far fields to produce the far field shown in Figure 5.20. This far field is close to identical to the goal far field from the characteristic mode analysis. The IFAs are fed at the high current point on the structure with identical excitations. Each IFA is matched to 50 Ω as shown in Figure 5.21.

Because the high current for the 915 MHz band is near the center of the posts compared to the other bands which have their high current spots on the rectangular plates, the lower bands should remain largely unchanged. Looking at the lower bands, this is true and thus the antenna has been successfully designed for all three bands and performs with the desired far field patterns. The surface current for each frequency of interest are shown in Figure 5.22. The surface currents are close to the ones determined to be optimal and the matching far field patterns confirm that. The final designed antenna is shown in Figure 5.23 and the built implementation is shown in Figure 5.24.

The built antenna was tested and at each band the VSWR was within

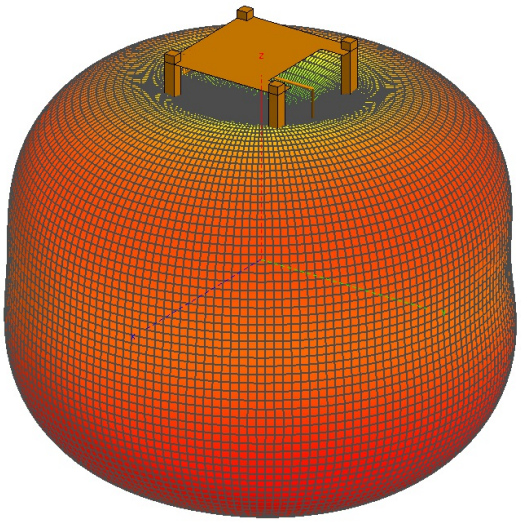

Figure 5.20: Total simulated far field for 915 MHz band

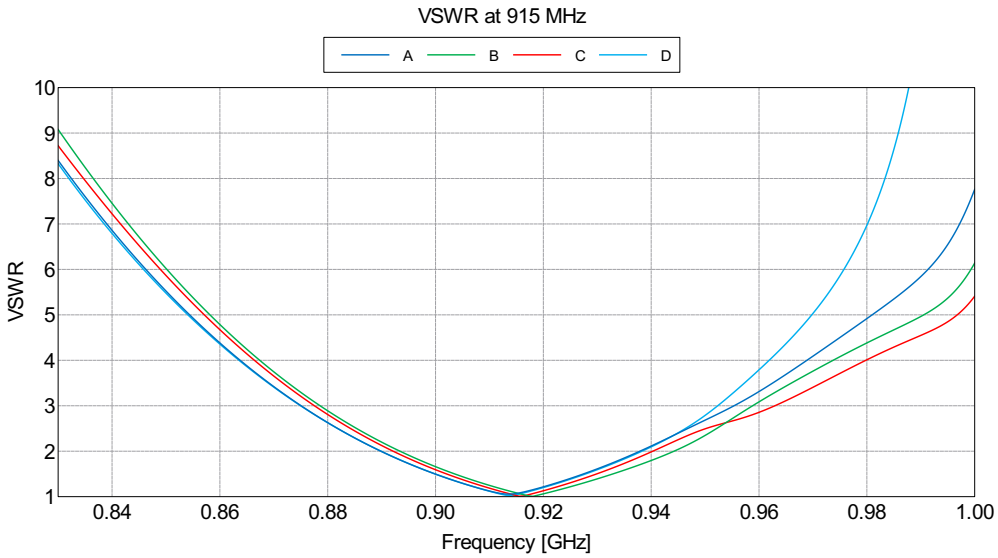

Figure 5.21: Simulated VSWR for 915 MHz band

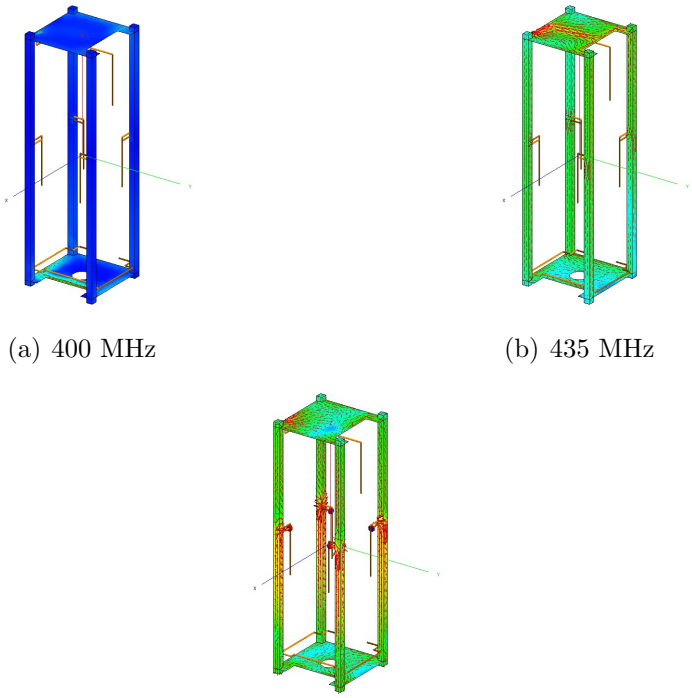

(a) 400 MHz

(b) 435 MHz

(c) 915 MHz

Figure 5.22: Surface current for the CubeSat at each frequency

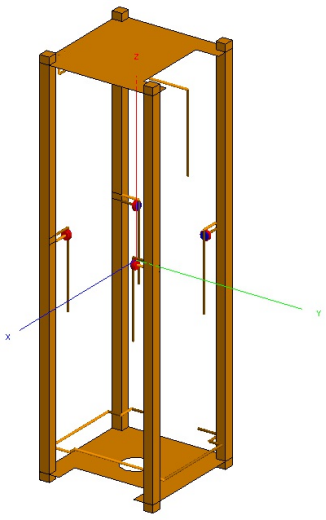

Figure 5.23: Final simulated antenna with all antenna elements installed

Figure 5.24: Antenna built to ensure simulation accuracy

2:1 for the bands of interest. While testing the pattern for one band and input, all other inputs were terminated with a 50 Ω load. For each antenna two pattern cuts were taken using both horizontal and vertical polarizations. Because there was no combiner available at the frequency of interest, all the IFAs for the 915 MHz band were measured separately and compared to the results for each element. The results largely match excepting angles near the cable.

For the 400 MHz antenna, the goal pattern attempted to guarantee that as much power reached the ground station as possible. Figure 5.25 examines the gain at ϕ equal to zero as θ changes. From 0 to 180 degrees the measurements match simulation within 3 dB and follow the same shape. Much of the gain difference can be that the simulation is done using PEC instead of copper with an actual thickness. Along the negative θ portion of the pattern there is slightly more deviation from the pattern. This is due to the direction of the cable during the measurement negatively affecting the radiation pattern. Figure 5.26 shows the comparison between the patterns as the CubeSat is rotated in ϕ at the x-y plane. The cross-polarization is lower than the co-polarization just like in simulation. Although difficult to see from this picture, the simulation and measurements have nulls in the same place for the E_ϕ measurements. The nulls for the simulation are much deeper than those from

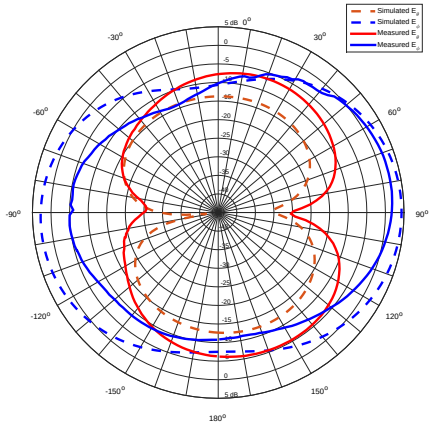

Figure 5.25: Gain comparison at different θ values at 400 MHz

the measurement. This could be due to cable radiation in some portions and the fact that the chamber cannot reliably measure below a certain threshold.

The 435 MHz element is measured in a similar fashion. Figure 5.27 shows the gain comparison between measurement and simulation when looking at various values of θ at ϕ equal to zero. The E_θ simulation and measurement track pretty closely together. The E_ϕ measurements are slightly stronger than predicted near θ equal zero. This is due to the connector placement forcing the cable direction. The cable is coming off the CubeSat directly at θ equal to zero creating a slight increase in gain in that direction. Figure 5.28 compares the gain between simulation and measurement in the x-y plane. These two measurements match almost exactly what was predicted by the simulation. The measured null is slightly deeper than it was predicted to be in E_ϕ but the measurements are extremely close to the simulated far field patterns.

The last measurement to validate is for the pattern at 915 MHz. Unfortunately there was no combiner to test the pattern of all four antennas working simultaneously. Each IFA was tested individually and compared to the simulated individual pattern. The pattern for each IFA in the x-y plane is shown in Figure 5.29.

With each individual measurement matching so closely, the combined pat-

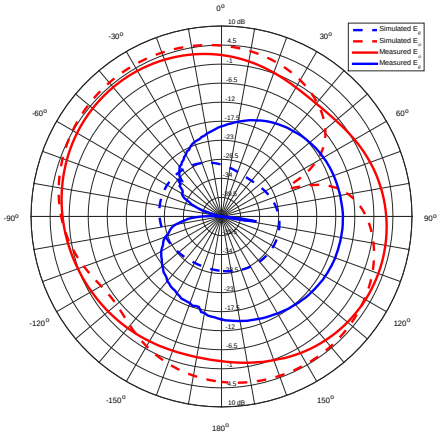

Figure 5.26: Gain comparison at different ϕ values at 400 MHz

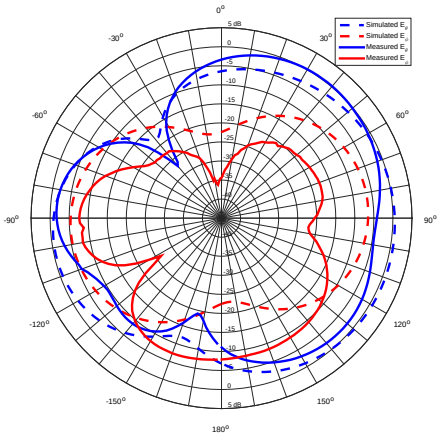

Figure 5.27: Gain comparison at different θ values at 435 MHz

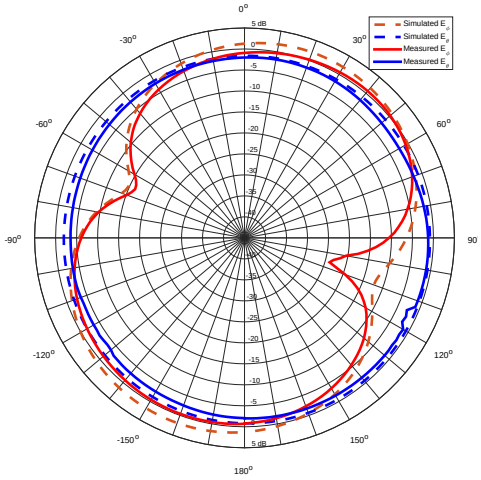

Figure 5.28: Gain comparison at different ϕ values at 435 MHz

terns should also closely match the simulated combined pattern. The pattern for IFA B is off slightly more than the other IFAs but this is due to the placement of the cable. For IFA A the cable is directed toward ϕ equal to -35 degrees. There are slight deviations in signal near the -35 degree point from the angle of the cable. IFA B when measured had a cable placement around 60 degrees. The additional null in that direction for IFA B is due to the cable blockage. IFA C's cable is placed near the 150 degree mark, causing a slight shift in the null. Because the simulation calls for a null near 150° regardless, the cable radiation has little impact on the gain of the pattern in that direction. IFA D's cabling was in the -125° direction. For that reason there is a slight null near -125° but the null that should be at -105° is less pronounced than expected. The cable radiation has some slight impacts on the pattern but overall the patterns do closely correspond to what is expected at these frequencies.

These antennas were measured using a 50 Ω system and the ports not being measured were terminated with 50 Ω loads. The antenna performance with different load conditions was not tested and is part of the future work. The port to port isolation was also not measured for these antennas.

The measurement results verify the synthesis method for installing multiple antennas on a single platform when the goal is to create particular

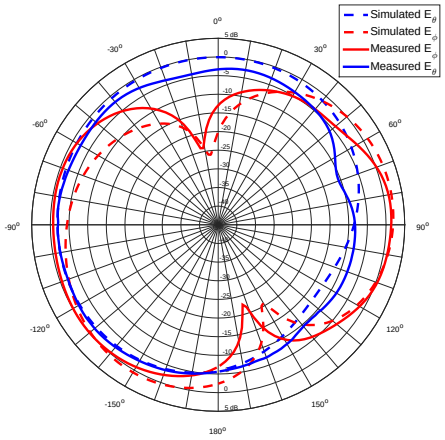

(a) Gain comparison for IFA A

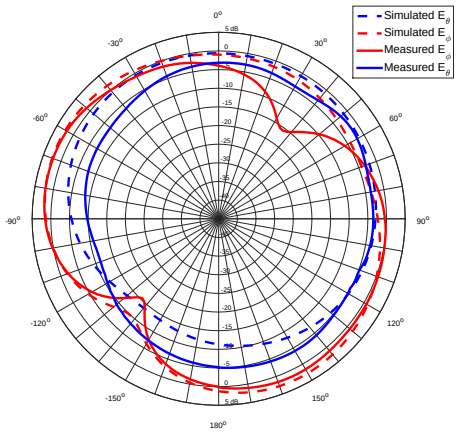

(b) Gain comparison for IFA B

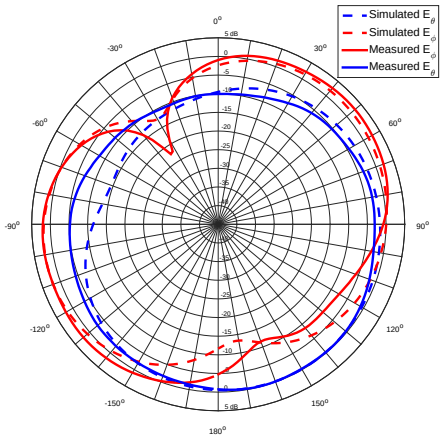

(c) Gain comparison for IFA C

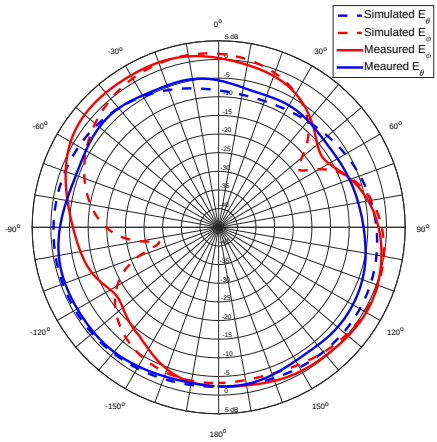

(d) Gain comparison for IFA D

Figure 5.29: Individual radiation pattern for each IFA

radiation patterns. The method finds the radiation pattern closest to the goal pattern that is achievable based on the platform for installation. From the goal pattern, the corresponding surface current can be calculated. Using the surface current, elements can be designed and installed on the structure starting at the lowest frequency and working toward the higher frequencies of interest. Most previous methods rely on installing pre-designed elements on a platform and attempting to mitigate the impact of mutual coupling. This method starts by evaluating the radiation of the platform and using that to design isolated elements that have the desired radiation pattern when they are installed on the structure of interest. The CubeSat example provided demonstrates how the method works in practice and verifies that the simulated antenna's performance.

There are some clear deficiencies to the model of the CubeSat platform. The platform does not have any of the additional electronics or instrumentation that would be required to make the CubeSat able to fly. The next chapter examines the impact of changing the platform to models that more accurately depict the true CubeSat platform implementation. The goal is to investigate the role of platform model fidelity in using this synthesis method.

CHAPTER 6

PLATFORM MODEL FIDELITY

The previous chapter detailed a novel synthesis method for designing multiple antennas for installation on a platform when the desire is to create a set of specific radiation patterns. The method used a characteristic mode analysis on the platform to assist in determining ideal antenna element designs and locations. The model used for the platform in the example was overly simplistic to make it easier to model and find solutions. The goal of this chapter is to research the impact of increasing model fidelity on the modal far fields and discuss how that impacts the resulting designs and radiation patterns.

In the previous section the example used a CubeSat chassis to verify the synthesis method. The modeled platform, shown in Figure 5.1, is highly simplistic. The inside of the platform is empty and does not account for electronics or instrumentation that would be necessary to make the CubeSat function. While the antenna element designs attempted to stay within the confines of CubeSat regulations, the example did not take into account the additional panels/electronics that would likely be contained inside the CubeSat. In this section, two different approximations to the CubeSat platform will be identified. A characteristic mode analysis will be performed on both structures. The modal far fields will be compared to gain insight into how the mode structure changes as the platform is altered and the impact on the results when one has a platform that varies from the exact modeling scenario.

The first comparison platform for this chapter will use a PEC box to approximate the additional electronics inside the CubeSat. Figure 6.1 shows the platform modeled for this analysis. The CubeSat frame has the same size and dimensions as in the previous chapter. The only difference is the large box added to the inside of the chassis. The box is not connected in any way to the original chassis. This platform will be referred to as the 'CubeSat with box.'

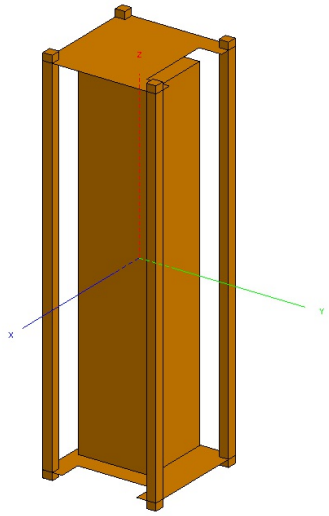

Figure 6.1: CubeSat with PEC box approximation for internal electronics

The second platform for comparison assumes that the internal electronics are mainly on printed circuit cards that can be approximated by sheets of perfect electric conductor. The cards are spaced at random heights and spacings throughout the CubeSat platform. Much like the first comparison platform, the goal is to capture the impact of adding electronics or other materials inside the platform. This platform is shown in figure 6.2 and it will be referred to as the 'CubeSat with slats.' The slats, like the box, are not connected to the original chassis at any point. For reference, Figure 6.3 shows the original CubeSat with no box or slats.

Much like in the previous chapters, the first step is to solve for the characteristic modes on both platforms at the three frequencies of interest and compare the eigenvalues and the modal far fields. The CubeSat with box platform has three eigenvalues that correspond to a modal significance above 0.1. The three eigenvalues are 0.058, 0.329, and 1.502. These are comparable in scale and number to the platform on its own. Figure 6.4 shows the modal far fields associated with the first three modes on the CubeSat with box platform.

The CubeSat with slats platform is analyzed in a similar manner. Similar to the other two platforms, this platform also has three eigenvalues that correspond to a modal significance greater than 0.1. The eigenvalues for the CubeSat with slats platform are 0.245, -8.492, and -8.505. These eigenvalues have a higher magnitude compared to the eigenvalues for both the original

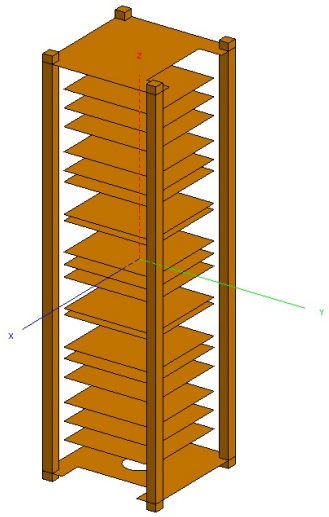

Figure 6.2: CubeSat with PEC cards approximation for internal electronics

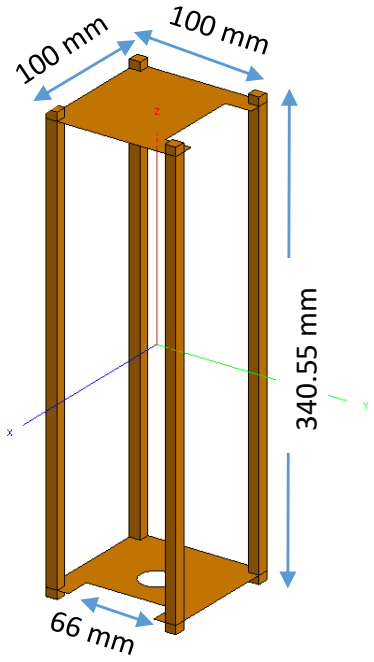

Figure 6.3: Original simulated 3U CubeSat structure

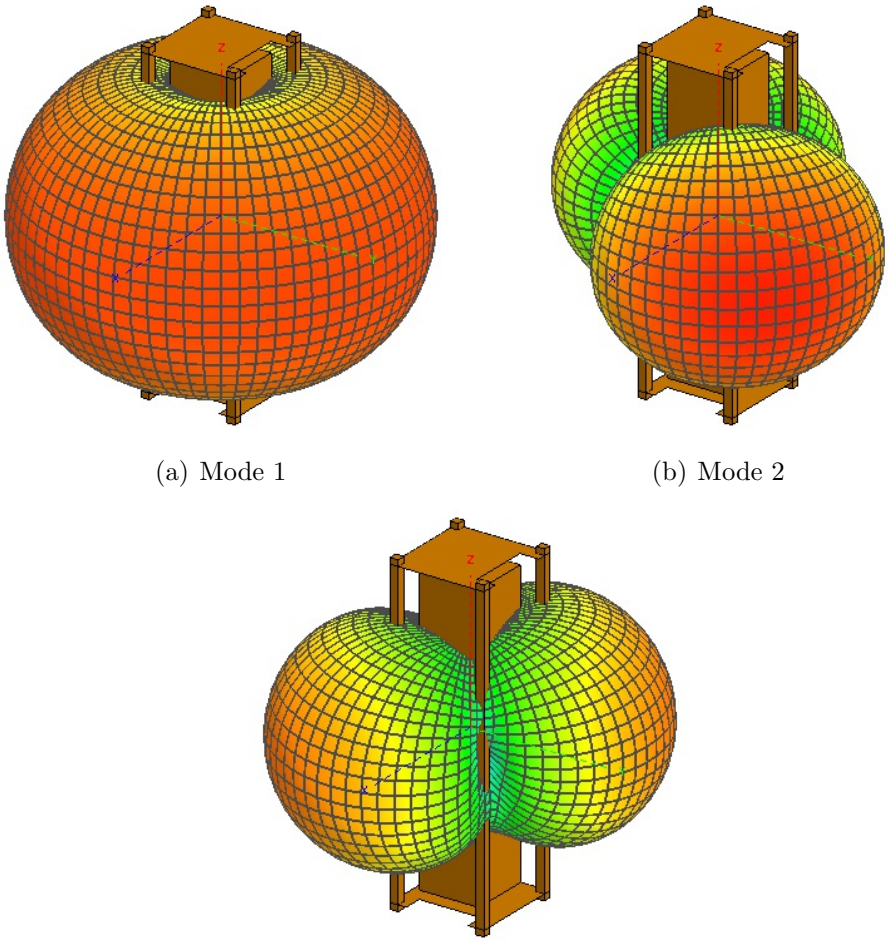

(a) Mode 1

(b) Mode 2

(c) Mode 3

Figure 6.4: Modal far fields for 3U CubeSat with PEC box at 400 MHz

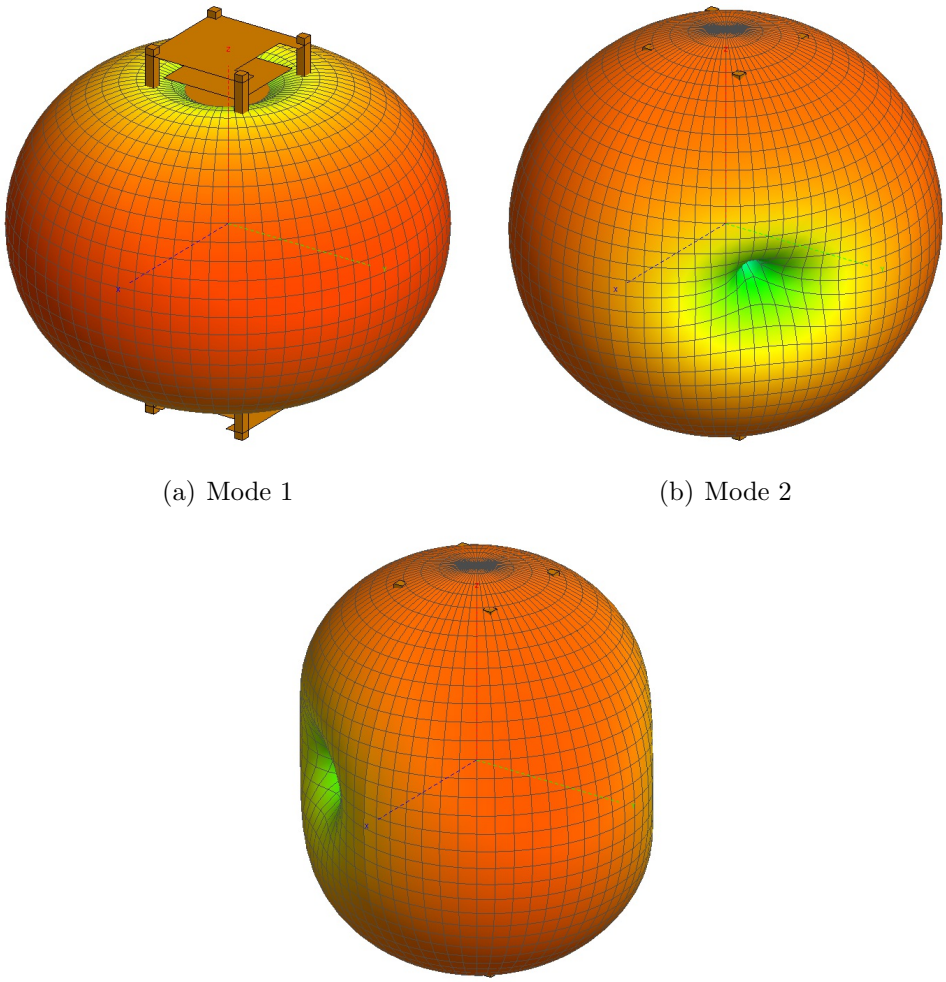

(a) Mode 1

(b) Mode 2

(c) Mode 3

Figure 6.5: Modal far fields for 3U CubeSat with slats at 400 MHz

CubeSat platform and the CubeSat with the PEC box. This shows that the modes on the platform are starting to change and deviate from the original design even without looking further into the modal far fields. Figure 6.5 shows the modal far fields for the first three modes on the CubeSat with slats. Figure 6.6 shows the modal far fields for the original CubeSat at 400 MHz.

While it is possible to compare the modal far fields linearly, there must be a way to quantitatively compare the modal far fields of the different platform structures. For the characteristic mode simulations, the modal far field is calculated for distinct points on the infinite sphere. If the simulations are chosen such that they all have the same location and number of points,

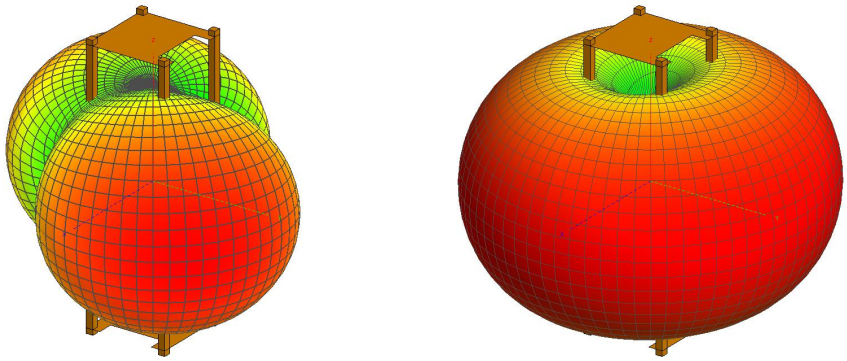

(a) Mode 1

(b) Mode 2

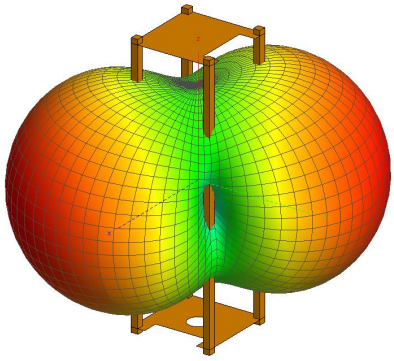

(c) Mode 3

Figure 6.6: Modal far fields for 3U CubeSat at 400 MHz

Table 6.1: Comparing modal far fields between the empty CubeSat and the CubeSat with box at 400 MHz

		CubeSat with Box		
		Mode 1	Mode 2	Mode 3
Empty CubeSat	Mode 1	248.97	2.23	323.79
	Mode 2	2.12	245.72	243.48
	Mode 3	249.99	324.36	1.96

it should be possible to quantify the difference in the total far field between different structures. The difference between modal far fields will be calculated as

$$E_j^m(i) - E_k^n(i) \tag{6.1}$$

where $E_j^m(i)$ is the modal electric field for the jth structure and the mth mode at the ith point. The metric, ψ to compare the difference will then be to use the sum over identical point spheres of the square of the difference as shown in Equation 6.2.

$$\psi = \sum_i \left(|E_j^m(i)| - |E_k^n(i)|\right)^2 \tag{6.2}$$

To better compare the simulations, the maximum power at any point on a modal far field is normalized to one and then the differences are calculated between all pairs of relevant modes for each of the three structures. Each simulation uses the same sphere with 2701 points. The points are spaced by 5 degrees in both θ and ϕ. Two modal far fields are considered the same if they have an average difference of less than 10% of the maximum power. Because this simulation has 2701 points and each pattern has a maximum at any given point of 1, the modal far fields are similar when ψ is less than or equal to 27.01. Once ψ is above 27.01, the modes are no longer considered similar. Tables 6.1, 6.2, and 6.3 show ψ for all the different combinations of structures and modes. The modal far fields that are similar are highlighted in yellow.

As the platform model deviates further from the original model, it seems that fewer modes correlate with the original modes. When comparing the empty CubeSat to the CubeSat with the box, each of the first three modal far fields is still present they are just in a slightly different order. When the

Table 6.2: Comparing modal far fields between the empty CubeSat and the CubeSat with slats at 400 MHz

		CubeSat with Slats		
		Mode 1	Mode 2	Mode 3
Empty CubeSat	Mode 1	245.69	937.41	700.03
	Mode 2	1.63	689.92	694.41
	Mode 3	246.05	702.14	941.73

Table 6.3: Comparing modal far fields between the CubeSat with slats and the CubeSat with box at 400 MHz

		CubeSat with Slats		
		Mode 1	Mode 2	Mode 3
CubeSat with Box	Mode 1	0.07	699.04	699.54
	Mode 2	258.43	979.75	736.52
	Mode 3	252.18	773.01	1011.72

empty CubeSat is compared to the CubeSat with slats, the first mode for the CubeSat with slats matches the empty CubeSat but they have no other modes in common. As the model complexity increases, the modes based on the larger features remain while many of the higher order modes begin to change.

The analysis is then performed on the same structures at 435 MHz. The original structure had five eigenvalues with a corresponding modal significance above 0.1. The CubeSat with a box also has five appropriate eigenvalues. The eigenvalues are 0.18, 6.02, 7.01, 8.36, and 8.43. This compares to the original structure with values of 0.33, 2.13, 2.50, 9.12, and 9.17. The CubeSat with the slats has eigenvalues of 0.33, -6.51, -6.52, 9.34, and 9.35. All the CubeSat structures have the same number of viable modes but the values vary. The CubeSat with slats has some negative eigenvalues showing that it stores its energy differently than the other structures. Similar to at 400 MHz, the modal far fields are compared. Figures 6.7 and 6.8 show the first five modal far fields.

Examining the modal far fields and comparing them to Figure 6.9, it seems as if the CubeSat with the box matches the modal far fields of the original quite closely. The CubeSat with slats do not seem to have the same modal far fields for modes 2 and 3, consistent with the difference in the eigenvalues for modes 2 and 3. ψ can be used to see if these results hold quantitatively.

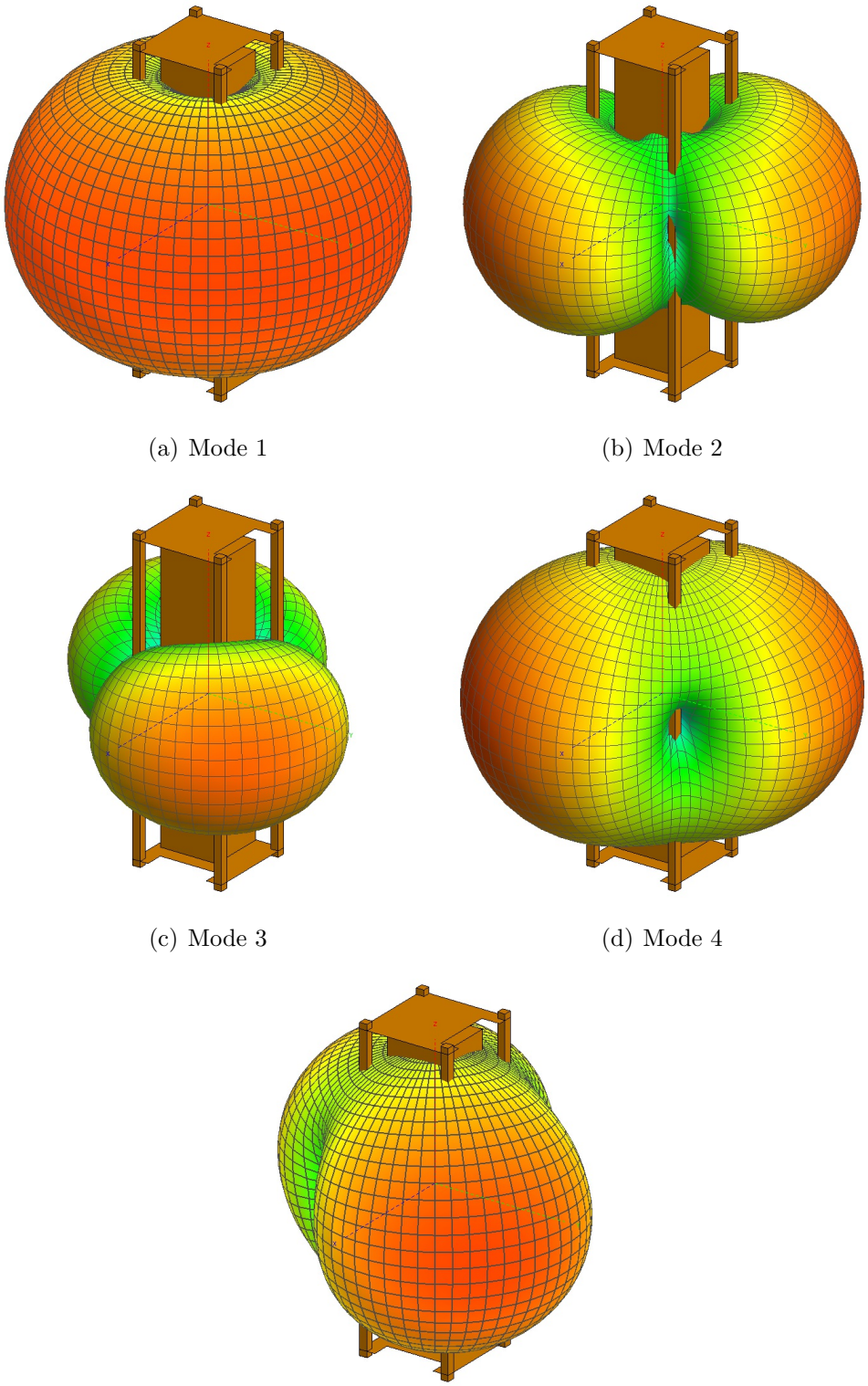

(a) Mode 1

(b) Mode 2

(c) Mode 3

(d) Mode 4

(e) Mode 5

Figure 6.7: Modal far fields for 3U CubeSat with box at 435 MHz

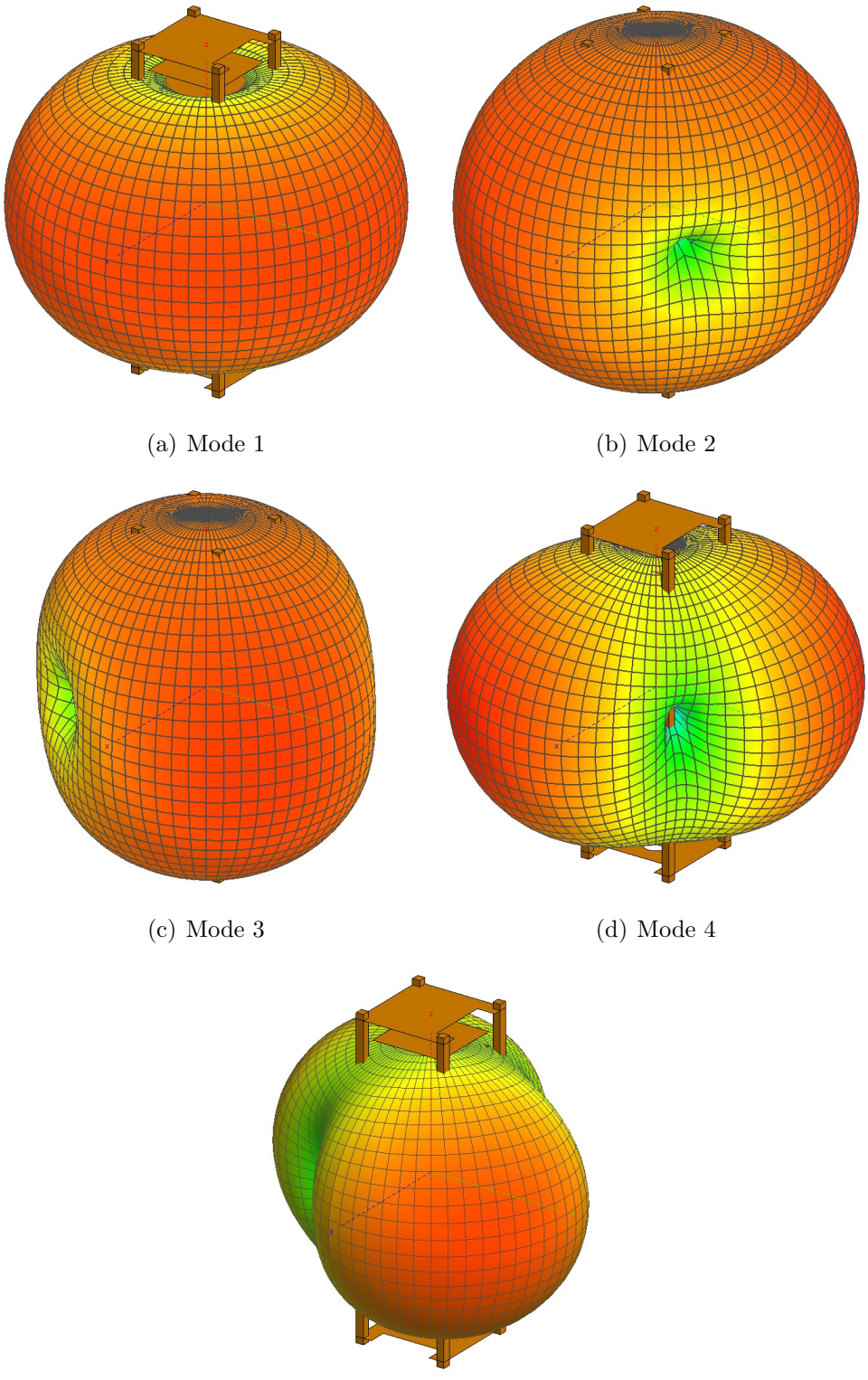

(a) Mode 1

(b) Mode 2

(c) Mode 3

(d) Mode 4

(e) Mode 5

Figure 6.8: Modal far fields for 3U CubeSat with slats at 435 MHz

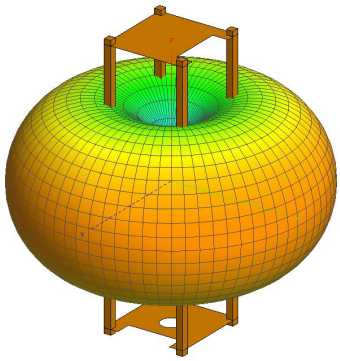

(a) Mode 1

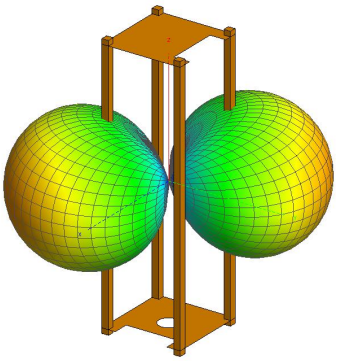

(b) Mode 2

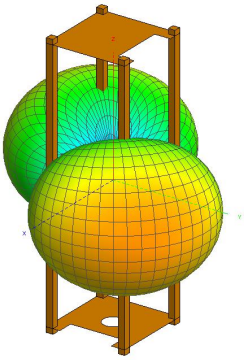

(c) Mode 3

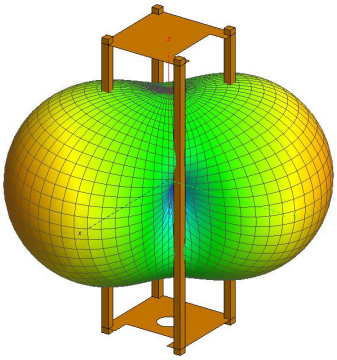

(d) Mode 4

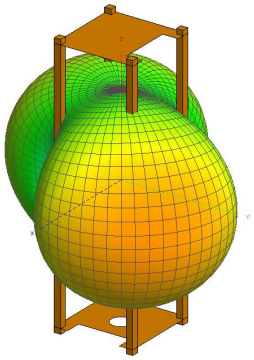

(e) Mode 5

Figure 6.9: Modal far fields for 3U CubeSat at 435 MHz

Table 6.4: Comparing modal far fields between the empty CubeSat and the CubeSat with box at 435 MHz

		CubeSat with Box				
		Mode 1	Mode 2	Mode 3	Mode 4	Mode 5
Empty CubeSat	Mode 1	0.06	285.10	279.09	243.59	246.46
	Mode 2	296.46	0.27	330.45	163.31	476.21
	Mode 3	297.92	332.98	1.115	469.60	173.86
	Mode 4	239.38	145.21	433.69	0.53	280.12
	Mode 5	240.74	451.32	138.20	281.19	0.65

Table 6.5: Comparing modal far fields between the empty CubeSat and the CubeSat with slats at 435 MHz

		CubeSat with Slats				
		Mode 1	Mode 2	Mode 3	Mode 4	Mode 5
Empty CubeSat	Mode 1	0.003	440.76	443.21	230.16	230.24
	Mode 2	291.45	557.61	815.51	140.16	441.99
	Mode 3	292.91	815.05	563.49	442.16	141.81
	Mode 4	239.01	126.67	365.97	1.36	278.81
	Mode 5	240.40	360.70	124.05	278.81	1.54

Using ψ, the first five modes of the empty CubeSat and the CubeSat with box do correspond to one another. The CubeSat with slats has modal far fields that correspond to those on the other two platforms for modes 1, 4, and 5. The values for ψ are shown in Tables 6.4, 6.5, and 6.6 with the correlated modal far fields highlighted in yellow as before.

Much like before, the more changes from the original structure, the less the modes start to resemble each other. The original first mode from the empty

Table 6.6: Comparing modal far fields between the CubeSat with box and the CubeSat with slats at 435 MHz

		CubeSat with Slats				
		Mode 1	Mode 2	Mode 3	Mode 4	Mode 5
CubeSat with Box	Mode 1	0.05	437.05	439.55	230.99	231.14
	Mode 2	285.36	538.49	794.47	130.75	429.65
	Mode 3	279.46	769.16	520.84	416.05	120.93
	Mode 4	243.82	119.55	362.29	1.18	281.85
	Mode 5	246.73	351.83	112.67	280.92	1.91

CubeSat is present in all three structures. The fourth and fifth modes are also present. The second and third modes are present in the CubeSat with the box but not the CubeSat with the slats. The changes in the platform are affecting some of the modes but not all of them. This is largely dependent upon how the mode radiates. The results are consistent with what can be observed by the differences in far field; however, it is not always practical to look at every modal far field.

The best example of where ψ can be used in lieu of visual comparison is at 915 MHz. For 915 MHz the original structure had 13 eigenvalues corresponding to a modal significance above 0.1. The CubeSat with box and the CubeSat with slats have 17 and 16 modes with small enough magnitudes to be considered, respectively. There are too many different combinations to do a visual comparison. The larger the number of eigenvalues, the more important it is to be able to compare the modal far fields without having to just use visual observation. At 915 MHz, the structures now have different numbers of important modes. This means that some modal far fields either will not correspond to others or should not be included in the synthesis method. This structure at 915 MHz shows the importance of using ψ to compare modal far fields.

To try and get some idea of the modal far fields, the first five modal far fields on the new structures will be shown in Figures 6.10 and 6.11. Even in the first five modes, these modal far fields have more nulls and differing lobe strengths making it significantly more difficult to compare by sight between those figures and Figure 6.12. Tables 6.7, 6.8, and 6.9 show ψ values comparing all the first 17 modal far fields from each structure.

The empty CubeSat and the CubeSat with the box have some corresponding modes. Modes 1, 2, 7, 8, 10, and 11 from the empty CubeSat correspond to modes 2, 1, 5, 6, 7, and 8 respectively in the CubeSat with the box. Once we compare the empty CubeSat to the CubeSat with slats, only modes 1 and 2 from the empty CubeSat correspond to modes 2 and 1. If the CubeSat with the box and the CubeSat with slats are compared, modes 1, 2, and 12 from the CubeSat with Box correspond to modes 1, 2, and 12 for the CubeSat with slats. The structure now has modes with many more nulls and they vary more significantly as the structure change. From the results at all three frequencies we can see that modes can change order or disappear as the structure changes. If an antenna designer is planning to use modes with

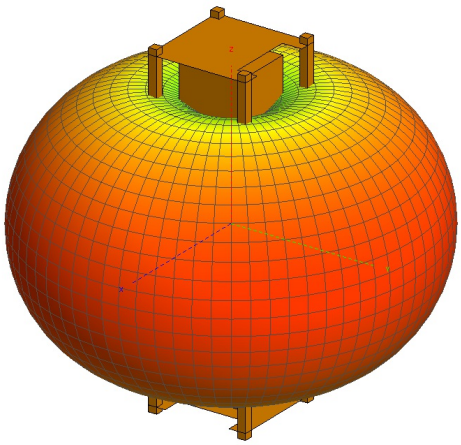

(a) Mode 1

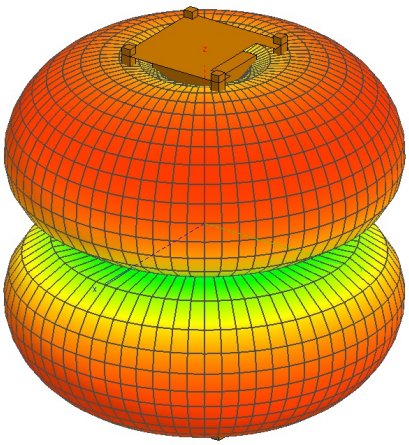

(b) Mode 2

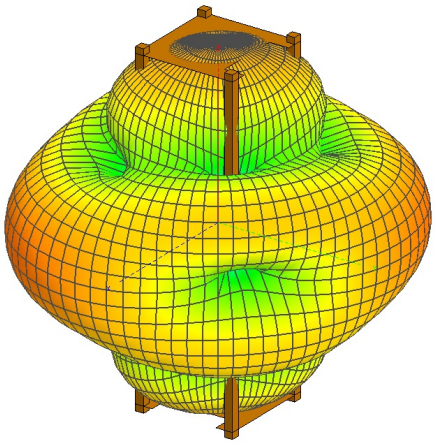

(c) Mode 3

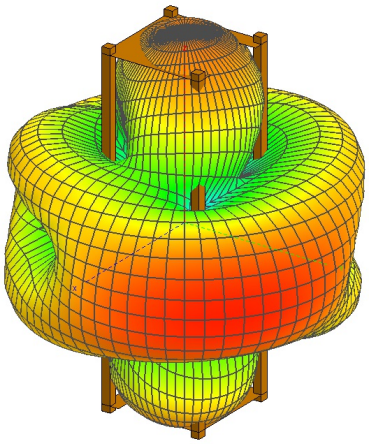

(d) Mode 4

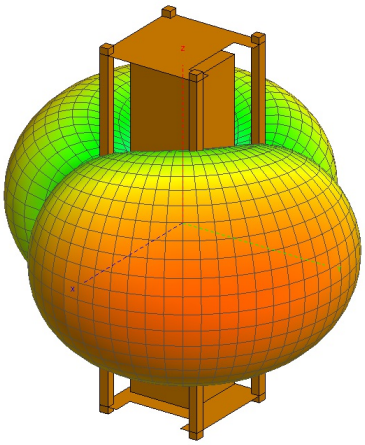

(e) Mode 5

Figure 6.10: Modal far fields for 3U CubeSat with box at 915 MHz

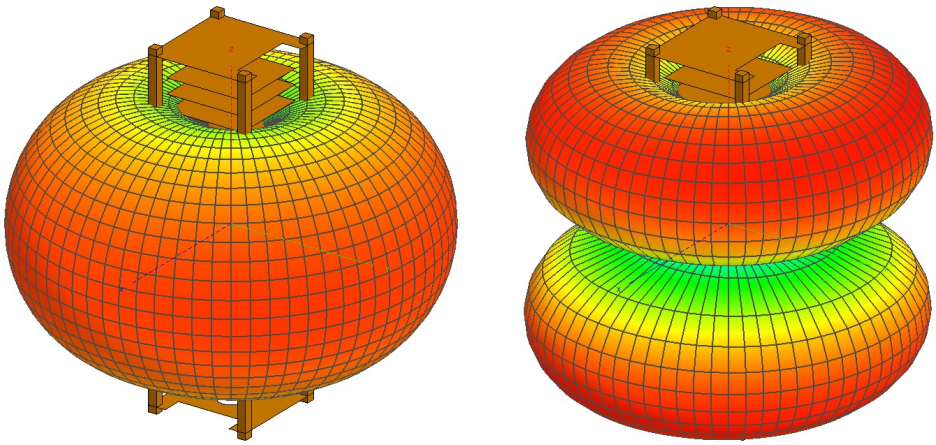

(a) Mode 1

(b) Mode 2

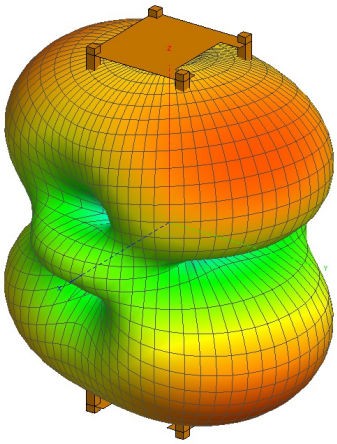

(c) Mode 3

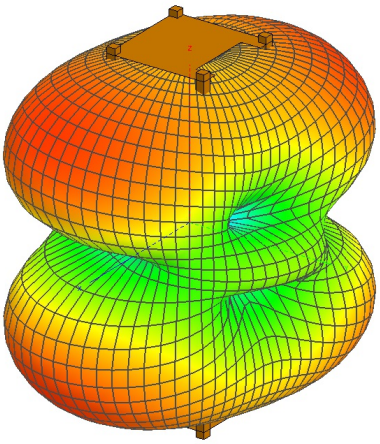

(d) Mode 4

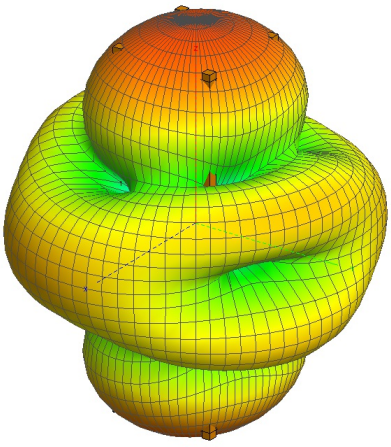

(e) Mode 5

Figure 6.11: Modal far fields for 3U CubeSat with slats at 915 MHz

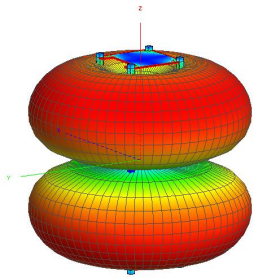

(a) Mode 1

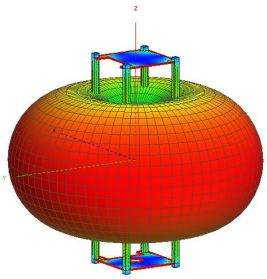

(b) Mode 2

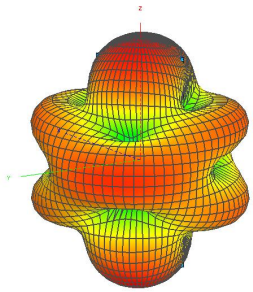

(c) Mode 3

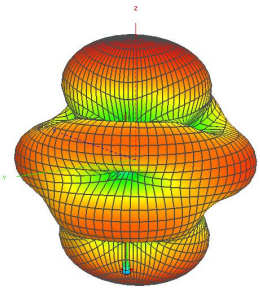

(d) Mode 4

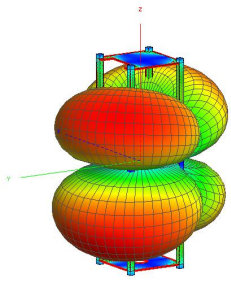

(e) Mode 5

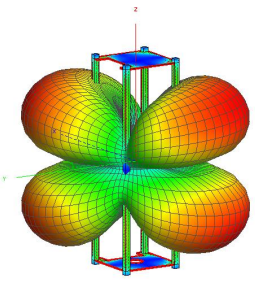

(f) Mode 6

Figure 6.12: Modal far fields for 3U CubeSat at 915 MHz

Table 6.7: Comparing modal far fields between the empty CubeSat and the CubeSat with box at 915 MHz

		CubeSat with Box																
		Mode 1	Mode 2	Mode 3	Mode 4	Mode 5	Mode 6	Mode 7	Mode 8	Mode 9	Mode 10	Mode 11	Mode 12	Mode 13	Mode 14	Mode15	Mode16	Mode 17
Empty CubeSat	Mode 1	391.54	0.90	637.01	639.23	645.89	645.49	254.17	254.42	311.17	421.33	362.96	712.03	418.03	429.64	49.826	394.36	374.73
	Mode 2	5.00	478.65	469.22	475.78	175.49	175.78	589.08	597.68	639.10	928.80	778.25	58.691	628.32	667.70	313.98	583.51	592.46
	Mode 3	775.91	713.22	92.68	224.35	918.74	884.33	292.08	257.98	338.28	208.72	303.60	857.47	157.56	249.88	572.55	311.07	158.14
	Mode 4	778.87	715.81	227.97	87.76	880.16	911.06	260.33	293.42	304.99	304.09	243.88	852.36	250.16	182.01	592.33	187.72	283.23
	Mode 5	381.24	378.39	579.54	608.47	409.18	182.79	350.90	649.25	633.89	910.70	722.87	404.10	547.95	888.65	285.45	368.98	558.38
	Mode 6	365.12	362.85	591.30	575.63	180.62	394.28	629.88	350.48	642.76	832.25	759.78	391.57	834.83	589.29	255.89	521.03	396.41
	Mode 7	221.25	703.73	556.55	469.18	0.8297	242.72	781.05	645.55	809.74	1133.74	962.36	114.69	930.93	759.64	491.66	679.47	572.08
	Mode 8	211.83	688.69	455.83	557.36	235.44	0.61	630.65	771.44	805.90	1117.50	943.38	109.91	694.36	960.50	494.60	521.19	702.86
	Mode 9	615.92	346.22	521.28	521.84	758.89	760.49	276.79	277.66	59.82	236.64	116.71	837.52	409.95	393.02	462.11	445.66	442.87
	Mode 10	490.09	239.38	310.83	272.46	697.93	576.90	4.36	258.86	166.70	250.15	152.69	677.70	89.49	321.61	210.21	132.77	229.57
	Mode 11	491.96	240.17	269.41	308.49	583.84	698.99	256.25	4.60	188.38	159.30	201.69	680.65	312.20	101.61	199.53	246.61	119.54
	Mode 12	96.84	319.18	402.76	406.64	230.90	230.70	380.58	387.77	408.52	648.57	517.47	201.13	472.33	505.35	233.21	441.57	454.58
	Mode 13	193.32	191.17	611.44	622.52	329.51	329.94	460.05	457.92	649.86	830.77	744.55	344.35	602.89	637.10	72.24	459.67	457.34
	Mode 14	319.72	824.59	563.82	571.50	180.39	180.37	813.70	821.36	911.58	1263.50	1070.18	158.15	931.90	983.94	603.02	652.01	690.64
	Mode 15	89.98	334.23	413.56	410.25	280.23	279.39	389.32	401.59	386.42	628.34	494.56	222.46	461.28	495.31	261.11	475.46	486.12
	Mode 16	445.33	434.03	533.43	618.11	442.33	273.83	351.38	562.74	418.53	687.55	532.68	481.53	510.45	837.15	412.10	474.04	515.73
	Mode 17	468.25	444.97	640.72	556.60	291.50	469.58	577.66	361.92	418.10	702.09	529.23	509.82	835.44	557.83	428.32	506.60	517.91

Table 6.8: Comparing modal far fields between the empty CubeSat and the CubeSat with slats at 915 MHz

		CubeSat with Slats																
		Mode 1	Mode 2	Mode 3	Mode 4	Mode 5	Mode 6	Mode 7	Mode 8	Mode 9	Mode 10	Mode 11	Mode 12	Mode 13	Mode 14	Mode15	Mode16	Mode 17
Empty CubeSat	Mode 1	431.34	0.98	272.38	265.78	828.99	828.59	703.76	703.62	443.90	417.27	251.06	627.59	284.70	187.81	65.84	725.61	698.54
	Mode 2	0.41	424.40	692.09	683.79	867.59	877.71	245.39	240.82	791.18	840.94	528.64	31.64	243.04	276.41	277.72	219.65	229.54
	Mode 3	784.56	678.62	247.15	282.94	63.63	151.86	918.72	910.87	198.07	262.58	505.08	802.39	574.27	589.69	706.47	787.76	795.68
	Mode 4	787.23	679.04	281.23	251.83	148.95	63.720	895.53	918.63	227.09	231.89	509.49	807.14	629.63	562.81	715.33	783.89	782.55
	Mode 5	366.80	337.88	655.72	505.93	828.44	818.99	355.28	256.44	519.65	842.43	619.11	374.18	74.37	449.33	256.71	303.89	325.13
	Mode 6	350.92	329.03	508.57	632.40	816.36	821.93	247.25	343.89	817.96	517.45	508.30	380.88	411.68	134.61	219.76	306.69	303.34
	Mode 7	187.30	640.35	793.74	865.80	856.03	841.67	87.83	205.90	967.87	842.37	674.31	125.47	429.84	278.18	446.54	96.49	173.82
	Mode 8	178.88	622.47	860.24	773.35	828.00	852.83	205.46	86.24	791.89	1010.15	751.28	111.33	161.08	492.94	430.85	89.86	174.74
	Mode 9	643.23	338.38	239.76	239.02	573.65	573.83	779.15	784.51	408.00	434.84	50.85	765.87	429.23	266.81	490.88	759.58	740.67
	Mode 10	510.99	219.27	210.67	63.05	363.22	333.46	704.91	631.10	57.61	338.69	279.87	603.96	182.38	361.84	277.42	618.32	621.23
	Mode 11	513.35	223.74	64.52	205.10	329.82	359.00	631.09	710.15	328.19	63.52	209.50	623.10	435.54	136.86	264.09	629.68	615.50
	Mode 12	103.27	280.70	485.86	473.54	705.73	710.67	308.70	302.22	562.56	600.14	322.17	161.44	178.73	170.31	215.37	261.61	359.83
	Mode 13	201.65	158.80	542.02	536.80	933.84	938.94	381.66	383.88	670.01	647.67	558.62	300.04	218.57	235.02	78.36	400.35	388.24
	Mode 14	272.82	753.15	913.40	907.92	875.46	878.87	145.43	153.97	981.45	1036.37	823.08	176.76	382.66	492.33	544.85	192.62	16.666
	Mode 15	101.98	297.58	492.13	476.63	724.40	726.29	367.19	358.85	571.10	620.13	301.15	175.19	210.94	193.23	232.33	317.44	409.48
	Mode 16	434.86	398.24	553.48	445.74	735.91	777.08	408.50	317.31	491.77	797.36	377.96	446.62	123.25	396.01	366.41	349.66	382.35
	Mode 17	459.23	411.37	460.14	558.60	800.22	752.46	333.05	433.78	786.73	523.04	319.08	492.88	456.63	142.67	386.18	384.19	396.47

Table 6.9: Comparing modal far fields between the CubeSat with slats and the CubeSat with box at 915 MHz

		CubeSat with Slats																
		Mode 1	Mode 2	Mode 3	Mode 4	Mode 5	Mode 6	Mode 7	Mode 8	Mode 9	Mode 10	Mode 11	Mode 12	Mode 13	Mode 14	Mode15	Mode16	Mode 17
CubeSat with Box	Mode 1	3.15	371.27	647.11	639.01	870.70	880.78	294.58	289.62	758.43	803.88	477.22	59.60	240.65	255.29	247.75	270.42	279.65
	Mode 2	462.54	2.96	272.99	266.11	844.86	844.06	741.87	741.36	448.37	421.13	246.65	666.54	304.01	199.97	78.52	764.13	737.43
	Mode 3	464.77	608.54	324.22	340.10	93.95	165.54	534.10	492.82	276.01	346.23	506.45	426.11	350.76	449.62	548.11	398.16	420.69
	Mode 4	470.76	610.31	338.72	322.89	161.58	97.47	493.53	546.73	292.96	315.94	486.09	435.65	438.21	398.58	558.32	406.44	423.52
	Mode 5	183.24	620.75	782.46	843.41	849.05	834.64	93.86	192.92	947.65	835.11	659.74	124.45	414.60	270.94	430.95	96.81	166.27
	Mode 6	183.65	616.42	851.34	770.66	825.99	850.34	197.10	94.07	788.87	1003.75	747.35	116.57	158.28	490.44	426.83	92.52	170.99
	Mode 7	574.29	239.54	185.80	61.32	339.48	315.05	750.83	690.32	47.20	314.82	286.33	668.75	211.54	389.33	312.32	667.07	667.58
	Mode 8	583.17	244.46	63.00	182.93	315.61	338.23	692.17	761.02	308.09	49.68	214.25	694.60	473.51	161.75	301.09	682.15	666.61
	Mode 9	622.39	294.58	133.53	121.27	412.38	396.73	824.83	834.42	247.60	279.65	54.32	752.59	412.20	278.86	440.07	786.67	764.15
	Mode 10	906.42	409.31	96.67	140.30	336.44	378.26	1145.65	1152.28	220.86	173.34	221.88	1060.60	617.42	445.75	575.59	1079.53	1062.41
	Mode 11	758.45	348.05	118.27	94.99	373.46	346.29	970.87	973.88	189.49	237.81	132.77	896.84	487.71	364.58	508.41	916.27	895.67
	Mode 12	65.13	681.85	870.38	862.11	841.44	850.37	158.40	155.48	914.75	982.20	738.73	6.26	314.15	414.15	467.77	109.22	135.42
	Mode 13	612.28	399.13	266.92	109.60	257.11	302.36	931.03	750.55	55.17	384.95	401.20	695.30	284.18	545.68	457.73	753.62	758.92
	Mode 14	649.79	417.19	110.30	264.79	312.80	278.94	801.26	984.09	358.90	79.90	327.97	761.84	654.77	264.58	484.79	816.65	798.09
	Mode 15	302.76	44.24	269.13	269.40	675.13	682.57	531.64	539.11	390.04	362.07	346.36	443.12	217.42	170.60	41.52	537.97	514.08
	Mode 16	575.69	374.24	241.52	163.83	248.67	198.69	620.56	561.20	154.51	251.91	479.43	600.68	280.48	407.90	375.88	523.77	513.11
	Mode 17	582.03	359.74	143.00	213.23	192.63	239.25	596.69	666.69	217.78	139.95	384.76	621.92	414.43	286.18	358.66	568.63	539.96

larger eigenvalues it is important to have as much model fidelity as possible to ensure the platform behavior is appropriately captured. If the modeled structure does not correspond closely enough to the actual platform, the results from the synthesis method will not work as desired. At 915 MHz, if the desired pattern relied heavily on modes 7-13, it is unlikely that those modes would appear on the implemented structure.

6.1 Comparing Optimized Patterns from the CubeSat with Slats to the Original CubeSat

The developed synthesis method relies on characteristic mode theory to find the pattern that is closest to the goal pattern that is achievable given the current structure. The CubeSat with slats, while still an approximation of the implemented CubeSat, is a better model for the implemented CubeSat. With the modal far fields changing, it is reasonable to assume that the optimized far field patterns and corresponding surface currents will also change. This section utilizes first part of the synthesis method from the previous chapter and compares the optimized far fields and the goal modal far field patterns to those from the empty CubeSat.

At 400 MHz the first three modal far fields for the CubeSat with slats are shown in Figure 6.5. Inputting the modal far fields and the same goal pattern from the previous chapter, the resulting pattern is shown in Figure 6.13. Comparing this to Figure 5.5, the two have substantially different patterns. The CubeSat with slats has a plane where it is mostly omnidirectional and one null through the center compared to the empty CubeSat pattern with a null in the $y-z$ plane. If the two patterns are compared using the same metric used for comparing the modal patterns, ψ is 608.32. The large magnitude of ψ demonstrates just how large the difference is between the pattern for the empty CubeSat and the pattern for the CubeSat with slats. Figure 6.14 shows the surface current associated with the CubeSat with slats. Comparing that to Figure 5.6, the main high current sections have moved onto the posts and away from the top and bottom plates. For the CubeSat with slats the highest current is now predominantly on the posts and the lowest current is on the slats closest to the top and bottom plates on the CubeSat. Adding the slats significantly changed the optimized pattern as well as the current.

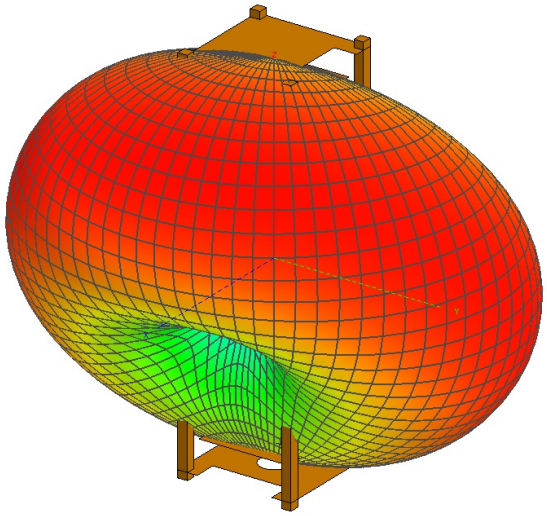

Figure 6.13: Optimized pattern at 400 MHz for CubeSat with slats

Even in the case where there are only three significant modes, there is a large change in the pattern and surface current that should be achieved for optimal performance.

The optimized radiation pattern and surface current can also be compared at 435 MHz. The goal at 435 MHz is to get as much energy radiating towards Earth as possible. Using the modal far fields from Figure 6.8, Figure 6.15 shows the optimized far field pattern for the CubeSat with slats. Comparing that to Figure 5.8, the CubeSat with slats does not have the omnidirectional pattern that the empty CubeSat's optimized pattern has. It has a slight indentation around 45 degrees. Comparing the patterns, the ψ value is 189.14. This means that patterns are closer than the two optimized patterns at 400 MHz but they are still substantially different. The optimized current at 435 MHz is shown in Figure 6.16. The minimum and maximum current regions have changed substantially. Maximum current is now found on the posts compared to on the plates previously. The lowest current points are on the slats closest to the top and bottom plates. The optimized surface current for the CubeSat with slats at 435 MHz is similar to the optimized surface current on the same structure at 400 MHz. The patterns are very different but the maximum and minimum placement are similar.

At 915 MHz, the CubeSat with slats has an omnidirectional pattern as its first mode unlike before where it was the second mode. Examining the surface current shown in Figure 6.17, the currents have maximums at the

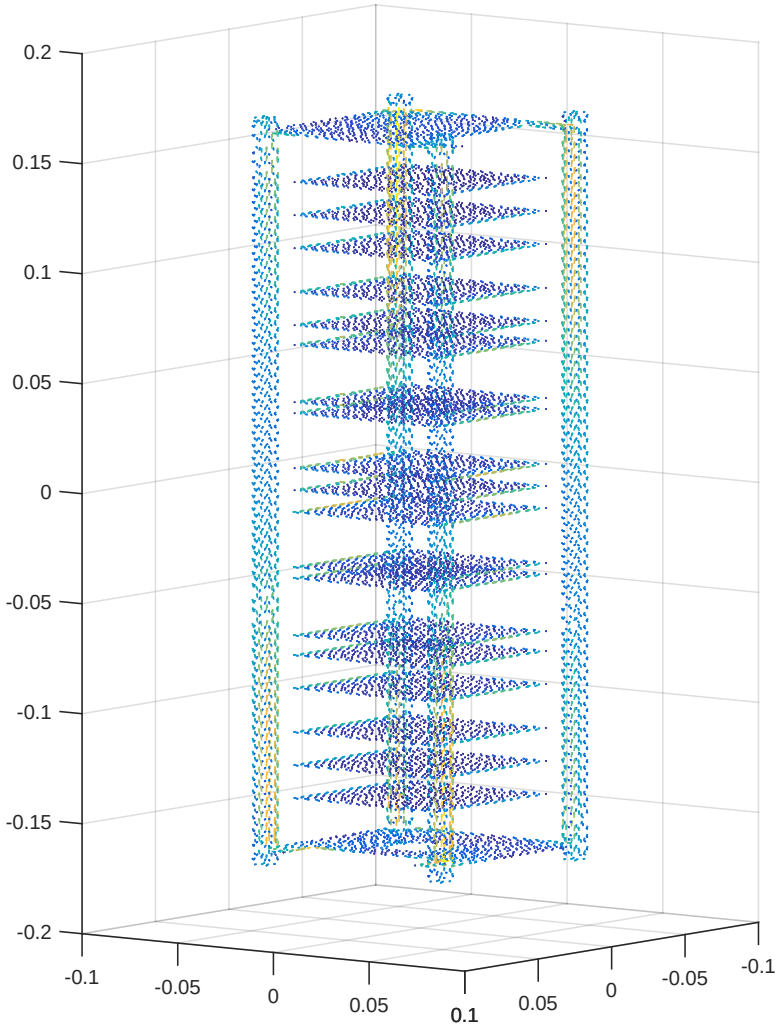

Figure 6.14: Surface current at 400 MHz for CubeSat with slats

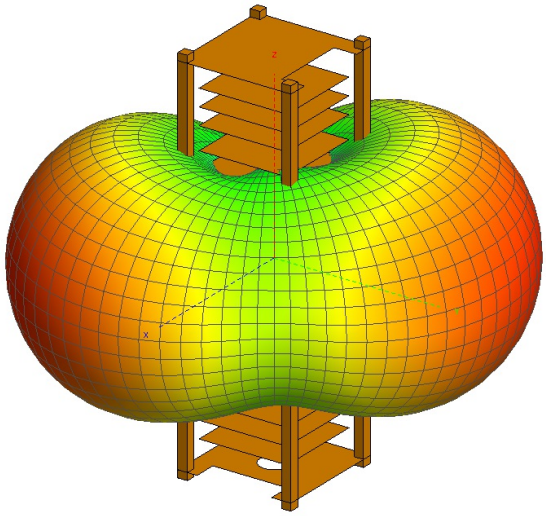

Figure 6.15: Optimized pattern at 435 MHz for CubeSat with slats

center of the posts and all four posts are in phase. This is not surprising as mode 1 of the CubeSat with slats corresponds to mode 2 of the original platform. If the mode was no longer present, the designer would have to use one of the other synthesis methods to find the pattern closest to the original that is achievable. The previous section of this chapter shows that the far fields for mode 1 of the CubeSat with slats is the same as the pattern from the previous chapter.

Overall, the analysis at the first two frequencies relied on all of the significant modes to generate the optimal pattern. Because the modal far fields changed significantly between the first structure and the second, the optimal patterns and surface currents shifted significantly when using the CubeSat with slats compared to the empty CubeSat. The synthesis method relies on an accurate representation of the platform to generate the optimal patterns and surface currents to be used. If the platform must be simplified to be modeled, it is important to make sure that only the most significant modes that should not change between the simulated and manufactured structures are used. Any mode that is narrow band or has a large amount of nulls, may not be present in the final implementation. Because the mode chosen for implementation at 915 MHz was still present, the goal surface current was extremely similar. This means the implementation used for the original empty CubeSat should translate to the CubeSat with slats unlike the element designs at 400 MHz and 435 MHz. Based on the large difference

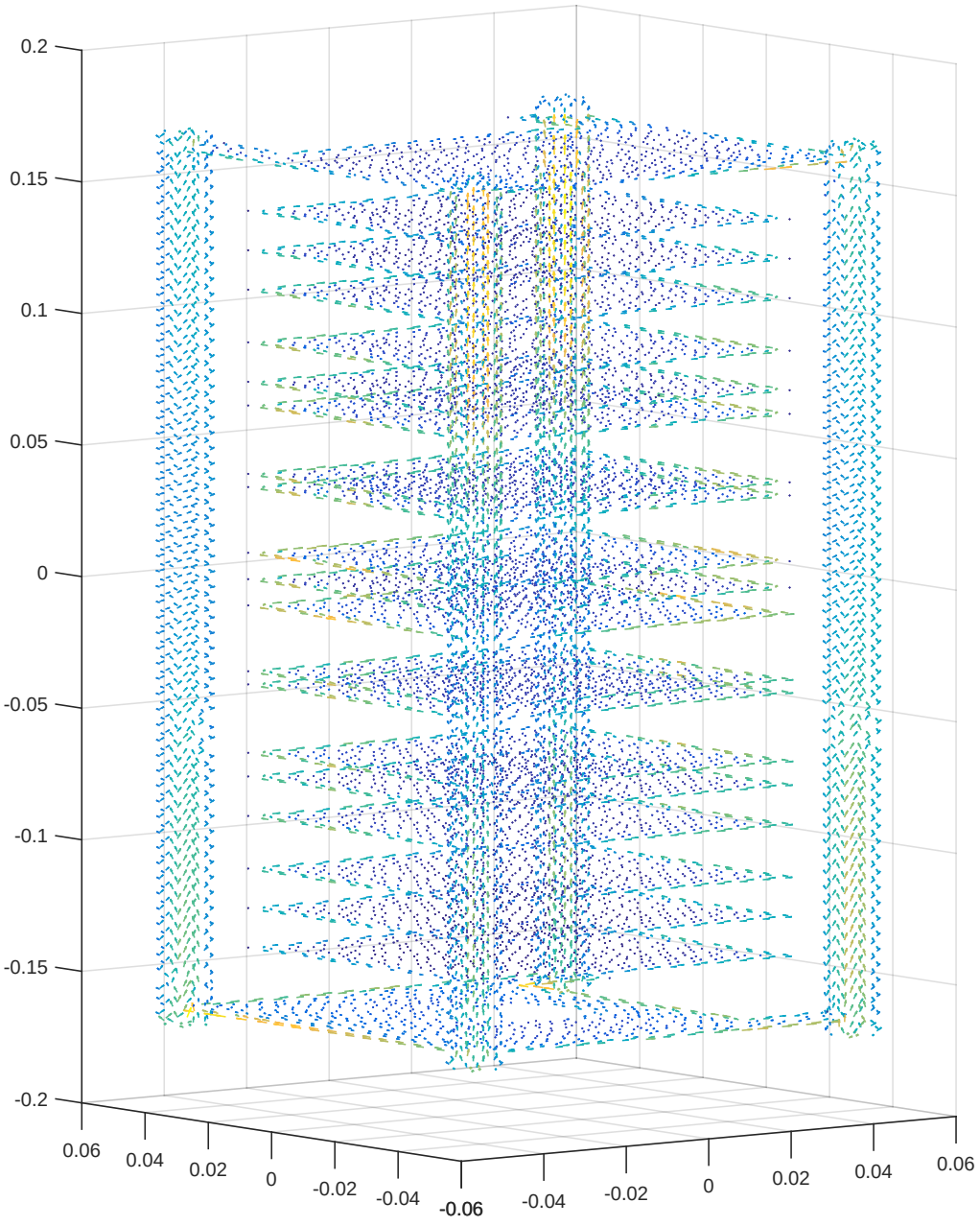

Figure 6.16: Surface current at 435 MHz for CubeSat with slats

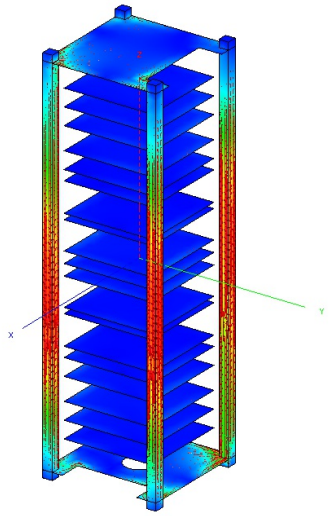

Figure 6.17: Surface current corresponding to omnidirectional pattern at 915 MHz for CubeSat with slats

in the optimal patterns and surface currents, the element implementations and feed points should be changed to take advantage of the modes on the new structure. The biggest conclusion is that when using this synthesis technique it is important to model the structure as closely as possible to the true implementation. For full confidence and the ability to use higher order modes, one would need to know everything about the structure. Because that is not feasible, the designer should not use some of the higer order modes based on the known assumptions in the model. If there are changes to the platform that alter the modal far fields, the analysis will no longer provide optimal solutions and may result in antenna designs that are at a significant disadvantage.

CHAPTER 7

CONCLUSIONS AND FUTURE WORK

As technology progresses, it is becoming more and more critical to install multiple antenna systems in close proximity. Much of the research pertaining to antennas in close proximity is limited in scope. Co-site interference research mitigates interference by cycling through types of antennas or using active cancellation, mutual coupling research is typically limited to similar elements or a single frequency, and MIMO research is single frequency and focused solely on channel capacity. While prior research does touch on issues with antennas in proximity, it does not provide information about how to design multiple elements that are to be placed on an existing structure. In addition, the prior research about antennas in proximity does not adequately address the radiation pattern as much of the results are concerned with raising isolation. It is the goal of this research to eventually provide an antenna synthesis procedure that will allow for the design and installation of multiple antennas over multiple frequency bands onto a pre-existing structure with antenna patterns close to goal patterns.

To reach that goal, this work has explored how antennas are typically designed when they are attached to preexisting structures. Research shows characteristic mode theory is commonly used to find feed points for resonant modes. This work develops a method for finding a feed location to excite modes that are not necessarily resonant at the frequency of interest using the impedance matrix. With the impedance matrix for a structure, a region is determined for the feed. The feed can be placed anywhere within that region to excite the mode. This research has shown that just choosing the feed location, however, is not enough. It is also important to look at the modal surface current needed to achieve the desired far field pattern. In the example from Chapter 3, the desired mode had a circulating surface current so a spiral element was chosen to ensure that the proper mode was excited. The feed point in conjunction with the spiral element that coupled to the

surface excited the needed surface current and ensured that the resulting simulated and built antenna had a radiation pattern that was close to that of the third mode. While the antenna's radiation pattern was not purely that of the desired mode, it did display the desired characteristics with a null in the z-axis and an omnidirectional pattern in the $x-y$ plane.

Next, a pattern synthesis procedure was developed based on the characteristic modes of an existing structure and a goal radiation pattern specifying both power and polarization. The method was able to identify the modal weighting coefficients that lead to a minimum mean-square error between the possible radiation patterns from the existing structure and the goal pattern. Using a dipole, a square plate, and a patch antenna over an infinite ground plane, the method was shown to have given accurate modal weighting coefficients even with complex characteristic far fields.

Because the goal is not always to create a radiation pattern with a specified polarization, a second method was developed to find the optimal modal weighting coefficients for a goal power pattern. Again using a dipole and a patch antenna over an infinite ground plane, the method was able to find modal weighting coefficients that closely approximated the goal pattern with minimal error. The method was also able to show that a two-element turnstile array is able to produce a pattern close to unity gain if it is excited properly. A 3-loop, 3-dipole antenna was also evaluated and the modal weighting coefficients are found that lead to a pattern with less than 0.05 dB of ripple across the radiation sphere.

Knowing the modal weighting coefficients that lead to the goal pattern allows one to visualize the needed surface current to achieve the desired far-field pattern. Once the modal surface current needed is known, it is possible to understand the type of element that would need to be designed in order to excite the appropriate modal surface current on the existing structure and thus create a radiation pattern closely approximating the goal radiation pattern.

Using the developed pattern synthesis methodology and the modal surface currents, a synthesis method was developed to design antenna elements and best understand where the antennas should be placed. The synthesis method uses an iterative process to design the antenna elements starting at the lowest frequency and working towards the higher frequency. After each band, the previous bands are checked to ensure that their match and patterns have not

changed substantially. For each antenna element, the needed surface current as well as the surface current placement for the higher frequencies are taken into account to ensure that the design for one frequency does not largely affect the other frequency bands.

A CubeSat was used as a sample platform to demonstrate the synthesis method. An element was designed for 400 MHz to communicate with Earth. For that reason the power and polarization pattern optimization was used to get as much power radiating toward Earth as possible. The surface current corresponding to the closest achievable pattern to the goal is found and implemented in simulation. Another optimization is run at 435 MHz using the power pattern optimization with the goal to also get as much power as possible radiating toward Earth. The surface current from the optimization is used to design an antenna element for 435 MHz that does not interfere with the element and pattern at 400 MHz. Lastly, the modal far fields are viewed at 915 MHz with the goal of having an omnidirectional pattern in the $x-y$ plane. The second mode at 915 MHz has a corresponding omnidirectional pattern. The surface current shows that high current must be in phase at the center of each post on the CubeSat. To implement the surface current without disrupting the currents for the previous frequencies, four IFAs are used.

Once the antenna was designed in simulation, the next step was to build the antenna, measure the far field patterns, and compare them to the simulated patterns. The antenna was built out of brass and measured in a far field tapered chamber. The cut planes from the implemented radiation patterns largely match the simulated patterns. There are some places where the simulated and measured patterns diverge but these are largely due to the direction the cable had to be run to get it away from the platform in the chamber. The overall patterns match well with simulation, validating the synthesis method in this case. The antenna elements are connected to the platform and utilize the platform to get better results than using elements alone.

The developed synthesis procedure for multiple antenna elements designed on an existing platform allows for more efficient antenna design when installing elements on existing structures. The process provides the designer with an understanding of the achievable patterns on the existing structure as well as physical insight into viable feed locations. With this insight, there

is no need to develop a variety of different elements and test for their interactions for multiple placements. The elimination of trial-and-error process results in significant time savings for the antenna designer. The method also quantifies how close to a goal radiation pattern an installed antenna's radiation pattern can be based on the existing structure. This ensures antenna designers do not waste time trying to achieve a pattern that is not possible because of the existing platform.

In addition to the synthesis procedure making the design process more efficient, the developed antennas will have improved individual performance because they are taking advantage of the existing structure. By not isolating the elements from the existing structure, the additional metal can be used to create additional gain in the direction of interest. Because the designed antennas utilize the existing structure, this also can result in increased efficiency and bandwidth performance compared to similar elements.

Overall the developed synthesis procedure leads to improved, more effective antenna designs that fully utilize the existing structure to improve antenna performance. By taking radiation pattern into account, the design process ensures that gain improvements are in the needed directions and that system requirements are satisfied.

The synthesis procedure is only as strong as the model that is used for the platform. Two slight modifications to the CubeSat antenna were explored and the modal far fields for relevant modes were compared. Many of the modes outside of the first few changed significantly as the structure changed. The more the structure changed, the more likely the modes were to differ from the original. The same optimization process used on the original CubeSat model was used on the CubeSat with slats model. The output radiation patterns and surface currents for 400 MHz and 435 MHz differed substantially from the original optimal radiation pattern. The addition of the slats greatly altered how the CubeSat radiated and the best pattern that was achievable given the platform. The changes were largely due to the optimization algorithms using higher modes that were very different between the original CubeSat and the CubeSat with slats. For this reason, if this synthesis method is used and higher order modes are needed to implement the goal pattern, a high fidelity model must be utilized. If a high fidelity model is not used and higher order modes are required, there is no guarantee the modes actually exist on the structure, which could lead to an antenna

designer trying to implement a pattern that is not realizable on the implemented platform.

In the future, the synthesis method can be extended to include optimization based on other factors like isolation or match. The current synthesis method assumes that all the bands are being implemented based on a radiation pattern, which is not always the case for antenna design. Additional research can also be done to add dielectrics or lossy materials to the analysis. The current method used here relies on a commercial characteristic mode solver that requires the use of only perfect electric conductor (PEC). By extending the method to other materials, there are more platforms that can utilize the developed synthesis method. In the future, more work can be done to examine the impact of PEC versus copper or brass on antenna implementations when utilizing characteristic mode theory. It is possible that the use of real metal versus PEC will cause the modes to shift in a predictable manner.

As CubeSat technology progresses, many CubeSat programs are beginning to use the L and S bands to communicate with the CubeSats. These bands have higher frequencies than those discussed in this dissertation but many of the same techniques should still be applicable. The future work is to formalize how to use this synthesis method when the structure is too large or has too many relevant modes for this exact analysis to be used. Many of the techniques in this dissertation should still be applicable and additional work will be done in the future to formalize changes to the synthesis method in this scenario.

Other future work is to evaluate the antenna for isolation and for its performance when the other ports are not terminated for 50 Ω. The method can be updated to account for what impedance is required at the other frequencies to ensure that the antenna system functions as a whole. The last interesting piece for future work is to tie the neighborhood portion of this work to the characteristic mode simulations to see if there is a faster way to estimate far field performance based on a conformal feed geometry.

REFERENCES

[1] N. L. Bohannon and J. T. Bernhard, "Design guidelines using characteristic mode theory for improving the bandwidth of PIFAs," *IEEE Trans. on Antennas and Propagation*, vol. 63, no. 2, p. 459, 2015.

[2] A. Andujar, J. Anguera, and C. Puente, "Ground plane boosters as a compact antenna technology for wireless handheld devices," *IEEE Trans. on Antennas and Propagation*, vol. 59, no. 5, pp. 1668–1677, 2011.

[3] S. T. Li, J. Logan, and J. Rockway, "Automated procedure for shipboard exterior communication rf system design," *IEEE Trans. on Electromagnetic Compatibility*, no. 4, pp. 219–223, 1980.

[4] G. Travis and H. Lenzing, "Shipboard HF interference: Problems and mitigation," in *1989 IEEE Military Communications Conference*. IEEE, 1989, pp. 106–110.

[5] K. Allsebrook and C. Ribble, "VHF cosite interference challenges and solutions for the United States Marine Corps' expeditionary fighting vehicle program," in *2004 IEEE Military Communications Conference*, vol. 1, Oct 2004, pp. 548–554 Vol. 1.

[6] S. Karlsson, M. Grenvall, A. Kvick, L. Eugensson, F. Grahn, and L. Pettersson, "Co-site interference analysis and antenna system integration on a Swedish combat vehicle platform," in *2013 IEEE Military Communications Conference*, Nov 2013, pp. 369–374.

[7] M. Alemohammad, D. Novak, and R. Waterhouse, "Photonic signal cancellation for co-site interference mitigation," in *2011 IEEE Military Communications Conference*. IEEE, 2011, pp. 2142–2146.

[8] J. Low and A. S. Wong, "Systematic approach to cosite analysis and mitigation techniques," in *Proc. of the 1990 IEEE Tactical Communications Conference*. IEEE, 1990, pp. 555–567.

[9] J. Isaacs, W. Robertson, and R. Morrison, "A cosite analysis method for frequency hopping radio systems," in *1991 IEEE Military Communications Conference*. IEEE, 1991, pp. 522–526.

[10] N. Chan and L. Peterson, "Reduction of cosite interference for digital fm frequency hopping radios," in *1996 IEEE Military Communications Conference*, vol. 3. IEEE, 1996, pp. 1036–1040.

[11] D. He, C. Ozbay, Y. Chi, K. Ambrose, and G. Michel, "Integrated radio frequency design environment," in *2006 IEEE Military Communications Conference*. IEEE, 2006, pp. 1–7.

[12] E. Yalcin, C. Girard, M. Cabellic, M. Hélier, G. Alquié, and J.-L. Montmagnon, "Modelling interference phenomena between cosite radiocommunication equipments to evaluate systems performance degradation," in *Proc. of IEEE Symposium on Electromagnetic Compatibility*. IEEE, 2008, pp. 1–6.

[13] F. German, K. Annamalai, M. Young, and M. C. Miller, "Simulation and data management for cosite interference prediction," in *2010 IEEE International Symposium on Electromagnetic Compatibility*. IEEE, 2010, pp. 869–874.

[14] S. Georgakopoulos, C. Balanis, and C. Birtcher, "Cosite interference between wire antennas on helicopter structures and rotor modulation effects: FDTD versus measurements," *IEEE Trans. on Electromagnetic Compatibility*, vol. 41, no. 3, pp. 221–233, Aug 1999.

[15] M. Radway and D. Filipovic, "Adaptive pattern nulling method for multi-armed spiral antennas," in *2010 Proc. of IEEE Antennas and Propagation Society*. IEEE, 2010, pp. 1–4.

[16] T. Roach, "Antenna element pattern reconfigurability in adaptive arrays," Ph.D. dissertation, University of Illinois at Urbana-Champaign, May 2010.

[17] S. Yong, "Design and analysis of pattern null reconfigurable antennas," Ph.D. dissertation, University of Illinois at Urbana-Champaign, May 2012.

[18] C. Cutler, A. King, and W. Kock, "Microwave antenna measurements," *Proceedings of the IRE*, vol. 35, no. 12, pp. 1462–1471, Dec 1947.

[19] A. Yaghjian, "Efficient computation of antenna coupling and fields within the near-field region," *IEEE Trans. on Antennas and Propagation*, vol. 30, no. 1, pp. 113–128, Jan 1982.

[20] D. M. Pozar, "Input impedance and mutual coupling of rectangular microstrip antennas," *IEEE Trans. on Antennas and Propagation*, vol. 30, no. 6, pp. 1191–1196, Nov 1982.

[21] F. Yang and Y. Rahmat-Samii, "Microstrip antennas integrated with electromagnetic band-gap (EBG) structures: A low mutual coupling design for array applications," *IEEE Trans. on Antennas and Propagation*, vol. 51, no. 10, pp. 2936–2946, Oct 2003.

[22] A. Diallo, C. Luxey, P. Le-Thuc, R. Staraj, and G. Kossiavas, "Study and reduction of the mutual coupling between two mobile phone PIFAs operating in the DCS1800 and UMTS bands," *IEEE Trans. on Antennas and Propagation*, vol. 54, no. 11, pp. 3063–3074, Nov 2006.

[23] C.-Y. Chiu, C.-H. Cheng, R. Murch, and C. Rowell, "Reduction of mutual coupling between closely-packed antenna elements," *IEEE Trans. on Antennas and Propagation*, vol. 55, no. 6, pp. 1732–1738, June 2007.

[24] Y. Gao, X. Chen, Z. Ying, and C. Parini, "Design and performance investigation of a dual-element PIFA array at 2.5 GHz for MIMO terminal," *IEEE Trans. on Antennas and Propagation*, vol. 55, no. 12, pp. 3433–3441, 2007.

[25] Y. Chung, S.-S. Jeon, D. Ahn, J.-I. Choi, and T. Itoh, "High isolation dual-polarized patch antenna using integrated defected ground structure," *IEEE Microwave and Wireless Components Letters*, vol. 14, no. 1, pp. 4–6, 2004.

[26] H. Li, J. Xiong, and S. He, "A compact planar MIMO antenna system of four elements with similar radiation characteristics and isolation structure," *IEEE Antennas and Wireless Propagation Letters*, vol. 8, pp. 1107–1110, 2009.

[27] F. Zhu, J. Xu, and Q. Xu, "Reduction of mutual coupling between closely-packed antenna elements using defected ground structure," in *Proc. of 2009 IEEE International Symposium of Microwave, Antenna, Propagation and EMC Technologies for Wireless Communications.* IEEE, 2009, pp. 1–4.

[28] M. A. Jensen and J. W. Wallace, "A review of antennas and propagation for MIMO wireless communications," *IEEE Trans. on Antennas and Propagation*, vol. 52, no. 11, pp. 2810–2824, 2004.

[29] S. Lu, H. Hui, and M. Bialkowski, "Optimizing MIMO channel capacities under the influence of antenna mutual coupling," *IEEE Antennas and Wireless Propagation Letters*, vol. 7, pp. 287–290, 2008.

[30] M. P. Karaboikis, V. C. Papamichael, G. F. Tsachtsiris, C. F. Soras, and V. T. Makios, "Integrating compact printed antennas onto small diversity/MIMO terminals," *IEEE Trans. on Antennas and Propagation*, vol. 56, no. 7, pp. 2067–2078, 2008.

[31] M. Pelosi, M. B. Knudsen, and G. F. Pedersen, "Multiple antenna systems with inherently decoupled radiators," *IEEE Trans. on Antennas and Propagation*, vol. 60, no. 2, pp. 503–515, 2012.

[32] Z. Li, Z. Du, M. Takahashi, K. Saito, and K. Ito, "Reducing mutual coupling of MIMO antennas with parasitic elements for mobile terminals," *IEEE Trans. on Antennas and Propagation*, vol. 60, no. 2, pp. 473–481, 2012.

[33] S. Zhang, S. N. Khan, and S. He, "Reducing mutual coupling for an extremely closely-packed tunable dual-element PIFA array through a resonant slot antenna formed in-between," *IEEE Trans. on Antennas and Propagation*, vol. 58, no. 8, pp. 2771–2776, 2010.

[34] J. D. Boerman and J. T. Bernhard, "Performance study of pattern reconfigurable antennas in MIMO communication systems," *IEEE Trans. on Antennas and Propagation*, vol. 56, no. 1, pp. 231–236, 2008.

[35] B. A. Cetiner, E. Akay, E. Sengul, and E. Ayanoglu, "A MIMO system with multifunctional reconfigurable antennas," *IEEE Antennas and Wireless Propagation Letters*, vol. 5, no. 1, pp. 463–466, 2006.

[36] H. Li, Z. Miers, and B. K. Lau, "Design of orthogonal MIMO handset antennas based on characteristic mode manipulation at frequency bands below 1 GHz," *IEEE Trans. on Antennas and Propagation*, vol. 62, no. 5, pp. 2756–2766, May 2014.

[37] H. Li, Y. Tan, B. K. Lau, Z. Ying, and S. He, "Characteristic mode based tradeoff analysis of antenna-chassis interactions for multiple antenna terminals," *IEEE Transactions on Antennas and Propagation*, vol. 60, no. 2, pp. 490–502, Feb 2012.

[38] W.-J. Liao, S.-H. Chang, J.-T. Yeh, and B.-R. Hsiao, "Compact dual-band WLAN diversity antennas on USB dongle platform," *IEEE Trans. on Antennas and Propagation*, vol. 62, no. 1, pp. 109–118, 2014.

[39] D. Yuan, Z. Du, K. Gong, and Z. Feng, "A four-element antenna system for mobile phones," *IEEE Antennas and Wireless Propagation Letters*, vol. 6, pp. 655–658, 2007.

[40] J. X. Yun and R. G. Vaughan, "Space efficiency of multiple element antennas," *IEEE Trans. on Antennas and Propagation*, vol. 60, no. 6, pp. 3066–3071, 2012.

[41] E. Newman, "Small antenna location synthesis using characteristic modes," *IEEE Trans. on Antennas and Propagation*, vol. 27, p. 530, 1979.

[42] K. Murray and B. Austin, "HF antennas on vehicles-a characteristic modal approach," in *IEE Colloquium on HF Antennas Systems*. IET, 1992, pp. 2–1.

[43] B. Austin and K. Murray, "Modelling and design of vehicle NVIS antenna systems using characteristic modes," in *1994 International Conference on HF Radio Systems and Techniques*, Jul 1994, pp. 207–211.

[44] K. Murray and B. Austin, "Synthesis of vehicular antenna NVIS radiation patterns using the method of characteristic modes," *IEE Proceedings-Microwaves, Antennas and Propagation*, vol. 141, no. 3, pp. 151–154, 1994.

[45] G. Huff, J. Feng, S. Zhang, G. Cung, and J. Bernhard, "Directional reconfigurable antennas on laptop computers: Simulation, measurement and evaluation of candidate integration positions," *IEEE Trans. on Antennas and Propagation*, vol. 52, no. 12, pp. 3220–3227, Dec 2004.

[46] A. Araghi and G. Dadashzadeh, "Oriented design of an antenna for MIMO applications using theory of characteristic modes," *IEEE Antennas and Wireless Propagation Letters*, vol. 11, pp. 1040–1043, 2012.

[47] Y. Chen and C.-F. Wang, "Electrically small UAV antenna design using characteristic modes," *IEEE Trans. on Antennas and Propagation*, vol. 62, no. 2, pp. 535–545, 2014.

[48] R. J. Garbacz and R. Turpin, "A generalized expansion for radiated and scattered fields," *IEEE Trans. on Antennas and Propagation*, vol. 19, no. 3, pp. 348–358, 1971.

[49] R. F. Harrington and J. R. Mautz, "Theory of characteristic modes for conducting bodies," *IEEE Trans. on Antennas and Propagation*, vol. 19, no. 5, pp. 622–628, 1971.

[50] M. Cabedo-Fabres, E. Antonino-Daviu, A. Valero-Nogueira, and M. F. Bataller, "The theory of characteristic modes revisited: A contribution to the design of antennas for modern applications," *IEEE Antennas and Propagation Magazine*, vol. 49, no. 5, pp. 52–68, 2007.

[51] J. Adams, "Characteristic modes for impedance matching and broadbanding of electrically small antennas," Ph.D. dissertation, University of Illinois at Urbana-Champaign, May 2011.

[52] M. Young and J. Bernhard, "Effect of ground plane size and geometry on frequency reconfigurable antenna electrical performance," in *2013 IEEE International Symposium on Antennas and Propagation*. IEEE, 2013, pp. 1–2.

[53] N. Bohannon and J. Bernhard, "Investigation of the impact of copper thickness on the center frequency for electrically small antennas," in *2013 IEEE International Symposium on Antennas and Propagation*. IEEE, 2013, pp. 1–2.

[54] Y. Chen and C.-F. Wang, "HF band shipboard antenna design using characteristic modes," *IEEE Transactions on Antennas and Propagation*, vol. 63, no. 3, pp. 1004–1013, 2015.

[55] C. G. Buxton, "Design of a broadband array using the foursquare radiating element," Ph.D. dissertation, Virginia Tech, May 2001.

[56] D. R. Rhodes, "The optimum line source for the best mean-square approximation to a given radiation pattern," *IEEE Trans. on Antennas and Propagation*, vol. 11, no. 4, pp. 440–446, 1963.

[57] R. Fante, "Optimum distribution over a circular aperture for best mean-square approximation to a given radiation pattern," *IEEE Trans. on Antennas and Propagation*, vol. 18, no. 2, pp. 177–181, 1970.

[58] W. Stutzman, "Synthesis of shaped-beam radiation patterns using the iterative sampling method," *IEEE Trans. on Antennas and Propagation*, vol. 19, no. 1, pp. 36–41, 1971.

[59] G. A. Deschamps and H. Cabayan, "Antenna synthesis and solution of inverse problems by regularization methods," *IEEE Trans. on Antennas and Propagation*, vol. 20, no. 3, pp. 268–274, 1972.

[60] R. F. Harrington and J. R. Mautz, "Control of radar scattering by reactive loading," *IEEE Trans. on Antennas and Propagation*, vol. 20, no. 4, pp. 446–454, 1972.

[61] R. F. Harrington and J. R. Mautz, "Synthesis of loaded n-port scatterers," DTIC Document, Tech. Rep., 1972.

[62] R. F. Harrington and J. Mautz, "Pattern synthesis for loaded n-port scatterers," *IEEE Trans. on Antennas and Propagation*, vol. 22, no. 2, pp. 184–190, 1974.

[63] J. R. Mautz and R. F. Harrington, "Computational methods for antenna pattern synthesis," *IEEE Trans. on Antennas and Propagation*, vol. 23, no. 4, pp. 507–512, 1975.

[64] R. J. Garbacz and D. M. Pozar, "Antenna shape synthesis using characteristic modes," *IEEE Trans. on Antennas and Propagation*, vol. 30, no. 3, pp. 340–350, 1982.

[65] F. Harackiewicz and D. M. Pozar, "Optimum shape synthesis of maximum gain omnidirectional antennas," *IEEE Trans. on Antennas and Propagation*, vol. 34, no. 2, pp. 254–258, Feb 1986.

[66] H.-P. Chang, T. K. Sarkar, and O. M. Pereira-Filho, "Antenna pattern synthesis utilizing spherical Bessel functions," *IEEE Trans. on Antennas and Propagation*, vol. 48, no. 6, pp. 853–859, 2000.

[67] D. M. Pozar, "Antenna synthesis and optimization using weighted Inagaki modes," *IEEE Trans. on Antennas and Propagation*, vol. 32, no. 2, pp. 159–165, 1984.

[68] O. M. Bucci, G. D'Elia, G. Mazzarella, and G. Panariello, "Antenna pattern synthesis: A new general approach," *Proceedings of the IEEE*, vol. 82, no. 3, pp. 358–371, 1994.

[69] W. K. Saunders, *On the Unity Gain Antenna*. Pergamon Press, 1963, vol. 2, pp. 1125–1130.

[70] G. Byun, H. Choo, and H. Ling, "Optimum placement of DF antenna elements for accurate DOA estimation in a harsh platform environment," *IEEE Transactions on Antennas and Propagation*, vol. 61, no. 9, pp. 4783–4791, 2013.

[71] S. Gao, K. Clark, M. Unwin, J. Zackrisson, W. A. Shiroma, J. M. Akagi, K. Maynard, P. Garner, L. Boccia, G. Amendola, and et al., "Antennas for modern small satellites," *IEEE Antennas and Propagation Magazine*, vol. 51, no. 4, pp. 40–56, 2009.

[72] Y. Yao, S. Liao, J. Wang, K. Xue, E. A. Balfour, and Y. Luo, "A new patch antenna designed for CubeSat: Dual feed, l/s dual-band stacked, and circularly polarized." *IEEE Antennas and Propagation Magazine*, vol. 58, no. 3, pp. 16–21, June 2016.

[73] A. K. A. N. Volkan, "Electrically small printed antenna for applications on CubeSat and nano-satellite platforms," *Microwave and Optical Technology Letters*, vol. 57, no. 4, pp. 891–896, 2015. [Online]. Available: http://dx.doi.org/10.1002/mop.28989

[74] R. Munakata et al., "CubeSat design specification rev. 12," *The CubeSat Program, California Polytechnic State University*, vol. 1, 2009.

[75] L. J. Ippolito, "Radio propagation for space communications systems," *Proceedings of the IEEE*, vol. 69, no. 6, pp. 697–727, 1981.